Gamma-ray studies of the young shell-type SNR RX J1713.7–3946

Dissertation

zur Erlangung des akademischen Grades

Dr. rer. nat.
im Fach Physik

eingereicht an der
Mathematisch-Naturwissenschaftlichen Fakultät
der Universität Potsdam

von
M.Sc. Simone Federici
geboren in Rom (Italien)

Erstgutachter und Betreuer:	Prof. Dr. Martin Pohl
Zweitgutachterin:	Dr. Lida Oskinova
Externe Gutachterin:	Prof. Dr. Julia Tjus

2013/2014

Published online at the
Institutional Repository of the University of Potsdam:
URL http://opus.kobv.de/ubp/volltexte/2014/7173/
URN urn:nbn:de:kobv:517-opus-71734
http://nbn-resolving.de/urn:nbn:de:kobv:517-opus-71734

Declaration

The material contained within this thesis has not previously been submitted for a degree at any other university or any other higher education institute. The research reported within this thesis has been conducted by the author unless indicated otherwise.

Acknowledgements

I would like to thank Professor Martin Pohl for allowing me the opportunity to work with the DESY Astroparticle Theory group, a valuable experience I have thoroughly enjoyed, and yet for his advice and patience in his role as my supervisor.

Thanks go also to the russian-speaking part of the group in DESY (including the outsider Maxim) and the other people of the group from the University of Potsdam, with whom I had great time (a special mention goes to Iman and his wife Maryam for their delicious iranian dinner).

Particular thanks to my officemates Igor and Anton for their useful feedback on this manuscript. Furthermore, I am grateful to Robert who has kindly helped me with the translation of the Zusammenfassung.

I also want to thank all the people who are no longer in Berlin (Luz, Michelangelo and Ena, Yurii and Dariya, Sara, ...) for the great time we had together and the laughs that have made many greasy BBQ events a very healthy time.

Being part of this group and meeting people from all over the world has been a very enriching experience which I am grateful for.

And finally, most of all, I thank my family and Valentina, for giving me the confidence to enjoy life and for supporting me all these years.

Contents

List of Figures

List of Tables

to my family and
to all the γ-rays that made this possible

Introduction

One of the most significant current discussions in Astrophysics relates to the origin of high-energy cosmic rays. According to our current knowledge, the abundance distribution of the elements in cosmic rays at their point of origin indicates, within plausible error limits, that they were initially formed by nuclear processes in the interiors of stars. It is also believed that their energy distribution up to 10^{18} eV has Galactic origins. But even though the knowledge about potential sources of cosmic rays is quite poor above $\sim 10^{15}$ eV, that is the "knee" of the cosmic-ray spectrum, up to the knee there seems to be a wide consensus that supernova remnants are the most likely candidates. Evidence of this comes from observations of non-thermal X-ray radiation, requiring synchrotron electrons with energies up to 10^{14} eV, exactly in the remnant of supernovae. To date, however, there is not conclusive evidence that they produce nuclei, the dominant component of cosmic rays, in addition to electrons.

In light of this dearth of evidence, γ-ray observations from supernova remnants can offer the most promising direct way to confirm whether or not these astrophysical objects are indeed the main source of cosmic-ray nuclei below the knee. Recent observations with space- and ground-based observatories have established shell-type supernova remnants as GeV-to-TeV γ-ray sources. The interpretation of these observations is however complicated by the different radiation processes, leptonic and hadronic, that can produce similar fluxes in this energy band rendering ambiguous the nature of the emission itself.

The main goal of this work is hence to develop a deeper understanding of these radiation processes from a particular shell-type supernova remnant, namely RX J1713.7–3946, using observations of the LAT instrument onboard the Fermi Gamma-Ray Space Telescope. To achieve this purpose, an accurate modelling of the diffuse Galactic γ-ray emission is desired, since this component represents the main contribution to the γ-ray background. At energies above few tens of MeV in fact more than 80% of the observed photons are due to diffuse emission. In order to obtain accurate spectra and morphology maps of RX J1713.7–3946, a template of the diffuse background with a resolution commensurate with the LAT point-spread function at 5–10 GeV is hence developed.

Since much of small-scale structure in the diffuse Galactic γ-ray emission arises from density structure in the interstellar medium, observations of the interstellar gas are also needed. In this regard, high-resolution radio data from the International Galactic Plane Surveys (IGPS) are used to trace the gas. The full angular resolution of IGPS is not needed for the Fermi data analysis, but it is useful nevertheless because it allows to correct for atomic hydrogen self-absorption. This correction is important because it prevents the spatial structures of cold absorbing hydrogen from remaining "invisible" and avoids hence an underestimate of the total gas density in the Galaxy, increasing the accuracy of the diffuse background template.

Finally, the resulting background template corrected for the hydrogen self-absorption is used to explore the region of interest around RX J1713.7–3946 with a series of likelihood analyses. A broadband spectrum of the supernova remnant is also derived and conclusions about the nature of the emission from RX J1713.7–3946 are drawn.

The first part of the thesis is organised as follows: Chapter 1 gives an overview about the diffuse Galactic γ-ray emission and supernova remnants; Chapter 2 describes the modelling of the diffuse Galactic γ-ray emission; Chapter 3 presents the analysis of RX J1713.7–3946 using the improved background map, and the consequent results.

The last part of the thesis presents a project which is independent from the rest of the work outlined thus far. This project is the result of a collaboration with A. Baushev and M. Pohl and it is about the study of the dwarf spheroidal galaxy Segue 1. The aim of this study is to derive upper limits of the annihilation cross section of dark matter particles using observations of Fermi-LAT in direction of Segue 1. The analysis, the results, and the conclusions are presented in Chapter 4 and published in a refereed journal.

1

The Milky Way Galaxy in γ-rays

Observations of the γ-ray sky provide one of the most promising direct ways to investigate the properties of cosmic rays. Unlike charged particles, which are almost completely randomised by the Galactic magnetic field, γ-rays can be traced directly back to their origins. They originate from radiation processes of cosmic rays. So, if the emission process is known, measuring the γ-ray spectrum from a source allows to infer the energy distribution of the radiating particles. Gamma-ray astronomy therefore has a vital role to play in establishing the fundamental origin of cosmic rays.

At the beginning of this chapter a short review of the history of γ-ray astronomy is given. The following sections provide an overview of two important components of the γ-ray sky: the diffuse Galactic emission, which dominates the γ-ray sky, and supernova remnants, which are believed to be the principal sources of Galactic cosmic rays.

1.1 Introduction

The history of γ-ray astronomy dates back to the fifties when scientists like Philip Morrison raised the question about a "form of radiation which is more directly related to high-energy and nuclear processes than is optical or radio emission, and yet does not share with high-energy charged particles the complete loss of information about the position of its source" [12].

Nearly two decades after the Morrison's statement, the most significant observatories of their time, specifically designed to collect cosmic γ-rays, were operating. In 1968 in southern Arizona, scientists at the Whipple observatory started developing further the atmospheric Cherenkov technique through the first 10-m γ-ray telescope ever built. This research ended up in a class of instruments known as Imaging Air Cherenkov Telescopes (IACTs). These

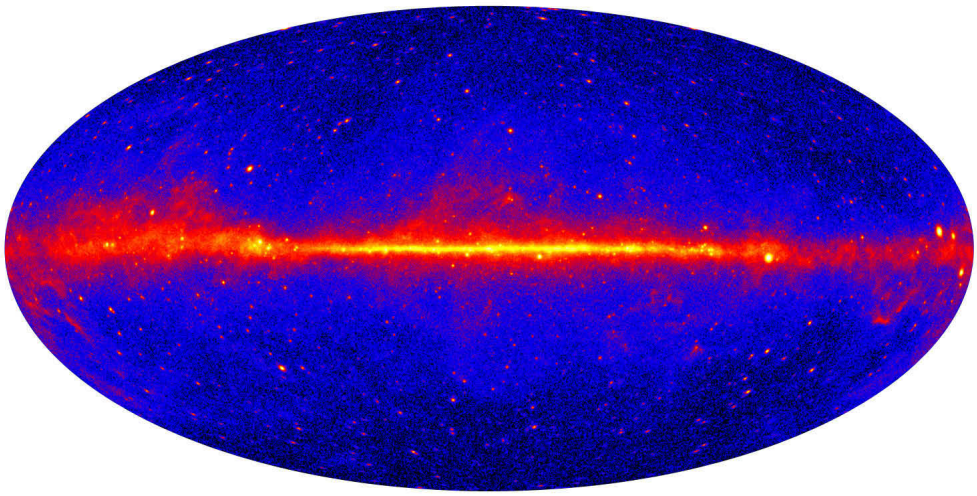

Figure 1.1: Aitoff projection of the Milky Way Galaxy at energies greater than 1 GeV based on five years of data from the LAT instrument on NASA's Fermi Gamma-ray Space Telescope. Brighter colours indicate brighter γ-ray sources. Image Credit: NASA/DOE/Fermi LAT Collaboration.

new observatories took advantage of the technique implemented by Hillas [13] to discriminate γ-ray initiated showers from those generated by protons. Enabling the search for sources of much lower γ-ray fluxes, the Hillas' method disclosed the first convincing observation of TeV emission from what would have become the standard candle of the γ-ray astronomy, namely the Crab Nebula [14]. Meanwhile, the american satellite SAS-2 [15] and the european COS-B [16] were launched (in 1972 and 1975, respectively). Despite their low angular resolution and sensitivity, they collected enough events directly from the sources and made an important contribution in providing the first complete map of the Milky Way disk in γ-rays.

Since then, a new generation of experiments has emerged. On the one hand with high-resolution space-born telescopes aboard satellites like the Compton Gamma Ray Observatory (CGRO, 1991), AGILE [17] and Fermi (2008); on the other hand with modern ground-based IACT experiments like H.E.S.S. [18], MAGIC [19], and VERITAS [20]. From the twenty-five γ-ray sources detected by COS-B to hundreds detected by Fermi and other recent IACT experiments, within an energy range spanning several orders of magnitude, γ-ray astronomy has made a remarkable step forward becoming *de facto* a new branch of physics.

From all these measurements we now know that there exist several classes of astrophysical objects responsible for such energetic emission. Rotating pulsars, accreting X-ray binaries, active galactic nuclei and supernova remnants (SNRs) are just some of them. A major role is furthermore played by the interstellar medium (ISM) and the interstellar radiation field (ISRF), two components responsible for the diffuse Galactic γ-ray emission (DGE) that permeates the entire Galaxy. The contribution of all these sources to the γ-ray sky is shown in Figure 1.1 for energies greater than 1 GeV.

In the next sections an overview of the DGE and SNRs, the two main topics of this thesis, is outlined.

1.2 The nature of the diffuse galactic γ-ray emission

Studying the DGE is important for a number of reasons. Of particular relevance for this work is its role as the primary source responsible for the luminosity of the Galaxy at high energies. More than 80% of observed photons with energy greater than few tens of MeV are in fact due to diffuse emission. This makes the DGE the primary background for Galactic sources and the primary foreground for extragalactic diffuse emission. Its comprehension is hence crucial to properly analyse extended γ-ray sources such as supernova remnants.

In addition, the DGE provides information on the acceleration and propagation of cosmic rays (CR), and it may contain information on new physics like dark matter (DM).

The physical processes responsible for the DGE are the interactions of cosmic rays with the interstellar medium and the interstellar radiation field. A deeper understanding of the diffuse emission requires therefore a deeper understanding of these three interacting elements. They are discussed in the next sections together with the processes of γ-ray production.

1.2.1 Cosmic rays

CRs are relativistic particles with a hadronic component comprising mainly protons and α particles (i.e., helium nuclei), and a leptonic component which consists of electrons, positrons, and neutrinos. The all-particle spectrum of CRs extends over many orders of magnitude from 10^6 eV up to more than 10^{20} eV. However, the relevant energies responsible for the DGE start from 10^6 eV (MeV) for the leptonic component and from 10^9 eV (GeV) for that hadronic and extend for both components up to energies of order 10^{12} eV (TeV).

Many studies have shown that low-energy CRs are partially excluded from the inner solar system due to the solar wind, a steady stream of magnetised plasma which the Sun emits in all directions. The intensity and energy spectra of these CRs undergo in fact heliospheric modulation, as shown in Figure 1.2, under the influence of a cyclic magnetic-field fluctuation and turbulence. Evidence of this modulation comes from the observed anti-correlation between solar activity, which has an alternating eleven-year cycle, and the intensity of CRs with energy below ~ 10 GeV.

Where the Sun's magnetic field is no longer a concern (i.e., $E \gtrsim 10$ GeV) the energy spectrum of CRs up to $\sim 10^{15}$ eV is well represented by a power-law with a spectral index of -2.7. In this energy range the spectrum appears rather featureless indicating that CR particles are produced in non-thermal processes and suggesting the existence of a dominant

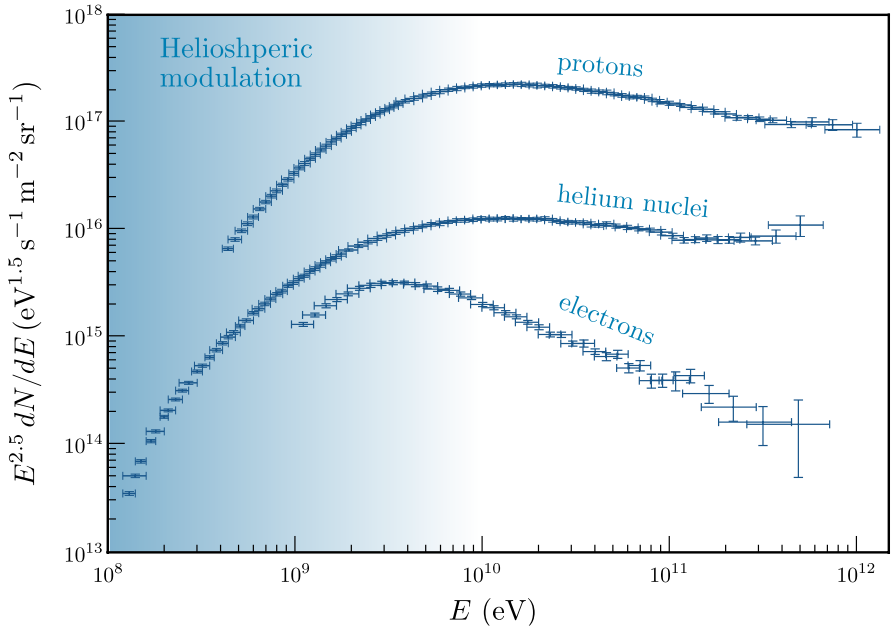

Figure 1.2: Energy spectra of hadronic and leptonic components of low-energy CRs measured by the PAMELA collaboration [1, 2]. The shaded area represents the region of the spectra affected by the influence of the solar wind. The flux of CRs with energy below about 10 GeV varies in fact significantly due to the helioshperic modulation. The plot is made using data taken from the CR Database maintained by A. Strong and I. Moskalenko [3].

source class. At higher energies, however, few structures appear, as shown in Figure 1.3, but their interpretation is still under debate. Between 10^{15} eV and 10^{16} eV in fact the CR spectrum steepens with a spectral index of -3.1 and gives rise to a feature known as the *knee*. As observed by the KASCADE-Grande experiment [21], the knee in the all-particle spectrum is caused by a decreasing of the flux of CRs with light mass ($Z < 6$). Its position in energy depends on the charge Z of the CR particles and hence is different for light and heavy elements [22]. Such a steepening might be a consequence of the breakdown of an acceleration mechanism which has reached its maximum energy. In the case of rigidity-dependent acceleration, where the rigidity of a particle is defined as

$$\rho = \frac{pc}{Ze}, \tag{1.1}$$

with p the particle momentum, c the speed of light, and Z the CR charge in units of the electronic charge e, the acceleration energy is proportional to Z. Thus, the maximum acceleration is reached by the heaviest element, the iron. As a consequence, a knee-like structure of the iron nuclei is expected to be a factor 26 higher in energy than the proton knee, i.e. form 4×10^{16} eV to 1.2×10^{17} eV. In 2011, the iron knee was indeed observed by KASCADE-Grande at 8.3×10^{16} eV [22].

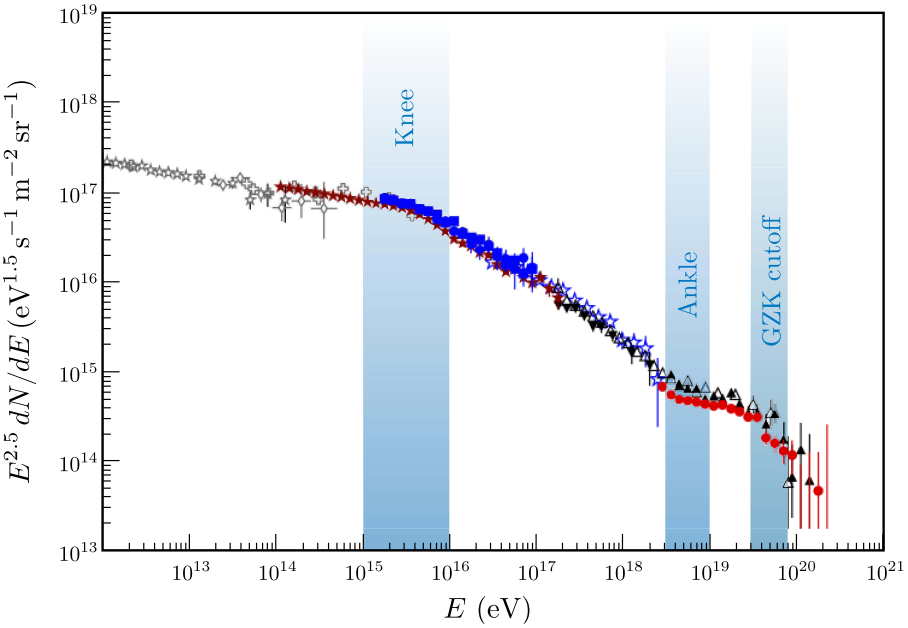

Figure 1.3: Energy spectrum of high-energy CRs measured by several experiments [4]. Despite its rather featureless behaviour the all-particle spectrum shows three main peculiarities whose characteristics are described in the text.

At about 5×10^{18} eV a flattening of the energy spectrum is observed with the index back to -2.7. This feature is known as the *ankle*. A possible explanation for the ankle might be due to a take over from the Galactic component to a harder extragalactic component [23]. Another possibility is connected with the energy losses of extragalactic protons on the cosmic microwave background (CMB) photons[1] through pair production

$$p + \gamma_{\mathrm{CMB}} \rightarrow p + e^+ + e^-.$$

This possibility is closely related to the prediction of Greisen [24] and Zatsepin & Kuz'min [25], for which at energy of roughly 5×10^{19} eV the energy spectrum should rapidly steepen giving rise to what is known as the GZK cutoff. In this case, the energy of the CR protons is high enough to allow pion-production through a Δ-resonance

$$\begin{aligned} p + \gamma_{\mathrm{CMB}} &\rightarrow \Delta^+ \rightarrow p + \pi^0 \\ p + \gamma_{\mathrm{CMB}} &\rightarrow \Delta^+ \rightarrow n + \pi^+. \end{aligned}$$

This mechanism leads to an energy loss per proton interaction of about 20% every 6 Mpc in the observer's frame [26]. Thus, extragalactic CR protons with energy above 10^{19} eV can be observed only when they originate from sources within a few 10 Mpc away.

[1] The radiation fall-out of the big bang.

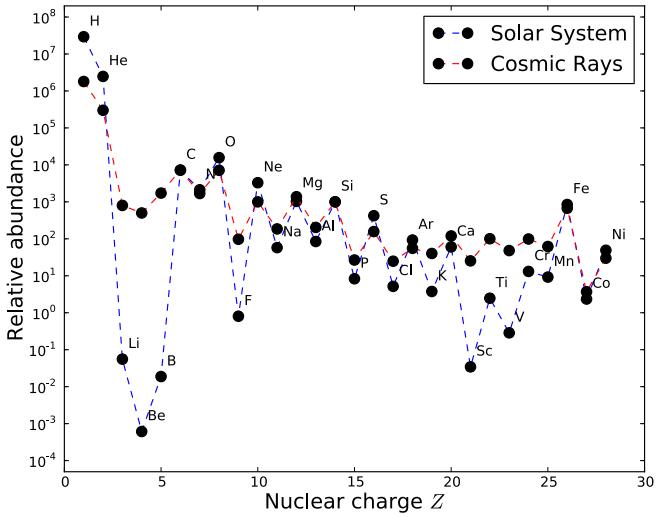

Figure 1.4: Abundances of both CR nuclei and solar system elements. The abundance distributions are normalised to Si = 10^3, and are plotted against the atomic number. The CR abundances for elements Be–Ni are CRIS measurements during the 2009–2010 solar minimum period [5]. The CR abundances for $Z < 5$ are derived from measurements by the balloon-borne instrument BESS and the GSFC instrument on the IMP-8 spacecraft. The solar system abundances are from Ref. [6].

The energy spectrum of CRs discussed thus far is the result of a combination of the injection spectrum at the sources and the complex effects of interstellar propagation. The dominant CR propagation mode is probably diffusion due to scattering on magnetic irregularities in the ISM. However, convective/advective CR transport due to the existence of Galactic winds may play a role as well. When CRs scatter off these magnetic inhomogeneities they effectively randomise their arrival direction, consequently losing any information about their sources. However, by accurately describing the gain and loss processes that affect CRs during their transport through the Galaxy, it is possible to construct models that enable us to infer the source composition from that observed in CRs.

In this regard, a comparison of the relative elemental abundances in the solar system and in the CRs reveals important information on the origin and propagation of these particles. On the basis of this comparison it appears that the two elemental abundances exhibit some noticeable differences. The light elements, lithium (Li), beryllium (Be), and boron (B), which are exceedingly rare in stars, have much higher abundances in cosmic radiation. The same applies for the heavier elements fluorine (F), scandium (Sc), titanium (Ti), and vanadium (V). These features are illustrated in Figure 1.4. These overabundances are understood quantitatively as the result of propagation effects of primary CRs, those accelerated in sources such as SNRs. During their propagation the primaries undergo in fact nuclear interactions with interstellar nuclei in a process known as *spallation*, where lighter elements (secondary

Phase	Density (atom cm^{-3})	Temperature (K)	Mass (10^9 M$_\odot$)	Tracer
Cold neutral medium	50	120	2.2	HI 21 cm emission and absorption line
Warm neutral medium	0.5	8×10^3	2.8	HI 21 cm emission line
Molecular clouds	$10^2 - 10^6$	10	1.3	CO rotational emission line
Hot ionised gas	3×10^{-3}	10^6	–	X-ray emission
Warm ionised medium	0.1	8×10^3	1	Hα emission
HII regions	$1 - 10^5$	10^4	5×10^{-2}	Hα emission

Table 1.1: A schematic classification of the phases of the ISM in the Galaxy. The neutral HI component is either clumped in cold clouds (cold neutral medium, CNM), or distributed in a diffuse manner as intercloud medium (warm neutral medium, WNM). The H_2 can exist only in dark cold clouds (molecular clouds) where it is protected against the ionising stellar ultraviolet radiation. Finally, the ionised component exhibits three phases discussed in the text.

CRs) are produced. For example, collisions of carbon (C), nitrogen (N), or oxygen (O) with protons or α particles in the ISM result in fragments of Li, Be, and B. Similarly for heavier elements such as iron (Fe) from which fragments of Sc, Ti and V are produced. On the other hand, the similarity of the more common elements is evidence that the composition of the CRs at their point of origin is very similar to that of the nebula that formed the solar system $\sim 4.6 \times 10^9$ years ago. However, it is worth mentioning that the direct observations of CRs come from the local region of the Milky Way, which is not necessarily representative of the entire Galaxy. Hence, the importance of the DGE photons which can sample much larger regions and give information on the interstellar spectra.

1.2.2 The three phases of the interstellar hydrogen

The interstellar medium acts as primary target for cosmic-ray interactions and shines in γ-rays as a by-product of these interactions. The ISM consists of a mixture of gas and dust with an average mass ratio of 100:1. From the point of view of the DGE the important component is the gas, whose density structure gives rise to the small-scale structure of the diffuse emission itself.

The interstellar gas is composed mainly of hydrogen (70% of the gas mass), with a small contribution of helium (28%) and heavier elements (2%) [27]. To first approximation the hydrogen can be schematically divided into three distinct phases: atomic (HI), molecular (H_2), and ionised (HII). The typical properties of these phases are summarised in Table 1.1. In reality, these phases are partly mixed and are strongly perturbed by winds from mas-

sive stars, supernova explosions, and other phenomena. The main characteristics of these components are considered below.

The neutral HI component

The neutral HI component emits line radiation at wavelength $\lambda_0 = 21.1$ cm, corresponding to a frequency of $\nu_0 = 1420.406$ MHz. This wavelength is characteristic of the transition between the two hyperfine sublevels of the ground state, which occurs when the spins of electron and proton flip from being parallel to antiparallel. The difference between the upper (u) and the lower (l) energy sublevel is

$$\Delta E = E_u - E_l = h\nu_0 = 5.874 \times 10^{-6} \text{ eV}, \tag{1.2}$$

where $h = 4.136 \times 10^{-15}$ eV s is the Planck's constant.

The spontaneous emission probability for this transition is given by the Einstein coefficient $A_{ul} = 2.869 \times 10^{-15}$ s^{-1}. This very small value indicates that this is a forbidden transition, with a rate of spontaneous decay

$$t_{\text{spon}} = \frac{1}{A_{ul}} = 1.108 \times 10^7 \text{ years}, \tag{1.3}$$

which is considerably larger than the time of HI atom collisions

$$t_{\text{coll}} = \frac{1}{n_{\text{H}} \sigma v} \simeq 400 \text{ years}, \tag{1.4}$$

where n_{H} is the hydrogen density taken equal to 1 cm^{-3}, σ is the geometrical cross section, and v the velocity of a HI atom with a value of 1 km s^{-1}. Since $t_{\text{coll}} \ll t_{\text{spon}}$, the spin-change process occurs in collisions amongst hydrogen atoms. These collisions have enough time to establish a local thermodynamic equilibrium (LTE) in which hydrogen atoms are in the ground state with the two hyperfine atomic sublevels populated according to the Boltzmann distribution

$$\frac{n_u}{n_l} = \frac{g_u}{g_l} \exp\left(-\frac{\Delta E}{k T_s}\right), \tag{1.5}$$

where n is the number density of atoms in each state, g is the statistical weight of each sublevel with ratio of $g_u/g_l = 3$, $k = 8.617 \times 10^{-5}$ eV K^{-1} is the Boltzmann's constant, and T_s is the excitation temperature called *spin temperature*. This temperature depends on the region of the emitted line and under normal circumstances it cannot be lower than the CMB temperature ($T_{\text{CMB}} \simeq 2.7$ K), since all the interstellar hydrogen has had a significant amount of time to be heated by CMB photons. The hyperfine transition corresponds to a

temperature $T_0 = \Delta E/k = 0.068$ K. Since from the previous consideration $T_s \geqslant T_{\rm CMB}$, it follows that $T_s \gg T_0$ and Equation 1.5 becomes

$$\frac{n_u}{n_l} \simeq \frac{g_u}{g_l} = 3, \tag{1.6}$$

with the total number density of HI atoms given by $n_{\rm HI} = n_u + n_l = 3n_l + n_l = 4n_l$. Thus, at any given time 3/4 of atoms are expected to be in the upper hyperfine sublevel, and 1/4 to be in the lower sublevel.

Turning now to quantities that can be measured in terms of *brightness temperature* T_b, which is the actual observable measured by radio surveys, the radiative transfer equation for 21 cm radiation has the general solution

$$T_b = T_s \left(1 - e^{-\tau}\right), \tag{1.7}$$

where discrete and isothermal components are assumed and the contribution from the background is ignored. The parameter τ determines the *optical depth* of the gas and it gives a sense of the level of opacity of the line. The optical depth, which is a dimensionless quantity, is defined in terms of the absorption coefficient of the line k_ν as $\tau = \int k_\nu \, ds$, where ds is the pathlenght along the line of sight. Under the assumption of LTE, k_ν can be written as

$$\kappa_\nu \simeq \frac{3c^2}{32\pi\nu_0^2} \, n_{\rm HI} \, A_{ul} \, \frac{T_0}{T_s} \, \phi(\nu) = \frac{n_{\rm HI}}{C \, \Delta v \, T_s}, \tag{1.8}$$

where $n_{\rm HI}$ is the number density of HI atoms found with Equation 1.6, and $\phi(\nu)$ is the line profile which can be defined in terms of radial velocities of the gas as $\phi(\nu) \sim c/(\nu_0 \Delta v)$, with Δv the line width at half-intensity. The constant C has been introduced for convenience and it is defined as

$$C = \frac{32\pi\nu_0^3}{3c^3 A_{ul} \, T_0} = 1.82 \times 10^{18} \ {\rm cm^{-2}} \ {\rm K^{-1}} \ ({\rm km/s})^{-1}. \tag{1.9}$$

The optical depth can be finally written as

$$\tau = \int \kappa_\nu \, ds = \frac{\int n_{\rm HI} \, ds}{C \, \Delta v \, T_s} = \frac{N_{\rm HI}}{C \, \Delta v \, T_s}, \tag{1.10}$$

where the integral of $n_{\rm HI}$ defines the *column density* $N_{\rm HI}$, in unit of atom cm^{-2}, for a given line of sight. Depending on the value of τ, the observations can be divided into two regimes: optically thin, when $\tau \ll 1$, and optically thick, when $\tau \gg 1$.

In the first case Equation 1.7 becomes $T_b \simeq T_s \tau$, meaning that optically thin emission depends only on the total column density of HI, not on the gas temperature. The column density can be worked out from Equation 1.10 and using the optically thin approximation

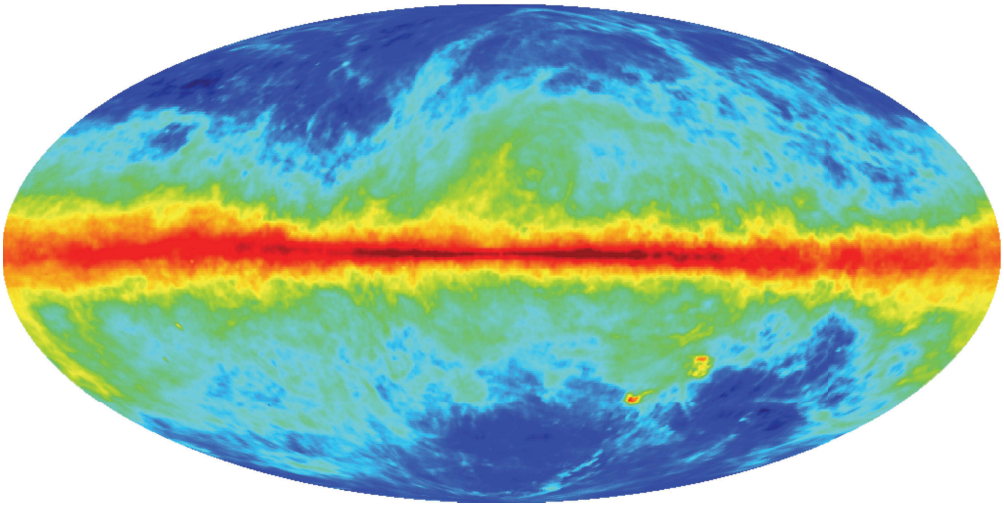

Figure 1.5: Aitoff projection of the neutral hydrogen column density from the Leiden/Dwingeloo HI Survey and the Instituto Argentino de Radioastronomia survey [7]. The brightness temperature T_b is integrated over a large range of radial velocities and the optical thin assumption is used. The integrated emission is showed in logarithmic scale within a range $0\ \mathrm{cm}^{-2} < N_{\mathrm{HI}} < 2 \times 10^{22}\ \mathrm{cm}^{-2}$. Image credit: Legacy Archive for Microwave Background Data Analysis (LAMBDA).

for T_b, N_{HI} along the observed direction is directly given by the measured T_b as follows

$$N_{\mathrm{HI}} = C\,\Delta v\,T_b. \tag{1.11}$$

In the second case, Equation 1.7 becomes $T_b \simeq T_s$. Here, only the $\tau = 1$ surface (similar to a stellar photosphere) can be seen and the observed brightness temperature T_b is independent of the column density N_{HI}, it only depends on the temperature of the gas, T_s. In this regime a formulation of the column density can be obtained by plugging τ from Equation 1.10 into Equation 1.7 and solving for N_{HI}. This procedure is often referred to as *opacity correction*. The result is

$$N_{\mathrm{HI}} = -\ln\left(1 - \frac{T_b}{T_s}\right) C\,\Delta v\,T_s. \tag{1.12}$$

In this case the determination of the column density is not, of course, accurate since assumptions on the value of T_s have to be made.

Figure 1.5 shows the HI column density distribution in the Milky Way Galaxy derived by observations of the Leiden/Argentine/Bonn (LAB) HI survey [7] with the optical thin assumption.

From Equation 1.10 it can be seen that the optically thin regime mostly applies to gas with high temperatures and/or with large internal velocity dispersion. So that "warm" can be explained as "poorly absorbing". This is the case of the warm intercloud diffuse neutral medium, whose properties are shown in Table 1.1.

The colder component of the gas, on the other hand, can have a rather small thermal broadening and temperatures below 100 K. In this case, which is the optically thick regime, "cold" means "narrow lines". Clouds in this regime are likely to be very dim in emission. However, in some case it is still possible to see them in absorption against warm HI gas behind the cloud due to a process known as *HI self-absorption* (HISA).

The HI self-absorption

This process occurs when the cloud emits less light then it absorbs from other clouds behind it. The net loss of light causes the foreground cloud to appear darker than the background field. This effect represents thus an excellent tool for mapping the structure and distribution of the otherwise invisible cold Galactic HI gas, provided a suitable background is present. This last requirement is partly fulfilled by bright HI emission found over large areas at low latitude by the most recent wide-area radio surveys.

The properties of the HISA clouds, i.e. the clouds responsible for self-absorption, can be derived by modelling the HI line emission through Equation 1.7 using the same assumptions as before but re-introducing the contribution of the background. In a simple two-component model, the aforementioned equation becomes

$$T_b = T_{\rm fg}\left(1 - e^{-\tau}\right) + T_{\rm bg}e^{-\tau}, \tag{1.13}$$

where $T_{\rm fg}$ is the spin temperature of the foreground cloud (i.e. the HISA cloud) and $T_{\rm bg}$ denotes the brightness temperatures of the background cloud. If $T_{\rm fg} < T_{\rm bg}$ then the self-absorption occurs.

In a more realistic model the emission can be described by four components [28]. In this case the HISA cloud (index 2 in the following equation) is in between a foreground (1) and a background (3) HI clouds, with the fourth component accounting for the continuum emission (4). The brightness temperature along the line of sight toward the HISA cloud (on sight line emission) now takes the form

$$T_{\rm on} = T_1\left(1 - e^{-\tau_1}\right) + T_2\left(1 - e^{-\tau_2}\right)\, e^{-\tau_1} + T_3\left(1 - e^{-\tau_3}\right)\, e^{-(\tau_1+\tau_2)} + T_4\, e^{-\sum_i^3 \tau_i}.$$

For a line of sight away from the HISA cloud (off sight line emission), the brightness temperature becomes

$$T_{\rm off} = T_1\left(1 - e^{-\tau_1}\right) + T_3\left(1 - e^{-\tau_3}\right)\, e^{-\tau_1} + T_4\, e^{-(\tau_1+\tau_3)}.$$

Assuming that the optical depth of both foreground (τ_1) and background (τ_3) clouds is small,

the difference between the on and off sight line observed intensities is then

$$T_{\rm on} - T_{\rm off} = (T_2 - T_4 - p\,T_{\rm off})\,\left(1 - e^{-\tau_2}\right), \tag{1.14}$$

where $p = T_3\,\left(1 - e^{-\tau_3}\right)/T_{\rm off}$ and it represents the fraction of HI emission originating behind the HISA cloud. In the multicomponent model the condition for self-absorption is $T_{\rm on} < T_{\rm off}$.

The quantities $T_{\rm on}$ and $T_{\rm off}$ are measured by radio surveys as well as T_4 which represents the continuum emission. The only unknown quantities are hence $T_2 \equiv T_s^{\rm HISA}$, $\tau_2 \equiv \tau^{\rm HISA}$, and p. So, in order to estimate the HI column density of HISA clouds, they have to be constrained. A method is described in Chapter 2. Once these values are known, the column density $N_{\rm HISA}$ can be estimated using Equation 1.10.

The molecular component

Molecular hydrogen is found in regions where it is shielded from ultraviolet radiation which causes its photodissociation. Thus, H_2 gas can only survive in cold and dense dark clouds. Containing two identical hydrogen atoms, H_2 is highly symmetric. Due to this symmetry, the molecule has no dipole moment and all ro-vibrational transitions within the electronic ground state are quadrupolar with low spontaneous coefficient A_{ul} values[2]. Hence, direct observation of this molecule is difficult.

However, a way to trace H_2 is from observations of the carbon monoxide molecule $^{12}C^{16}O$ (hereafter CO). Contrary to H_2, CO is made up of two different atoms which have different charge. Such a difference contributes to form a significantly asymmetric charge distribution which gives rise to a polar molecule. Rotating around its centre of mass the CO polar molecule radiates. Its rotational energy changes according to the quantum-mechanical selection rule $\Delta J = \pm 1$, where J is the angular-momentum quantum number. The CO molecule is observed in its $J = 1 \rightarrow 0$ transition at a wavelength of 2.6 mm, corresponding to a frequency of $\nu_0 = 115.271$ GHz. The energy released going from $J = 1$ to $J = 0$ is

$$\Delta E_{\rm rot} = h\nu_0 = 4.767 \times 10^{-4}\ {\rm eV}, \tag{1.15}$$

equivalent to a temperature $T_0 = \Delta E_{\rm rot}/k = 5.532$ K, which is low enough to easily excite CO even in cold molecular clouds.

The spontaneous emission probability is $A_{ul} = 7.202 \times 10^{-8}\ {\rm s}^{-1}$, with a spontaneous emission rate of

$$t_{\rm spon} = \frac{1}{A_{ul}} \simeq 5.357\ {\rm months}. \tag{1.16}$$

[2]The transition rate decreases by a factor of about 1000 from one multipole to the next, so the highest multipole transitions are most unlikely to occur.

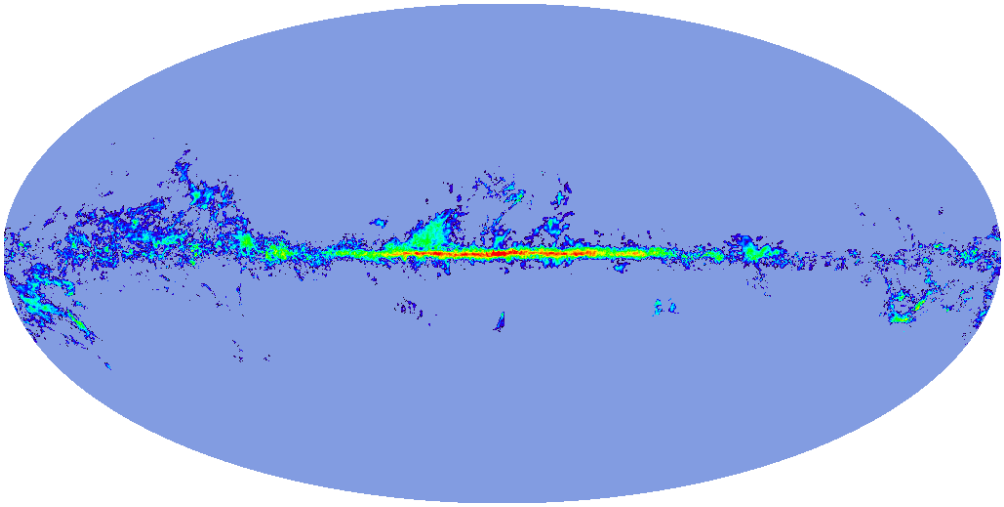

Figure 1.6: Aitoff projection of the velocity-integrated CO brightness temperature from 37 individual surveys [8]. The integrated emission is showed in logarithmic scale within a range 1.5 K km s^{-1} < $W_{\rm CO}$ < 200 K km s^{-1}. Image credit: Legacy Archive for Microwave Background Data Analysis (LAMBDA).

This time is much longer than the average time between molecular collisions in an interstellar molecular cloud with density 10^2 to 10^3 H_2 molecules cm^{-3} (H_2 is by far the most abundant molecule). Then, collisions with H_2 dominate over other processes in determining the relative populations of the upper rotational levels. The Galactic distribution of H_2 can thus be determined indirectly by observation of CO.

A commonly used method to derive the column density of molecular hydrogen $N_{\rm H_2}$, in cm^{-2}, is from the velocity-integrated line intensity $W_{\rm CO}$, in units of K km s^{-1}, defined as

$$W_{\rm CO} = \int T_b(J = 1 \rightarrow 0)\, dv \tag{1.17}$$

where v is the radial velocity of the gas. Figure 1.6 shows the $W_{\rm CO}$ map in the Milky Way. Thus, the column density $N_{\rm H_2}$ writes

$$N_{\rm H_2} = X_{\rm CO} W_{\rm CO}, \tag{1.18}$$

where $X_{\rm CO}$ is known as *CO-to-H_2 conversion factor*. The $X_{\rm CO}$ factor depends on the metallicity and the ultraviolet radiation background which regulate the CO abundances [29]. In clouds with low metallicity or strong ultraviolet radiation background, the CO abundance is smaller. Therefore, the conversion factor must increase to an appreciable extent. However, in clouds with large CO abundance the emission line is fully saturated and $X_{\rm CO}$ is directly proportional to the molecular column density. The measurement of metallicity gradient in our Galaxy can be used to estimate the distribution of $X_{\rm CO}$. It has been shown that $X_{\rm CO}$

increases with Galactocentric radius although its radial steepness is largely uncertain [30].

The ionised medium

The ISM can be ionised by several mechanisms giving rise to different kinds of ionised components whose distinction is not always completely clear. Nonetheless, three main components can be identified. The HII regions are one of them. They are well-defined entities surrounding bright O and B stars that form when far ultraviolet radiation originating by these stars ionises and heats the surrounding gas. The far ultraviolet radiation, however, can escape the HII regions and be absorbed by atoms. In this way, outside the HII regions, a second component in form of diffuse warm ionised medium develops. Finally, a large fraction of the ISM contains a component of hot and very-low density gas with a large vertical extent from the Galactic plane. This gas owes its existence to the presence of strong shock waves, driven by supernova explosions, as confirmed by X-ray observations [31].

Overall, all these components in the ionised medium make a small contribution to the γ-ray production compared to that of HI and H_2.

From observations of the hydrogen components both gas distances (from the Doppler-shifted velocity and Galactic rotation models) and density informations (from Equations 1.11, 1.12, and 1.18) can be deduced. Thus, measurements from all-sky surveys yield the hydrogen space-averaged density as a function of position in the Galaxy, i.e. the Galaxy's geometry. From the perspective of the DGE this is a crucial point. Such a geometry reflects in fact that of the DGE itself, since hydrogen atoms and molecules are one of the main targets of CRs from which photons originate. The most noticeable evidence of this is the intense emission from the Galactic plane where most of the interstellar gas lies, which is the dominant feature of the high-energy γ-ray sky.

The results obtained in this section will be used in Chapter 2 to derive the column densities of the ISM from astrophysical observations.

1.2.3 Interstellar radiation field

Besides ISM, the Galaxy is filled with a radiation field made up of contributions from starlight, emission from dust, and CMB photons. The energy spectrum of the radiation field can be divided into three wavelength ranges: the ultraviolet-visible-near infrared region ($\lambda \lesssim 8\,\mu$m), which is produced almost entirely from stars, the middle- and far-infrared region ($8\,\mu\text{m} \lesssim \lambda \lesssim 1000\,\mu$m), where warm and cold dust are the dominant components, and the far infrared-microwave region ($\lambda \gtrsim 1000\,\mu$m), with the 2.7 K microwave background as the main radiation field. Figure 1.7 illustrates these contributions in terms of the local energy

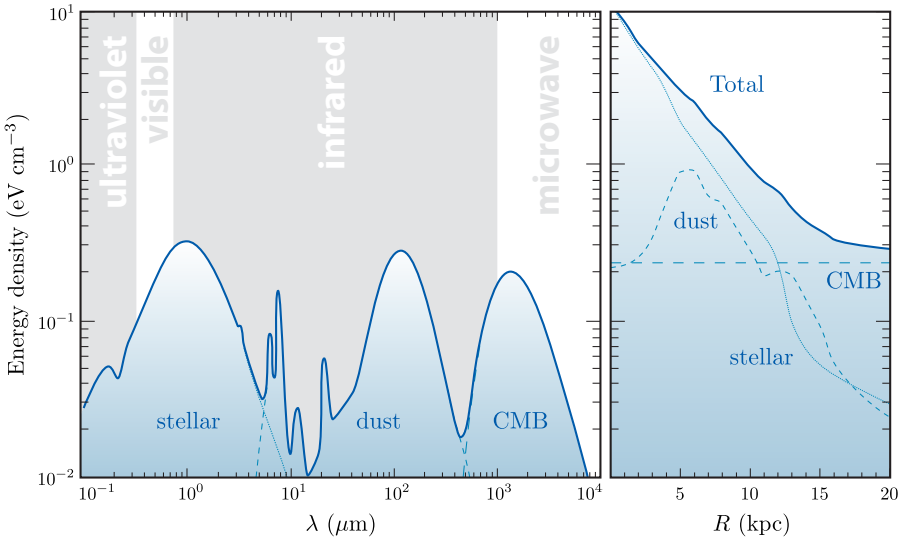

Figure 1.7: Estimated energy density spectra of the ISRF in the Galactic plane. On the left it is shown the spectrum plotted against the wavelength for a distance of 8 kpc from the Galactic centre. The plot on the right is the spectrum as a function of Galactocentric radius. The two spectra show the three contributions due to stellar, dust, and cosmic microwave background emission. The plots are adapted from Ref. [9, 10].

density of the field, in the vicinity of the Sun, against the wavelength (left-side plot) and the total energy density of the field against the Galactocentric distance (right-side plot).

The first region is dominated by the emission from the stellar disk and red giants. It shows a wide peak at $\lambda \sim 1\,\mu$m, in the near infrared, corresponding to a local energy density of about 0.4 eV cm^{-3}. A second smaller peak is also visible at $\lambda \sim 0.15\,\mu$m in the ultraviolet, which is thought to be due to early type stars (OB stars) [32].

The emission from interstellar dust plays a major role in the second region. Such emission is the result of starlight photons which are absorbed by small grains in the ultraviolet-visible region and re-emitted in the infrared. During this process the dust is heated by the absorbed starlight photons in a stochastic way that results in transient temperature spikes [33]. In particular, infrared observations have shown that the diffuse ISM radiates strongly in emission features at 3.3, 6.2, 7.7, 8.6, and 11.3 μm [34].

Finally, the last region is due to radiation field from the CMB photons. Given its temperature this radiation is at wavelengths where the ISM is very transparent and hence its effects are very limited. However, it may play some role in populating the rotational levels of interstellar molecules because many of them have transitions in this wavelength range. This however is not the case of CO molecules, as it was shown in Section 1.2.2.

The radiation fields described in this section are an important component for the diffuse γ-ray emission since a substantial fraction of the DGE is produced via inverse Compton process (see next section) of relativistic CR electrons scattering off these low-energy photons.

1.2.4 Processes of γ-ray production

The spectrum of the radiation of a black body of temperature T is described by the Planck's law

$$I_\nu(T) = \frac{2}{c^2} \frac{h\nu^3}{e^{h\nu/kT} - 1}, \tag{1.19}$$

with a peak at energies $E_{\max} = h\nu_{\max} \simeq 2.821\, kT$. For a thermal radiator with significant emission in γ-rays of about 1 MeV, T would be of order 10^{10} K. This large value means that thermal production is not the typical process for γ-rays.

Three basic non-thermal radiative processes are instead capable of producing DGE, whose energy spans many orders of magnitude from MeV to TeV. The nature of these processes depends on the type of interacting CRs.

CR leptons, predominantly electrons, radiate efficiently when they accelerate or decelerate quickly. Interactions between CR electrons and interstellar gas give rise to non-thermal *bremsstrahlung radiation*. The mean energy of a bremsstrahlung photon is typically half of the radiating relativistic electrons

$$\langle E_\gamma \rangle \simeq E_e/2, \tag{1.20}$$

for $E_e > 10$ MeV. This radiation contributes significantly to the DGE spectrum at low energy and it is produced by the low-energy tail of the CR spectrum.

CR electrons can also transfer a large fraction of their energy to low-energy photons of the ISRF, by scattering them off in a process known as *inverse Compton* (IC). Depending on the energy involved in this process, two regimes can be identified. In the so-called "Thomson limit", photons with the mean energy $\langle E_\gamma \rangle$ receive on the average an energy given by

$$\langle E_{\gamma'} \rangle \simeq \frac{4}{3} \langle E_\gamma \rangle \left(\frac{E_e}{m_e c^2} \right)^2, \tag{1.21}$$

where E_e and m_e are the initial energy and the rest mass of the electron. This regime applies when $E_\gamma\, E_e \ll (m_e c^2)^2$. Equation 1.21 permits hence to estimate the contribution of different background radiation fields to the resulting spectrum of γ-rays. For instance, electrons of $E_e \simeq 50$ GeV when interact with low-energy microwave ($\langle E_\gamma \rangle \simeq 10^{-4}$ eV), infrared ($\langle E_\gamma \rangle \simeq 10^{-2}$ eV), or optical ($\langle E_\gamma \rangle \simeq 1$ eV) photons give rise to high-energy photons of about 6 MeV, 95 MeV, or 10 GeV respectively. On the other hand, in the so-called "Klein-Nishina" limit which is satisfied when $E_\gamma\, E_e \gg (m_e c^2)^2$, the scattered photon energy equals the radiating relativistic electron energy

$$\langle E_{\gamma'} \rangle \simeq E_e. \tag{1.22}$$

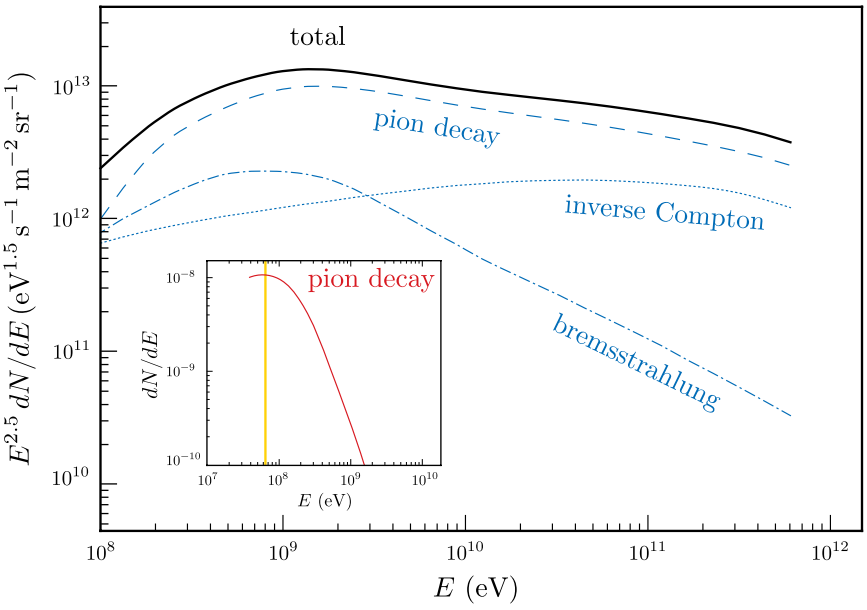

Figure 1.8: The predicted diffuse γ-ray spectra from the propagation model described in Chapter 2. The various production processes are shown: inverse Compton-interactions with the ISRF, non-thermal bremsstrahlung, and decay of neutral pions produced in nuclear interactions of CRs. The inset denotes the characteristic π^0-decay hump at 70 MeV.

This limit is characterised by a cutoff in the spectrum due to a take over from recoil effects in the interaction which low the cross-section value [27]. The detection of such a feature might be used to reveal the IC origin of the radiation. The IC emission gives a substantial contribution to the DGE spectrum at high energies.

In the case of CR hadrons, mostly protons and α-particles, the interaction takes place through inelastic collisions with the interstellar gas producing mainly neutral and charged pions (π^0, $\pi^{\pm}$). The charged pions decay via muons into secondary electrons, positrons, and neutrinos. If the secondary electrons and positrons are confined long enough in the Galactic disk, they produce non-thermal bremsstrahlung γ-rays. Each neutral pion, on the other hand, successively decays into a pair of equal-energy γ-rays[3] emitted in the direction of propagation of the pion. In the reference system of the pion, each photon has an energy $1/2\, m_{\pi^0} c^2 \simeq 70$ MeV, where $m_{\pi^0} = 134.976\ \mathrm{MeV}/c^2$ is the rest mass of the pion. Then, by Lorentz transformation, the γ-ray energy in the reference system of the observer is

$$E_\gamma = \frac{1}{2}\, \gamma_{\pi^0} m_{\pi^0} c^2 (1 + \beta_{\pi^0} \cos\theta), \tag{1.23}$$

[3]The branching fraction for this decay is 98.8%.

where γ_{π^0} is the Lorentz factor of the neutral pion, $\beta_{\pi^0} = v/c$ with v the pion velocity, and θ is the direction with respect to the line of sight.

The characteristic spectra of these processes that all together form the DGE spectrum are shown in Figure 1.8. The inset is the characteristic π^0-decay spectrum with its symmetry around 70 MeV.

1.3 Supernova remnants

After having discussed in previous sections the properties of the CRs and those of the main components of the ISM and the ISRF, as well as the CR interactions that these components undergo to finally give rise to the DGE, the discussion will now be focussed on one of the most likely classes of astrophysical objects considered to be the main source of CRs with energy up to $\sim 10^{15}$ eV, namely the supernova remnants.

Radio observations have long been drawing attention to supernova remnants as principal sources of GeV-scale electrons. Compelling evidence for acceleration of cosmic-ray electrons in these sources comes also from observations of non-thermal X-ray radiation in supernova remnants like SN 1006, which require electrons with energies of at least $\sim$ 100 TeV [35]. However, a conclusive evidence that supernova remnants can accelerate cosmic-ray hadrons, that dominate the energy budget of cosmic rays, in addition to electrons is still missing.

In this section, an overview of the main features of supernova remnants and their connection with cosmic rays and γ-rays is described.

1.3.1 Introduction

The dynamical state of the ISM is strongly affected by supernovae (SNe), rare events (3 ± 1 per century [36]) that characterise the last stage of stellar evolution. Depending on the mass of the progenitor stars and their circumstellar environment, different types of SNe can occur, which can be divided into two main categories: core-collapse of massive stars (Type II, Ib and Ic) and thermonuclear explosion of white dwarf stars (Type Ia).

When a star explodes as a SN, it ejects into outer space a mass of material ($M_{\rm ej}$) with a typical kinetic energy of $E_0 \equiv 10^{51} E_{51}$ erg, where for most SNe $E_{51} \simeq 1$ [37]. Depending on the supernova type, $M_{\rm ej}$ can range from $\sim 1.4\,M_\odot$ for Type Ia, where the Sun's mass is $M_\odot = 1.988 \times 10^{30}$ kg, to about 10–20 $M_\odot$ for a core-collapse event. The ejected stellar material (hereafter ejecta) will have a range of velocities, with the outermost material moving fastest at velocity

$$v_{\rm ej} = \left(\frac{2E_0}{M_{\rm ej}}\right)^{1/2} \simeq 1 \times 10^4 \text{ km s}^{-1}\, E_{51}^{1/2} \left(\frac{M_\odot}{M_{\rm ej}}\right)^{1/2}. \tag{1.24}$$

A characteristic initial velocity is hence of order $\sim 10^4$ km s^{-1} for a Type Ia and $\sim 10^3$ km s^{-1} for a core-collapse. Such velocities are 3–4 orders of magnitude greater than the sound speed in the surrounding material ($c_s \simeq$ 1–10 km s^{-1}), corresponding to a Mach number $\mathcal{M} \equiv v_{\rm ej}/c_s \sim 10^3$. Because of this extremely high $\mathcal{M}$-value, a fast shock wave (the forward shock) forms at the leading edge of the expanding ejecta. All the matter interior to this shock surface defines the SNR.

1.3.2 The evolution of the SNR

Subsequent evolution of SNRs has been widely studied either numerically or analytically. Here, a simple standard picture of such evolution assuming a spherically symmetric explosion of a star in a uniform medium is considered. This picture assumes three main stages (or phases) of the evolution of the SNR, as illustrated below.

The free-expansion phase

In the first days after the explosion, the ejecta continue to expand almost freely at nearly constant velocity since their density dominates that of the ambient medium. Meanwhile, their temperature drops due to adiabatic expansion. Behind the forward shock (FS), that propagates outward from the centre of the remnant, the compressed ambient medium starts accumulating and it gives rise to a shell of shock-heated gas. Between this shell and the more inner ejecta a contact discontinuity is created.

The free-expansion phase continues as long as the density of the ejecta dominates over that of the shock-heated gas. The time when this happens corresponds to $t_0 = R_s/v_{\rm ej}$, with R_s the radius of the shock wave defined by

$$R_s = \left(\frac{3M_{\rm ej}}{4\pi\rho_{\rm gas}}\right)^{1/3} \simeq 6 \times 10^{13}\ {\rm km}\ \left(\frac{M_{\rm ej}}{M_\odot}\right)^{1/3}, \tag{1.25}$$

where $\rho_{\rm gas}$ is the mass density of the pre-shock ambient gas (taken $\sim 1.7 \times 10^{-27}$ kg cm^{-3}), and the initial velocity $v_{\rm ej}$ is given by Equation 1.24. The free-expansion phase lasts hence from $\sim$ 100 years to almost 1000 years.

The Sedov-Taylor phase

For $t \gtrsim t_0$, the mass of the swept-up and shock-heated ambient gas becomes large compared to the original mass $M_{\rm ej}$. At this stage the pressure of the shock-heated gas prevails and pushes back into the ejecta. This gives rise to a reverse shock (RS) which decelerates and heats the ejecta itself. Now the remnant has a double-shocked structure with a FS

propagating outward into the ambient medium and a RS propagating inward, slowing and shock-heating the ejecta.

The shock-heated gas in the shell is still hot and radiative energy losses are small compared with its internal energy. The rate of expansion is determined only by the initial explosion energy E_0 and the external density $n_{\rm gas}$. This expansion phase can therefore be regarded as adiabatic, the cooling of the gas is only due to the expansion.

In the fifties Taylor [38] and Sedov [39] independently derived an exact self-similar solution for such a pressure-driven explosion. The observable quantities inferred from their analysis are

$$R_s = 1.54 \times 10^{14}\ \mathrm{km} \left(\frac{E_{51}}{n_{\rm gas}}\right)^{1/5} t_3^{2/5} \tag{1.26}$$

$$v_s = 1950\ \mathrm{km\ s^{-1}} \left(\frac{E_{51}}{n_{\rm gas}}\right)^{1/5} t_3^{-3/5} \tag{1.27}$$

$$T_s = 5.25 \times 10^{7}\ \mathrm{K} \left(\frac{E_{51}}{n_{\rm gas}}\right)^{2/5} t_3^{-6/5} \tag{1.28}$$

where R_s, v_s, and T_s are the radius, velocity, and temperature respectively of the shock wave with $t_3 \equiv t/10^3$ year. This phase lasts about 10^4 years.

The radiative phase

As the SNR continues to expand it sweeps up cold ambient gas, becoming cooler as its mass increases. Its evolution at this stage quits the Sedov-Taylor phase (i.e. the adiabatic phase) and it enters the so-called radiative phase. When it reaches a critical temperature of about 10^6 K, the ionised atoms start capturing free electrons and losing their excitation energy by radiation. Due to the efficient radiative cooling the thermal pressure in the post-shock region decreases and the FS weakens and slows down to a much lower Mach number.

In the end, the FS becomes sub-sonic and eventually stalls. The diffuse SNR finally merges with the surrounding ambient gas on a timescale of 10^5–10^6 years, chemically enriching the ISM with heavy elements.

Although the phases of SNR evolution can be fairly well described by this simple picture, there are many deviations that should be mentioned. One of this is that the progenitors of SNRs are massive hot stars that can have copious stellar winds. Thus, at the time of the explosion, the supernova is surrounded by a low-density bubble created by these stellar winds. As long as the ejecta are expanding into this low-density region, they will sweep up very little mass, and the free expansion phase will be prolonged. Another complication is

that the ambient medium is not uniform. Thus, some part of the shock front might pass through a dense cloud and an other through rarefied gas, with the result that the remnant may experience different phases at the same time.

1.3.3 CR origin and acceleration in SNRs

The energy density of CRs implies the existence of powerful accelerators in the Milky Way. SNRs have long been thought to be those accelerators. The power required to accelerate particles up to 10^{15} eV (the knee), beyond which the spectrum of Galactic CRs starts to deviate from a simple power-law form, can be estimated by energetic considerations as follows. Defining the number density of CRs with velocity v as

$$n(E) = \frac{4\pi}{v} F(E), \tag{1.29}$$

where $F(E) = dN/dE$ is the same measured spectrum shown in Figures 1.2 and 1.3, the energy density of CRs can be obtained by

$$\rho_E = \int E\, n(E)\, dE = 4\pi \int \frac{E}{v} \frac{dN}{dE}\, dE, \tag{1.30}$$

where dN/dE is used above 1 GeV to avoid uncertainties due to influence of solar modulation. As it was pointed out in Section 1.2.1, CRs belong to two families of particles, namely leptons and hadrons. Summing Equation 1.30 over all nuclei gives the total energy density of hadrons $\rho_E \simeq 0.5$ eV cm^{-3}. The same equation gives the leptonic contribution $\rho_E \simeq 0.006$ eV cm^{-3}. The comparison of these two results shows that from the perspective of the energy budget the hadron component dominates. The key issue in understanding the origin of CRs is therefore the acceleration of hadrons.

The measured abundances of radioactive CR isotopes, in particular ^{10}Be, indicate that the mean residence time of CRs in the Galaxy is $\tau_{\rm CR} \sim 10^7$ years. Assuming a CR confinement region with a volume V of approximately 10^{68} cm^3, the CR energy content of the Galaxy is $E_{\rm CR} = \rho_E V = 5 \times 10^{67}$ eV $= 8 \times 10^{55}$ erg. From such energy is straightforward to estimate the production rate of CRs

$$Q_{\rm CR} = \frac{E_{\rm CR}}{\tau_{\rm CR}} \simeq 10^{41} \text{ erg s}^{-1}. \tag{1.31}$$

Assuming the typical SN kinetic energy E_0 of order 10^{51} erg, a SN rate $r_{\rm SN}$ of 1 every 33 years, and an efficiency $\varepsilon_{\rm SN}$ for converting E_0 to CR particles of 10%, then the energy production rate is

$$Q_{\rm SN} = E_0\, r_{\rm SN}\, \varepsilon_{\rm SN} \simeq 10^{41} \text{ erg s}^{-1}. \tag{1.32}$$

Despite the treatment is not rigorous, this result is a strong indication that the source of energy for CR acceleration are compatible with the shock waves driven by the expansion energy of SN ejecta.

The only theory sufficiently well developed which allows effective conversion of the kinetic energy of bulk motion to relativistic leptons and hadrons is the *diffusive shock acceleration* (DSA), or first-order Fermi acceleration. The idea behind this theory is that charged particles gain supra-thermal energies by being repeatedly reflected by magnetic turbulence ahead of and behind the shock so that they propagate diffusively (see Ref. [40] for a comprehensive review). Despite early works inferred a maximum energy of accelerated particles $E_{\rm max}$ of only 10^{14} eV [41], further studies have shown that the magnetic field upstream the shock can be strongly amplified due to instabilities driven by CRs themselves [42]. Evidence of the magnetic field amplification come from X-ray observations of narrow filaments at the outer edge of SNRs (e.g., SN 1006 [43]). This effect can greatly boosts $E_{\rm max}$ up to a limit determined by [44]

$$E_{\rm max} \propto B\, v_s^2\, t_{\rm age} \tag{1.33}$$

where B is the magnetic field, $t_{\rm age}$ is the age of the supernova remnant, and v_s is the shock velocity. The strong dependence on the shock velocity implies that $E_{\rm max}$ falls rapidly once the SNR enters the Sedov-Taylor phase and starts decelerating. CRs can thus be accelerated up to 10^{15} eV but only during the young phase of the SNR, that is the free-expansion phase. The efficient particle acceleration is maintained for $\sim 10^3$ years after which SNRs gradually lose their ability to efficiently accelerate particles.

1.3.4 γ-ray signatures of SNRs

Radiation from shell-like SNRs mainly consists of thermal emission from shock-heated gas and non-thermal emission from shock-accelerated particles. Four basic radiative processes are responsible for such emission, in particular for the non-thermal emission. Three are the same as those seen for the DGE and the fourth is the *synchrotron radiation* process, being the result of high-energy electrons spiralling in a magnetic field.

The synchrotron emission is the only one to be firmly identified in SNRs and is capable of producing photons from radio to soft X-ray (few tens of keV) band. Moreover, the same electron population giving rise to synchrotron radiation should produce TeV emission via IC scattering. Thus, from spatial correlation between X-ray and TeV-band emission it would be possible to rule out or to confirm the IC origin of such emission in favour or against the hadronic scenario. Nevertheless, if the TeV emission is of leptonic origin, the spectra in X-rays and γ-rays should also be similar.

Even though synchrotron emission only indicates the presence of relativistic electrons, a

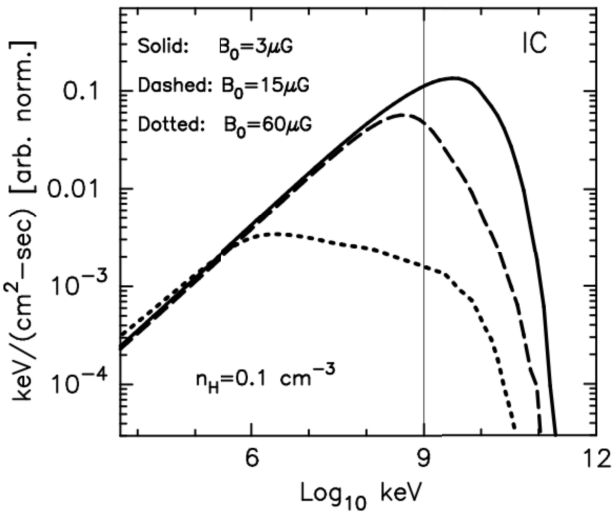

Figure 1.9: Expected GeV-TeV band γ-ray emission from inverse Compton scattering off the microwave background on highly relativistic electrons [11]. Shown are three spectra for different values of the magnetic field strength upstream of the SNR forward shock. The thin vertical line marks 1 TeV photon energy.

direct signature of CR hadrons is provided by γ-rays generated in the decay of neutral pions, as described in Section 1.2.4. The γ-ray spectrum is symmetric about 70 MeV in a log-log representation (see the inset in Figure 1.8) and approximately traces the energy distribution of parent protons at energies greater than a few GeV. The detection and identification of γ-rays with this characteristic spectral feature directly from young SNRs would be therefore a clear evidence of protons and nuclei acceleration at shock fronts. The interpretation of the π^0-decay spectrum is however complicated because IC emission can produce similar fluxes in the GeV-TeV band. This is particularly evident in the presence of a strong magnetic field. In this case in fact the energy losses may produce a change in the electron spectrum which affects the expected IC spectrum in a way that it mimics that of the π^0-decay, as shown in Figure 1.9 in the case of magnetic field of 60 μG. Hence, the need of observing a large enough energy range in order to disentangle these two spectra.

2

Modelling the diffuse Galactic γ-ray emission

One of the aims of this work is to develop a high-resolution DGE background model which can be used as background map for the Fermi-LAT data analysis of extended supernova remnants. Since small-scale features in the DGE reflect the spatial distribution of the ISM, high-resolution radio observations, which can trace the interstellar gas, from the most recent wide-area surveys are necessary to achieve a more detailed view of cloud structures. In particular, data from the International Galactic Plane Survey (IGPS) which covers almost 90% of the Galactic plane with an angular resolution of $\sim 1'$ are used in this work. The characteristics of this survey, which in fact is a consortium of three surveys, are presented in Section 2.3.1.

The full angular resolution of the IGPS is however not needed for the Fermi-LAT data analysis, but it is useful nevertheless because it permits correcting for atomic hydrogen self-absorption (HISA). Observations of HISA against diffuse background HI emission provide in fact a direct view of the spatial structure of cold atomic gas and therefore a direct method to estimate the cold atomic hydrogen column density of the otherwise invisible absorbing hydrogen clouds.

The distribution of the ISM along with that of ISRF and CRs is finally used to derive the DGE. The resulting high-resolution DGE background model covers only the Galactic plane, where the measurements of the IGPS are available. However, this is exactly where the intensity of that background is high, and the statistical precision of the Fermi data ensures high angular resolution. Furthermore, this is also where the majority of supernova remnants are.

The first section of this chapter presents a cursory overview of what the possible approaches used to model the DGE are. The following sections describe theoretical models and techniques employed to obtain the distributions of CRs and their targets in order to

finally derive a more physically plausible model for the DGE in the Galactic plane.

2.1 A brief introduction to the DGE modelling

Different approaches can be adopted to model the DGE. A phenomenological approach consists in modelling the γ-ray intensity as a linear combination of contributions coming from point-like sources (S_k), CRs interactions with different gas phases (X_j), inverse Compton scattering emission (I_{IC}), and an isotropic term (I_{ISO}) which accounts for the extragalactic γ-ray background. For this kind of models the terms in the linear combination can differ in number and nature, depending upon the model assumptions, but in the general form the intensity of the DGE (I_{DGE}) in a direction (ℓ, b), for a given energy band, may be modelled as

$$I_{DGE}(\ell, b) = \sum_{i}^{M} \left[\sum_{j}^{N} q_i(j)\, X_j(\ell, b) \right] + \sum_{k}^{P} S_k + I_{IC} + I_{ISO} \tag{2.1}$$

where q_i are the γ-ray emissivities per H atom, the index i represents the i^{th} Galactocentric radius, the index j refers to the specific gas components (i.e. HI and CO), and the sum over k accounts for all the point-like γ-ray sources. This model is then used to fit γ-ray observations in order to find the best-fit parameter values: the emissivities q as well as the I_{ISO} component. This approach is based on simple assumptions: the ISM is transparent to the γ-rays, CR densities do not vary over the scale of interstellar complexes, and CRs penetrate clouds uniformly. Thus, to first order the linear combination 2.1 is justified. This approach has been used in many works. Of considerable interest are those by Lebrun et al. [45] with the COS-B data, by Hunter et al. [46] with the EGRET data, and the more recent analyses by the Fermi-LAT collaboration [47, 48, 49].

A more theoretical approach to model the DGE is based on CR propagation models. DGE originates from high-energy CRs interacting with ISM and ISRF. Thus, modelling the γ-ray emission requires knowledge of the distributions of CRs along with those of their targets. Using the distribution of CR sources and the injection spectra of CRs, the intensities and spectra of CRs can be derived by solving the transport equation which governs their propagation in the Galaxy. The transport equation can be computed analytically, semi-analytically, or numerically. The resulting CR distributions are then used with those derived for ISM and IRSF to finally obtain the DGE.

In the present work the DGE is obtained using this second approach. The CR propagation model considered here accounts for diffusive re-acceleration in the interstellar medium with a Kolmogorov spectrum of interstellar turbulence, along with momentum losses, nuclear fragmentation, and radioactive decay. The transport equation of the model is numerically

Parameter	Nuclei	Electrons	Description
ρ_1	9×10^3	4×10^3	1^{st} break rigidity of the spectrum (MV)
ρ_2	–	1×10^9	2^{nd} break rigidity of the spectrum (MV)
γ_1	1.82	1.6	index below the 1^{st} break
γ_2	–	2.5	index in between the two breaks
γ_3	2.36	5.0	index above the 2^{nd} break

Table 2.1: Main input parameters of the diffusive re-acceleration model used in this work. All injection parameters of the model are adjusted to agree with CR observations.

solved by the GALPROP code, version 54 [50]. The choice of GALPROP relies on the possibility of constraining the most important astrophysical inputs by using CR observations of different experiments, hence obtaining more realistic results. A description of the whole procedure is outlined in the next sections.

2.2 CR injection and propagation

GALPROP solves numerically the transport equation for all CR species, starting with a given CR source distribution. SNRs are believed to be the principal sources of CRs. However, their Galactic distribution is not well determined. Therefore, a parametrized distribution [51], chosen to agree with the EGRET data, is used in the model.

The injection spectra for all CR nuclei species and primary CR electrons are assumed to follow a rigidity-dependent function, where a particle rigidity is defined by Equation 1.1. For nuclei spectra one break rigidity is assumed, corresponding to two spectral indices. The electron spectrum accounts for two break rigidities and three spectral indices. All spectral indices (γ_i, $i = 1, 2, 3$) and break rigidities (ρ_1, ρ_2) are determined by tuning the model to observations [52] and are summarised in Table 2.1.

The propagation region of CRs in the Milky Way Galaxy is modelled as a two-dimensional spatial grid with cylindrical symmetry. The basic coordinates of the model are (R, z, p), where R is the Galactocentric radius, z the distance from the Galactic plane, and p the total particle momentum. The general transport equation for a particular species is written in the form [53]

$$\begin{aligned} \frac{\partial \psi}{\partial t} &= Q + \vec{\nabla} \cdot \left(D_{xx} \vec{\nabla} \psi - \vec{V} \psi \right) + \frac{\partial}{\partial p} p^2 D_{pp} \frac{\partial}{\partial p} \frac{1}{p^2} \psi + \\ &- \frac{\partial}{\partial p} \left[\dot{p} \, \psi - \frac{p}{3} \left(\vec{\nabla} \cdot \vec{V} \right) \psi \right] - \frac{1}{\tau_f} \psi - \frac{1}{\tau_r} \psi, \end{aligned} \tag{2.2}$$

where $\psi = \psi(\vec{r}, p, t)$ is the CR density per unit of total particle momentum p at position

Parameter	Value	Description
R_h	20 kpc	Radial boundary of the CR propagation region
z_h	5 kpc	Vertical boundary of the CR propagation region
v_A	36 km s^{-1}	Alfvén velocity
D_0	5.75×10^{28} cm^2 s^{-1}	Diffusion coefficient at reference rigidity
ρ_0	4×10^3 MV	Reference rigidity for diffusion coefficient

Table 2.2: Main input parameters of the diffusive re-acceleration model used in this work. The propagation parameters of the model are tuned to agree with ACE observations.

$\vec{r}$, $Q = Q(\vec{r}, p, t)$ is the source term, $\dot{p}$ is the momentum loss rate, τ_f is the time scale for fragmentation, and τ_r is the time scale for the radioactive decay. The propagation region is radially and vertically bounded by $R = R_h$ and $z = \pm z_h$, respectively. Beyond the boundaries free particle escape is assumed, i.e. $\psi(R_h, z, p) = \psi(R, \pm z_h, p) = 0$. R_h has been chosen to be 20 kpc while z_h, the CR halo height, 5 kpc. The choice of $z_h = 5$ kpc is a reasonable compromise, within the context of the diffusive re-acceleration model, between the lower limit of 4 kpc and the higher limit of 6 kpc estimated with the more recent cross-sections and observations from different experiments [54].

Diffusion re-acceleration models do not account for the convective/advective CR transport which is due to the existence of Galactic winds. Thus, the convection velocity $\vec{V}$ in Equation 2.2 can be neglected. On the other hand, these models describe the stochastic re-acceleration of CRs scattering on randomly moving magneto-hydrodynamic (MHD) waves in the interstellar magnetic field. The re-acceleration, so called to distinguish it from the primary acceleration process that occurs in the CR sources, is described as diffusion in momentum space by the coefficient D_{pp} in Equation 2.2. This coefficient is related to the spatial diffusion coefficient D_{xx} by

$$D_{pp} = \frac{p^2 v_A^2}{9\, D_{xx}}, \tag{2.3}$$

where v_A is the propagation velocity of Alfvén waves, the small scale turbulences of the interstellar magnetic field. If $v_A = 0$, re-acceleration does not take place. The stochastic re-acceleration provides a natural mechanism for reproducing the rigidity dependence of the boron-to-carbon (B/C) ratio data. This is achieved taking the Alfvén velocity $v_A \sim 30$ km s^{-1}, which is similar to its actual value in the ISM, and assuming a single power law for D_{xx},

$$D_{xx} = \frac{v}{c}\, D_0 \left(\frac{\rho}{\rho_0}\right)^{\delta}, \tag{2.4}$$

with $\delta = 1/3$ for all particle rigidities. This value of δ corresponds to MHD turbulence with a Kolmogorov spectrum. The propagation parameters have been tuned to agree with the

B/C ratio measured by the Advanced Composition Explorer (ACE) [55], and their values are summarised in Table 2.2.

2.3 Interstellar medium and radiation field

The transport equation 2.2 requires the knowledge of the interstellar environment, important for the production of secondary CR species and for energy losses. As described in Chapter 1, the main components of the ISM are the three gas phases of hydrogen: atomic (HI), molecular (H_2), and ionised (HII). The GALPROP code uses a 2D analytical model for the distribution of each of these gas phases, whose estimates come from the work of different authors. For the HI phase, the radial distribution is taken from Gordon & Burton (1976), while the vertical distribution is from Dickey & Lockman (1990) for a Galactic radius $0 \leqslant R \leqslant 8$ kpc, and from Cox et al. (1986) for $R \geqslant 10$ kpc, with linear interpolation between the two ranges. The molecular component, traced by the carbon monoxide CO (see Section 2.3.3), uses the gas distribution from Bronfman et al. (1988) for $1.5 \leqslant R \leqslant 10$ kpc, and that from Wouterloot et al. (1990) for $R \geqslant 10$ kpc. The ionised component HII is calculated using a cylindrically-symmetric model by Cordes et al. (1991). A helium component is also considered in the model. This component is used for fragmentation, secondary production, energy loss, and γ-ray production. The gas ratio of helium to hydrogen is taken as He/H = 0.11, a value widely used [51].

The CR density distribution in the Galaxy is found by solving the propagation equation. Once the equation is solved, GALPROP derives the γ-ray emissivities associated with the different components of the ISM.

While a fine structure is not crucial for propagation, the knowledge of the geometry of the Galaxy along with the small-scale hydrogen structures contained therein assumes a key role for estimating the emissivities and hence modelling the DGE. The latter is in fact highly structured with strong gradients which mostly reflect the spatial distribution of the ISM.

The information on the interstellar hydrogen can be provided by radio surveys, as the different gas components are traced by their emission line at this band. The evaluation of the emissivities can then be derived from the knowledge of the gas column densities for each of the gas phases. However, recent works have shown that up to 30% of the HI column density along a line of sight might be hidden by the HI self-absorption (HISA) against diffuse background emission. Thus, to correctly estimate the HI column density in the Galaxy, a method to search and extract HISA from survey observations is necessary. In this regard a fundamental work has been done by Gibson et al. [56] (hereafter Gibson) to develop such a method.

One of the goals of the work presented here is to exploit the Gibson's method and derive

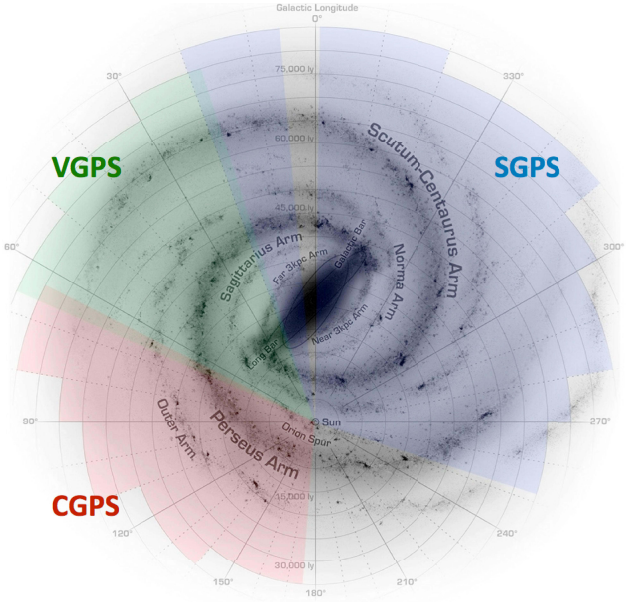

Figure 2.1: Top-view of the Milky Way Galaxy. The coloured-shaded regions indicate the sky coverage of the three wide-area, high-resolution radio surveys: the Canadian Galactic Plane survey (CGPS), the Southern Galactic Plane survey (SGPS), and the VLA Galactic Plane Survey (VGPS).

a more realistic estimate of the HI column density in the Galactic plane, accounting for the HISA contribution. A description of this procedure is discussed in Section 2.3.2. The next sections will focus on the derivation of the column density of the interstellar gas, necessary to estimate the γ-ray emissivities.

2.3.1 Atomic hydrogen

The derivation of HI column densities $N_{\rm HI}$ within the Galactic plane is made with data from three large-scale, high-resolution radio surveys: the Canadian Galactic Plane Survey (CGPS) [57], the Southern Galactic Plane Survey (SGPS) [58], and the VLA Galactic Plane Survey (VGPS) [59]. These three surveys are members of the International Galactic Plane Survey consortium. The IGPS provides high-quality data for over 90% of the Galactic disk with an unprecedented angular resolution. Figure 2.1 shows the longitudinal coverage of the three surveys. Off the Galactic plane, i.e. $|b| > 5^\circ$, the $N_{\rm HI}$ is derived using data from the all-sky survey Leiden/Argentine/Bonn (LAB) [7], which, however, has a more coarse resolution with respect to the other three surveys. Table 2.3 summarises the main characteristics of all the aforementioned surveys.

Atomic hydrogen observations are presented as 3D data, or data cube, containing observed brightness temperature T_b as a function of both spatial coordinates (longitude and latitude) and velocity (radial velocity of the gas) as a third dimension. The column density

Survey	Frequency (Component)	Sky coverage	Angular resolution
CGPS	1420 MHz (atomic)	$74.2^\circ \leqslant \ell \leqslant 147.3^\circ$, $-3.6^\circ \leqslant b \leqslant 5.6^\circ$	$\sim 1'$
	115 GHz (molecular)	$102.5^\circ \leqslant \ell \leqslant 141.5^\circ$, $-3^\circ \leqslant b \leqslant 5.4^\circ$	$\sim 1'$
SGPS I	1420 MHz (atomic)	$253^\circ \leqslant \ell \leqslant 358^\circ$, $\lvert b\rvert \leqslant 1.5^\circ$	$2.2'$
SGPS II	1420 MHz (atomic)	$5^\circ \leqslant \ell \leqslant 20^\circ$, $\lvert b\rvert \leqslant 1.5^\circ$	$\sim 3.3'$
VGPS	1420 MHz (atomic)	$18^\circ \leqslant \ell \leqslant 67^\circ$, $\lvert b\rvert \leqslant 1.3^\circ$, $\lvert b\rvert \leqslant 2.3^\circ$	$1'$
LAB	1420 MHz (atomic)	all-sky	$\sim 36'$

Table 2.3: Main features of the three high-resolution Galactic plane surveys and the all-sky survey. The molecular component of the ISM is observed by the CGPS through ^{12}CO line emission at 2.6 mm.

is derived in Galactocentric rings using a deconvolution technique described in Section 2.4.

Since the 21 cm HI line is not optically thin in all regions, and the data do not provide measurements of the opacity τ, a first-order opacity correction has been applied by assuming a uniform spin temperature T_s. The opacity-corrected $N_{\rm HI}$ can thus be derived as

$$N_{HI}(v, T_s) = -\log\left(1 - \frac{T_b}{T_s - T_{bg}}\right) T_s\, C\, \Delta v, \tag{2.5}$$

where $T_{bg} = 2.7$ K is the brightness temperature of the microwave background, $C = 1.83 \times 10^{18}$ cm^{-2} is a constant depending on the line profile shape, and Δv is the full line width at half maximum amplitude (FWHM). This correction has been often adopted in many large-scale emission surveys using values of T_s in the range 120–150 K. In this work a T_s value of 125 K is used for two main reasons. First, to be consistent with the analytical model of the HI distribution used in the GALPROP code, which used $T_s = 125$ K. Second, to directly compare the results with existing $N_{\rm HI}$ maps provided within GALPROP and derived assuming this value.

The main source of uncertainty when deriving $N_{\rm HI}$ is, however, the assumed T_s itself. Relatively small changes in its value may in fact reflect substantial changes in the derived value of $N_{\rm HI}$. Figure 2.2 shows this effect along a certain line of sight. Varying T_s in the range 100–200 K induces, in this particular case, a change in the $N_{\rm HI}$ value of $\sim 22\%$. It can be shown that this effect has the same order of magnitude for any given line of sight in the Galactic plane.

One of the techniques to determine T_s consists of observing the gas in both absorption and emission. This however would require a considerable number of bright radio sources and their absence together with the lack of deep observations prevents us from obtaining a full sky coverage of T_s. Furthermore, observations show T_s to vary as a function of both velocity and location, then there is no an obvious pattern for estimating T_s. But, in the absence

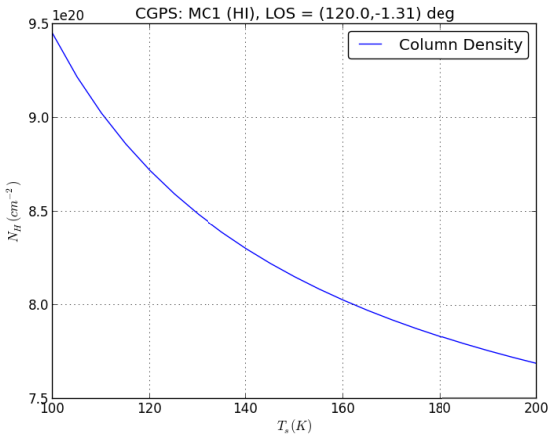

Figure 2.2: Column density $N_{\rm HI}$ as a function of spin temperature T_s. $N_{\rm HI}$ is derived with data from the Canadian Galactic Plane Survey (CGPS), along a line of sight with Galactic coordinates $\ell = 120^\circ$ and $b = -1.31^\circ$. The variation of $N_{\rm HI}$ of $\sim 22\%$, in the range 100-200 K for T_s, shows how closely related the derived $N_{\rm HI}$ and the assumed value of T_s are.

of evidence of mechanisms heating the gas, assuming a constant T_s is actually a physically reasonable starting point to analyse the observations.

2.3.2 HI self absorption

The LAB survey is by far the most utilised observatory for studying the DGE. Its popularity is mostly due to the fact that it is the only uniform complete survey covering the entire Milky Way Galaxy in the HI line emission. However, due to its relatively low angular resolution, if compared to the small-scale structure of the ISM, it is not adequate to identify absorption features smaller than half a degree. Therefore, to derive the HI column density corrected by the self-absorption, observations from the three high-resolution surveys introduced in Section 2.3.1 are used. Furthermore, to search and extract HISA features from survey data, the algorithms developed by Gibson are used.

The idea behind the Gibson's algorithms, based on a variant of the CLEAN algorithm (Högbom, 1974), is to remove large-scale spectral and spatial emission structures from HI data iteratively and flag the small-scale negative residuals as self-absorption features.

Following the Gibson's procedure the analysis pipeline is separated into three parts for computational efficiency. The first two parts are dedicated to the spectral and spatial search, the last part to the amplitude estimation. Details on the analysis can be found in his paper. Here it is only reported the calculation of the column density.

To extract estimates of column density for HISA cloud it is necessary to solve numerically a system of two equations. The first one is the optical depth solution to the radiative transfer equation 1.14 derived in Section 1.2.2,

$$\tau = -\ln\left(1 - \frac{T_{\rm on} - T_{\rm off}}{T_s - T_c - p\,T_{\rm off}}\right) \tag{2.6}$$

where $T_{\rm on}$ is the observed brightness temperature along the line of sight toward the HISA

cloud and $T_{\rm off}$ away from it, T_c is the brightness temperature of the continuum background, and p is the fraction of HI emission originating behind the HISA cloud.

The second equation comes from assumptions about the nature of the gas and its sight line distribution. The first assumption is that the HISA feature must contain only one velocity component and must be isothermal along the line of sight. These conditions enable the relation for the optical depth defined in Equation 1.10. The second assumption is that its volume density $n_{\rm HISA}$ and kinetic temperature T_k must be related via an ideal gas law

$$P = n_{\rm tot} k\, T_k \simeq \frac{n_{\rm HISA} k\, T_s}{f_n}, \tag{2.7}$$

where $T_s \simeq T_k$, P/k is the gas thermal pressure, $n_{\rm tot}$ is the total gas density, and $f_n \equiv n_{\rm HISA}/n_{\rm tot}$ is the fraction of particle density contributed by the HISA gas.

Combining Equation 1.10 and Equation 2.7 yields

$$T_s = \left(\frac{\langle P \rangle\, f_n\, \Delta s}{C\, k\, \tau_0\, \Delta v} \right)^{1/2}, \tag{2.8}$$

where the gas thermal pressure is averaged over the feature's sight line dimension Δs, τ_0 is the opacity at line centre, and C and Δv are defined as in Section 2.3.1.

Thus, solving numerically Equation 2.6 in combination with Equation 2.8 and using the resulting values for τ and T_s in Equation 1.10, it allows to derive the HISA column density

$$N_{\rm HISA} = \tau\, C\, \Delta v\, T_s, \tag{2.9}$$

for those sky regions where continuum emission observations are available.

2.3.3 Molecular hydrogen

As described in Section 1.2.2, the molecular component of hydrogen cannot be directly observed in emission due to the absence of a dipole moment. Therefore, as a tracer of H_2 it is commonly used the 2.6 mm line of the ^{12}CO molecular transition $J = 1 \rightarrow 0$, which is one of the most abundant polar molecules in the ISM. By mean of its velocity-integrated line intensity,

$$W_{\rm CO} = \int T_{\rm CO}(J = 1 \rightarrow 0)\, dv \tag{2.10}$$

the H_2 column density $N_{\rm H_2}$ can be derived using a conversion factor $X_{\rm CO}$ and the relation

$$N_{\rm H_2} = X_{\rm CO} \times W_{\rm CO} \tag{2.11}$$

The W_{CO} is derived from observations of the CGPS in the region of the Galactic plane comprising $102.5^{\circ} \leqslant \ell \leqslant 141.5^{\circ}$ and $-3^{\circ} \leqslant b \leqslant 5.4^{\circ}$, and from those of the composite survey of Dame [8] in the rest of the Galaxy. Following the work by Ref. [30], the X_{CO} factor is assumed to vary with Galactocentric radius. Its value is used by GALPROP in both CR propagation and γ-ray emissivities derivation.

Furthermore, before deriving W_{CO}, the CO data have been filtered with the moment-masking technique [8] in order to reduce the noise while keeping the resolution of the original data.

2.3.4 Ionised hydrogen

This gas component is mostly concentrated in the vicinity of young O and B stars, since the ultraviolet radiation originating from these very hot stars, with surface temperatures higher than 10^4 K, ionises the surrounding gas. However, since this work focuses on the Galactic plane, where most of the supernova remnants are, and the ionised component of hydrogen gives a significant contribution to the DGE only at high latitude, its column density contribution is not taken into account for the derivation of γ-ray emissivities.

2.3.5 Radiation fields

As discussed in Section 1.2.4, the leptonic component of CRs interacts with the ISRF through inverse Compton scattering. This mechanism is important for both propagation (energy losses) and γ-ray emission of CR electrons. The radiation field is mainly due to photons emitted by stars and then scattered or absorbed and re-emitted by dust. Therefore, the modelling of ISRF requires the knowledge of detailed Galactic stellar and dust distributions along with a treatment of absorption and scattering of photons in order to calculate the emissivities. In this work a model based on COBE/DIRBE survey is used as stellar distribution [60]. The dust in the ISM is based on the grain model abundance and size distribution of Weingartner & Draine (2001).

2.4 Deconvolution process

To transform the spectral measurements into maps of column densities for a range of Galactocentric rings a deconvolution technique, along with the relations found in the previous sections, is used. Such a technique is based on the method developed by Pohl et al. [61] (hereafter Pohl) and applied to the HI unabsorbed component (i.e., the one corrected for self-absorption), the HI absorber (i.e., the cold HI responsible for self-absorption), and the CO component.

For a given direction, the observed spectral line shows a broadened profile which extends over a range of radial velocities. The spectral broadening is a result of several effects, the main of which are the intrinsic instrumental resolution, the Doppler broadening due to the thermal motion of the gas particles, turbulence within the cloud, and multiple clouds along the same line of sight, each with a different radial velocity relative to the observer. A deconvolution process is hence necessary to disentangle the different components of the broadened profile and to apply to them a one-to-one relationship between their radial velocity, also called velocity with respect to the local standard of rest v_{LSR}, and the Galactocentric distance R. Before describing the deconvolution method, a way to link v_{LSR} to R is discussed.

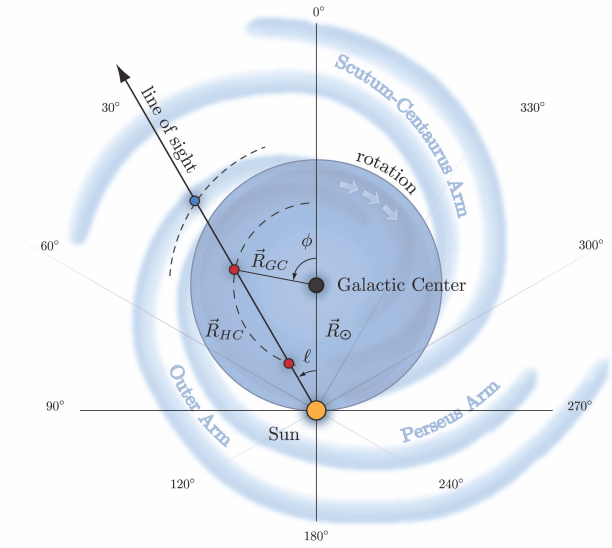

Figure 2.3: Top view of the Milky Way Galaxy in both Heliocentric (HC) and Galactocentric (GC) systems of reference. The circular shaded region is the inner Galaxy delimited by the solar orbit. The radius of the Sun's orbit around the Galactic centre is indicated by $R_{\odot}$. Along the line of sight $(\ell,\, b) = (30°, 0°)$, a generic cloud lying within the solar orbit (first red point from the top) has GC coordinates given by Equation 2.12. In the HC system the same cloud with distance R_{GC} can be seen in two different positions (the two red points display the near-far ambiguity). Outside the solar orbit the ambiguity does not exist. A hypothetical cloud in the Outer Arm (blue point) has only one possible HC distance corresponding to R_{GC}.

2.4.1 Velocity to distance relation

An arbitrary cloud in the Galaxy has Galactocentric (GC) coordinates,

$$\vec{R}_{GC} = (R_{GC}\cos\phi,\, R_{GC}\sin\phi,\, z), \tag{2.12}$$

where R_{GC} is the radial distance from the Galactic centre, ϕ is the azimuthal angle, and z the height from the Galactic plane (see Figure 2.3). In these coordinates the Sun is located at $\vec{R}_{\odot} = (-R_{\odot},\, 0,\, z_{\odot})$, where values of $R_{\odot} = 8.5$ kpc and $z_{\odot} = 15$ pc are used throughout this work, as recommended by the International Astronomical Union (IAU). Observations, however, provide information in terms of heliocentric Galactic coordinates (HC). Thus, the position of the same cloud in terms of the new coordinates is

$$\vec{R}_{HC} = (R_{HC}\cos\ell,\, R_{HC}\sin\ell,\, z_{HC}), \tag{2.13}$$

Ring N	Min value (kpc)	Max value (kpc)	Ring N	Min value (kpc)	Max value (kpc)
1	0.	1.767249	6	9.5	11.5
2	1.767249	3.524893	7	11.5	13.5
3	3.524893	5.520308	8	13.5	15.5
4	5.520308	7.505054	9	15.5	50.0
5	7.505054	9.5			

Table 2.4: Boundaries of the 9 Galactocentric rings used in this analysis.

where $R_{HC} = (P \cos b)$ is the radial distance from the Sun, $z_{HC} = (P \sin b)$ is the height from the Galactic plane, and ℓ, b are the Galactic longitude and latitude of the line of sight. The heliocentric distance R_{HC} associated to (ℓ, b, v_{LSR}) is obtained by solving a second order equation, derived by geometrical considerations, whose solutions are

$$R_{HC} = R_\odot \cos \ell \pm \sqrt{R_{GC}^2 - R_\odot^2 \sin^2 \ell}. \tag{2.14}$$

For the outer Galaxy ($R_{GC} > R_\odot$) there is only one kinematically allowed distance, the positive solution. However, in the inner part of the Galaxy ($R_{GC} < R_\odot$) both kinematic distance solutions are allowed. This leads to a degeneracy, often called near-far ambiguity, which does not allow to uniquely determine the kinematic distance for a given radial velocity (except for tangent points $R_{GC} = R_\odot |\sin \ell|$ where the distance solutions coincide). Where this is the case, the Pohl's method provides a way to distribute the line signal between the different distance solutions using weights. This point will be discussed further hereinafter.

Under the assumption of purely circular gas motion with rotation curve $V(R_{GC})$, the radial velocity with respect to the Sun of a cloud with Galactocentric distance R_{GC}, viewed toward direction ℓ, b is

$$v_{LSR}(\ell, b) = \left[\frac{R_\odot}{R_{GC}} V(R_{GC}) - V_\odot \right] \sin \ell \cos b. \tag{2.15}$$

For a given line of sight (ℓ, b), and Galactic rotation curve $V(R_{GC})$, all variables in this equation are known. Thus, kinematic distances can be finally assigned to radial velocities. In this analysis all the kinematic distances are confined together in 9 possible Galactocentric rings. The boundaries of the rings are shown in Table 2.4, while the rotation curve used in this work is described below.

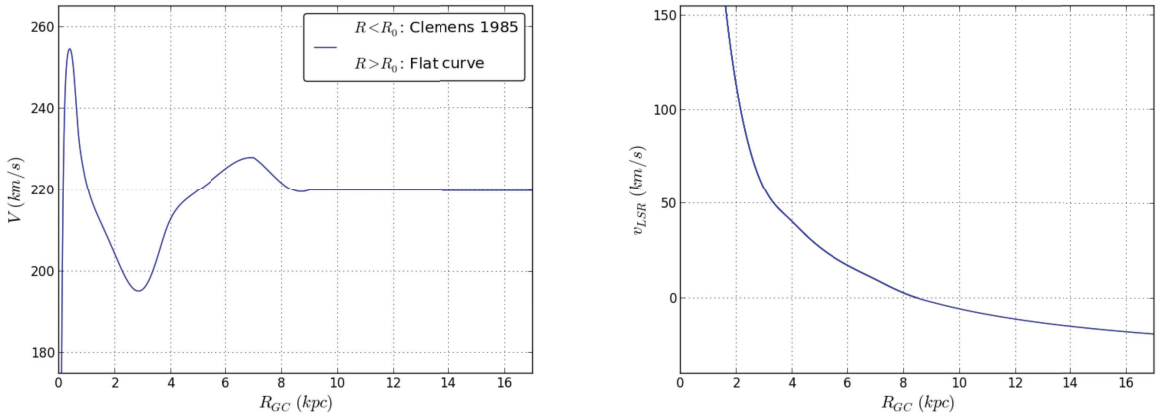

Figure 2.4: Left side: the Galactic rotation curve used in this work as a function of Galactocentric radius. For $R < R_\odot$ the curve is from Dan P. Clemens (1985); for $R > R_\odot$ a flat rotation curve is used. Right side: radial velocity curve as defined in Equation 2.15, for a line of sight in the Galactic plane with $\ell = 10°$.

2.4.2 Galactic rotation curve

Inside the solar circle ($R_{GC} < R_\odot$) the Galactic rotation curve from Clemens (1985) [62] is used. Such a composite curve is a result of a fit of data from the Massachusetts-Stony Brook Galactic plane CO survey. The data were fitted by a polynomial of the form,

$$V(R_{GC}) = \sum_{i=0}^{7} A_i. \tag{2.16}$$

Two sets of coefficients of the polynomial are provided in the Clemens's work, depending on the assumed value for $R_\odot$ and the rotation velocity of the Sun around the Galactic centre $V_\odot$. In this analysis coefficients corresponding to $R_\odot = 8.5$ kpc and $V_\odot = 220$ km s^{-1} are used. Outside the solar circle, where $R_{GC} > R_\odot$, a flat rotation curve with $V = V_\odot$ is also considered. In the transition region between the inner and the outer Galaxy a linear interpolation is used to match the two curves.

Figure 2.4 shows the composite rotation curve V used in this work and, as an example, the radial velocity curve v_{LSR} for $(\ell, b) = (10°, 0°)$, both curves as a function of Galactocentric distance. From the right side curve it can also be seen that the radial velocity at the position $R_\odot$ is 0. This reflects the way the local standard of rest is defined, i.e., the point which co-rotates with the Galaxy at the solar Galactocentric radius.

2.4.3 Iterative procedure

Once the rotation curve of the Galaxy is defined, the spectral measurements can be deconvolved. The deconvolution process is based on an iterative procedure in which, for every line of sight, the following steps are performed:

1. A smoothed version $S(k)$, where k is the channel index, of the observed spectrum $O(k)$ is used to improve the signal-to-noise ratio and hence to better determine peak values and relative velocities. $S(k)$ is the result of a convolution of $O(k)$ with a Gaussian whose sigma is equal to the gas velocity dispersion. In the case of the HISA spectrum, this step is unnecessary because the spectrum extends over a few noise-free channels.

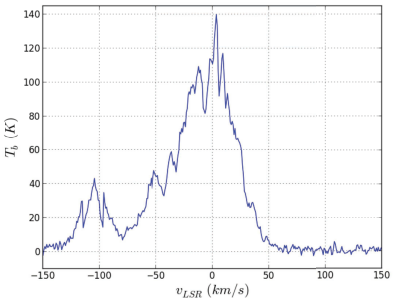

(a) Observed spectrum $O(k)$.

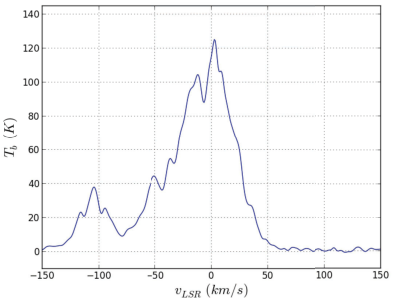

(b) Smoothed spectrum $S(k)$.

2. A residual spectrum $R(k)$ is defined by subtracting a Gaussian $G(k_0)$ with the amplitude A equals to 20% of the peak value, centred at the corresponding channel k_0 of the peak, and with a given velocity dispersion, from the observed spectrum $O(k)$. Taking 20% of the peak instead of the full peak line signal is a way to reduce artefacts introduced by the deconvolution itself.

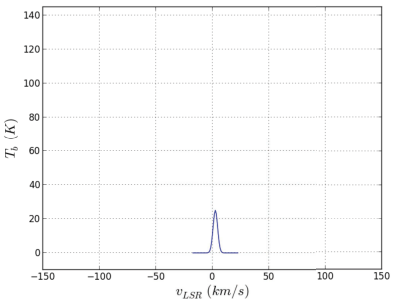

(a) Gaussian $G(k_0)$.

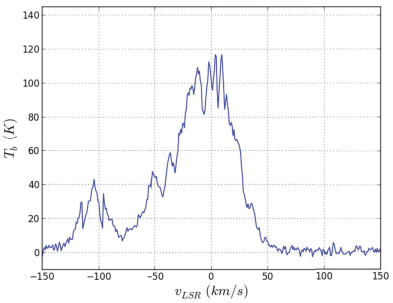

(b) $R(k) = O(k) - G(k_0)$.

3. The corresponding amplitude A, along with the width of $G(k_0)$, are used to calculate the HI column density through Equations 2.5, 2.9, and the CO velocity-integrated

intensity through Equation 2.10. The resulting quantities are hence assigned to Galactocentric rings, whose boundaries are defined in Table 2.4. The assignment is done by using Equation 2.15, with radial velocity $v_{LSR} = v[k_0]$, the radial velocity corresponding to the peak value of the line. Such a procedure requires further explanation that will be outlined below.

4. The iteration is repeated until the integral of the residual spectrum $R(k)$ is less than a preset value, corresponding to 0.5 K km s^{-1} for HI and CO, and 0.01 K km s^{-1} for HISA.

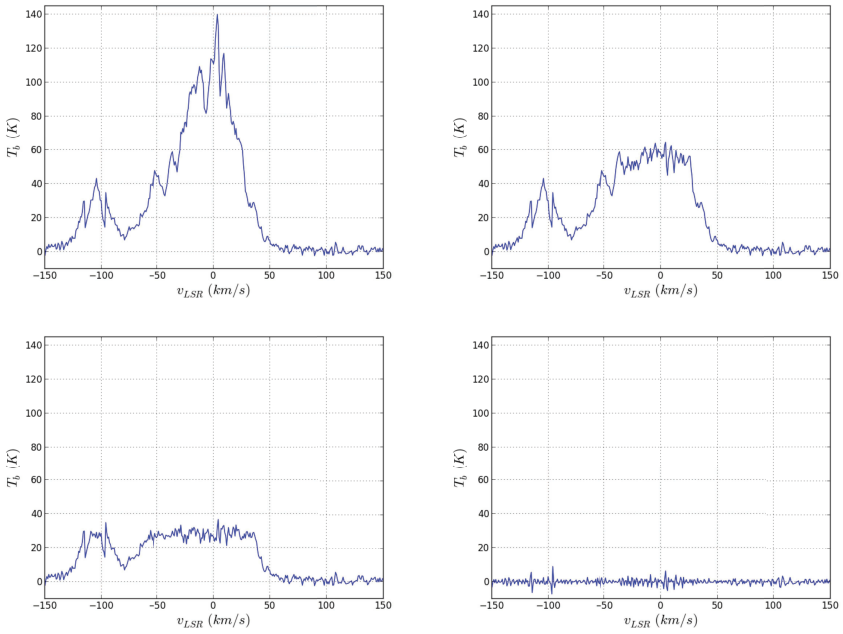

The above figure shows the evolution of the residual spectrum $R(k)$ after 25, 75, and about 1300 iterations.

2.4.4 Definition of weights

Figure 2.8 shows the velocity of the interstellar gas as a function of heliocentric distance, along the line of sight with coordinates $(\ell, b) = (0.5^\circ, 0^\circ)$. The narrow curve peaks at the Sun position around which it loses its monotonic behaviour. As a consequence, almost all radial velocities along this line of sight have two possible distance solutions. To account for this, the line emission is distributed between two distance bins of 50 pc length. Each bin receives part of the line emission according to certain weights defined as a product of three terms.

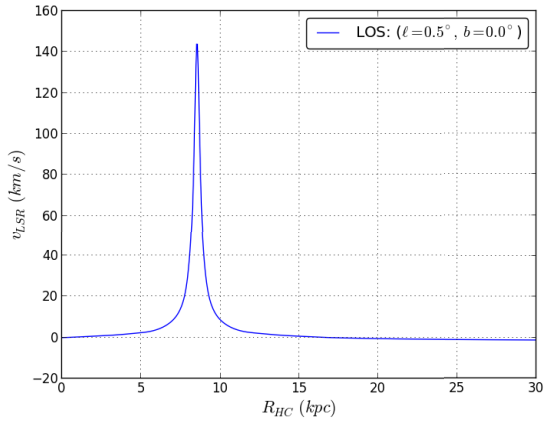

Figure 2.8: Radial velocity with respect to the local standard of rest as a function of heliocentric distance. The line of sight points 0.5° away from the Galactic centre and lies on the Galactic plane. It is worth noting that almost all velocities have two distance solutions.

The first term accounts for the vertical extension of the gas, assuming that this can be described by a Gaussian function of the form

$$w_z = \exp\left\{-\frac{1}{2}\left(\frac{z - z_0}{\sigma_z}\right)^2\right\} \tag{2.17}$$

whose scale height σ_z and mid-plane displacement z_0 are obtained from analytical approximations by Pohl. In this paper he uses various results reported in the literature (see the paper for references) to formulate the two following expressions,

$$\sigma_z = 60 - 50\left(\frac{R_{GC}}{R_\odot}\right) + 60\left(\frac{R_{GC}}{R_\odot}\right)^2$$

$$z_0 = ax\sin\phi + bx^2\left(1 - \cos 2\phi\right)$$

where a and b are two constants, ϕ is the azimuthal angle, and $x = (R_{GC} - 11 \text{ kpc})/6 \text{ kpc}$, with $R_{GC} \geqslant 11$ kpc. This last condition ensures that the mid-plane displacement coincides with the Galactic plane in the inner Galaxy, where the warp of the gas disk appears insignificant, and differs in the outer Galaxy where the warp cannot be neglected.

From Figure 2.9a it can be seen that the point whose height is closer to the mid plane receives more contribution from the line signal. In this specific case, the line of sight has coordinates $(\ell, b) = (30°, 0.5°)$, and points in a direction within the solar circle where a near-far ambiguity exists. The point equivalent to the near-distance solution has $z \sim 30$ pc, corresponding to a weight $w_z = 0.95$. The other point, coinciding with the far-distance solution, has a higher z (~ 100 pc) to which corresponds a smaller weight $w_z = 0.6$.

The second term of the product is added to avoid placing gas at unrealistic large distance.

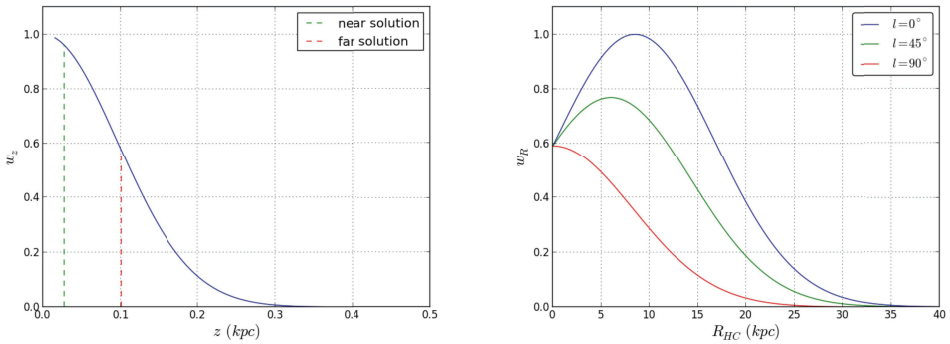

(a) $w_z(z)$ **(b)** $w_r(R_{HC})$

Figure 2.9: Left side: weight accounting for the vertical extension of the interstellar gas. The more the gas is close to the mid-plane displacement the more weight it receives. Right side: weight accounting for the Galactocentric distance.

Such a term is defined by a Gaussian function of the form

$$w_R = \exp\left\{-\frac{1}{2}\left(\frac{R_{GC}}{\sigma_R}\right)^2\right\}, \tag{2.18}$$

where $\sigma_R = 8.3$ kpc is the radial scale in Galactocentric radius. In Figure 2.9b is shown w_R as a function of the heliocentric distance, for three lines of sight corresponding to $\ell = 0°$, $45°$, $90°$ and $b = 0°$. The distance solution whose value is closer to the tangent point, corresponding to the peak of the curve, receives more contribution from the line signal. In the case of near-far ambiguity, w_R cannot disentangle the two solutions that hence receive an equal amount of signal from it.

Finally, the third term of the product comes from the Jacobian used to transform differential in velocity into differential in heliocentric distance, defined as

$$J = \left|\frac{dv_{LSR}}{dR_{HC}}\right| = \frac{\delta v_{LSR}}{\Delta R_{HC}} \qquad \Rightarrow \qquad w_J = \frac{\delta v_{LSR}}{n\,\delta R_{HC}} \tag{2.19}$$

where δv_{LSR} is the velocity interval, equals to the velocity pixel size of survey data, and ΔR_{HC} is the associated distance interval. The size of the distance interval can be defined in terms of bins δR_{HC} whose size is 50 pc. If $\Delta R_{HC} > \delta R_{HC}$ then the line signal is equally distributed over n bins. In the opposite case, the line signal is entirely assigned to one bin.

In summary, part of the line signal is assigned to the i^{th} distance bin according to the normalised weight defined as follows

$$\tilde{w}_i = \frac{\Pi_j w_{ij}}{\sum_k \Pi_j w_{kj}} \tag{2.20}$$

where the index $j = z, R, J$ accounts for the different weights and the sum over k is the normalisation factor.

2.4.5 Forbidden velocities

Due to non-circular motion of the gas in the Galaxy, some cloud can have forbidden velocity. This may happen when the angular velocity

$$\Omega \equiv \frac{V(R_{GC})}{R_{GC}} = \Omega_{\odot} + \frac{v_{LSR}}{R_{\odot} \sin \ell \cos b} \tag{2.21}$$

that is always positive, for some value of v_{LSR} becomes negative. In this case the gas is assigned to the local ring, the one that spans $R_{\odot}$.

A different situation of forbidden velocity is when the gas velocity is greater than the terminal velocity v_t, defined as the radial velocity at the tangent point $R_{\odot} |\sin \ell|$. If the offset $|v_{LSR} - v_t|$ is more than 10 km s^{-1} the line signal is assigned to the corresponding tangent point.

2.5 Results

Once all observations have been converted in column density or integrated emission line and assigned to Galactocentric rings, the resulting gas maps are input to GALPROP so that they can be used to define the spatial distribution of matter in the Galaxy. Such a distribution is hence used to calculate the γ-ray emissivities from which the intensity of the DGE is derived.

Before this last step, all high-resolution gas maps are down sampled to an angular resolution of 0.125° and combined with the low-resolution all-sky maps. The resulting gas map is therefore a composite all-sky map with a finer resolution in the Galactic plane. This degradation of angular resolution is reflected in the resulting DGE template but does not affect the analysis of supernova remnants because the Fermi-LAT point-spread function below 5–10 GeV, where most of the photons are detected, is larger than 0.25°.

Figure 2.11 shows the deconvolved high-resolution gas maps of a region of the Galactic plane covered by the CGPS (upper maps) in comparison with the low-resolution maps from the LAB and Dame surveys (lower maps). The map at the top in Figure 2.11b is the hydrogen column density derived by the column density of the unabsorbed HI gas and that of the colder HI absorber.

The DGE model is output in the form of three templates representing the three main components of the emission: inverse Compton, bremsstrahlung, and π^0-decay. The IC component is treated using the formalism for an isotropic or anisotropic radiation field developed

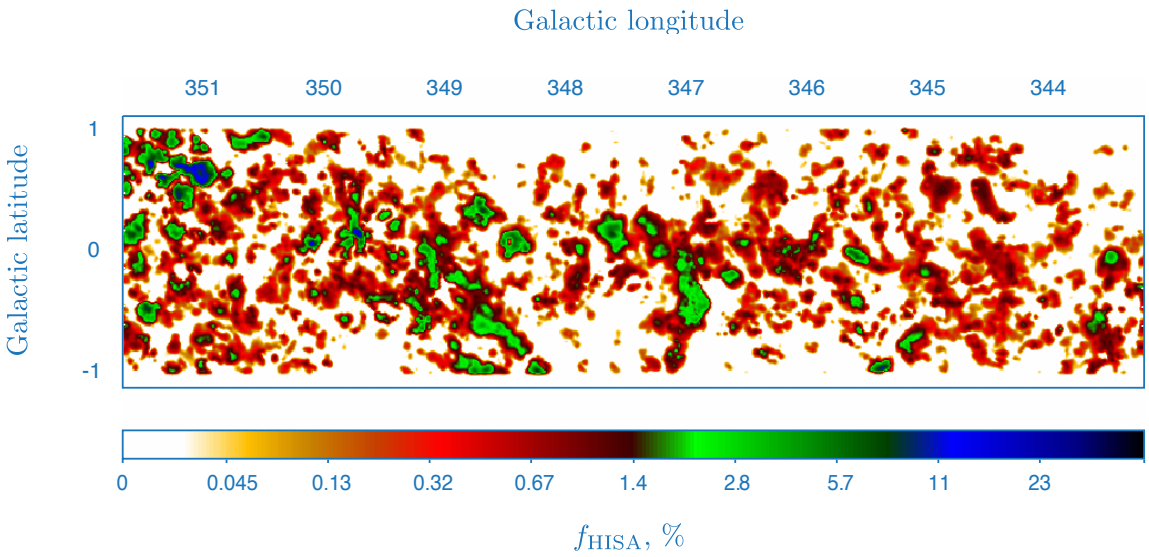

Figure 2.10: Fraction of HISA along the line of sight relative to the total amount of HI gas. The fraction is defined as $f_{\mathrm{HISA}} = n_{\mathrm{HISA}}/n_{tot}$ and is given as percentage. For many lines of sight the HISA contributes for more than 5% to the total gas with peaks $> 30\%$. The sky region shown here is the one used to study the supernova remnant RX J1713.7–3946 (see next chapter).

by Moskalenko & Strong [63] with the full spatial and angular distribution of the ISRF as described in Section 2.3.5. The γ-ray intensities of π^0-decay and bremsstrahlung are computed from the emissivities as a function of (R, z, E_γ), using a formalism by Dermer [64] and by Koch and Motz [65] respectively.

In this chapter a novel approach in modelling the DGE has been provided. The key point of this approach is the deconvolution technique discussed in the previous sections. Furthermore, an unprecedented element consists in accounting for the correction for HI self-absorption and the inclusion of the cold HI absorber as a component of the ISM. Despite the HISA may not be important for studies on large-scale structures, its contribution is of particular relevance in revealing morphological details of cold atomic hydrogen clouds for several lines of sight where it may reach more than 30% of the total HI gas density, as shown in Figure 2.10. Thus, neglecting this phenomenon may lead to underestimate the ISM density, especially in the Galactic plane where most of the cold gas lies and where this work is focused on.

The DGE model developed with the method discussed in this chapter is used to correct for HISA the standard Fermi-LAT background map. The corrected-background map is then used for the analysis of a particular extended supernova remnant: RX J1713.7–3946. A description of this analysis is given in the next chapter.

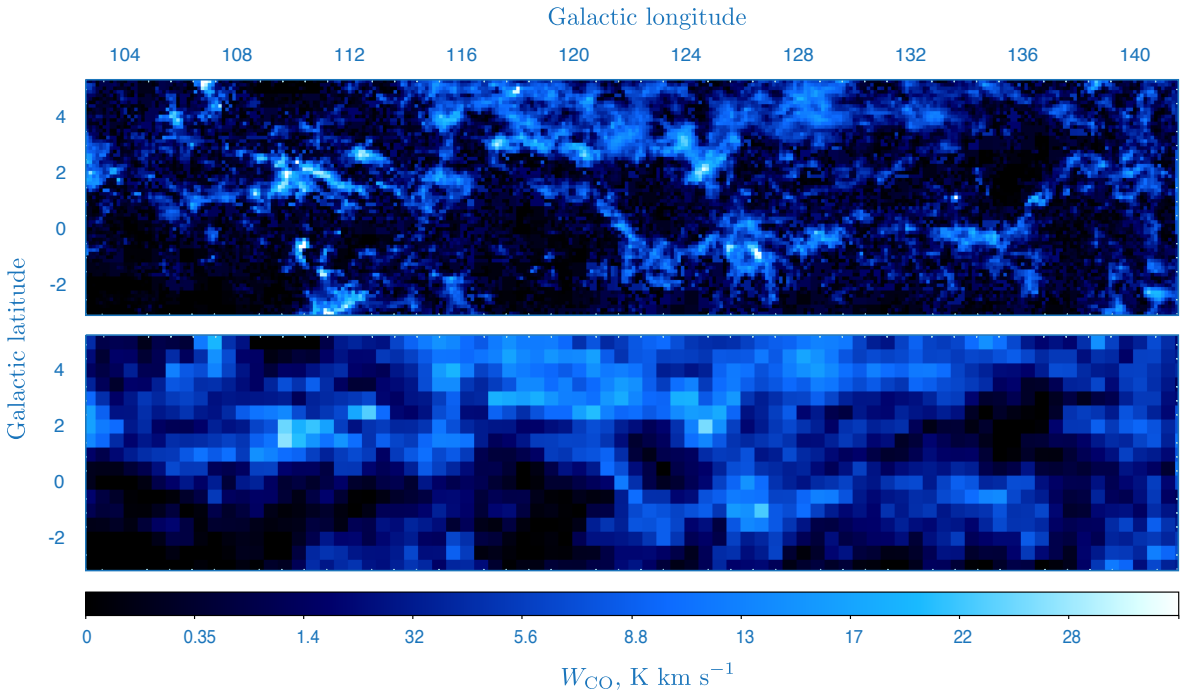

(a) Integrated line intensity of the molecular carbon monoxide W_{CO}.

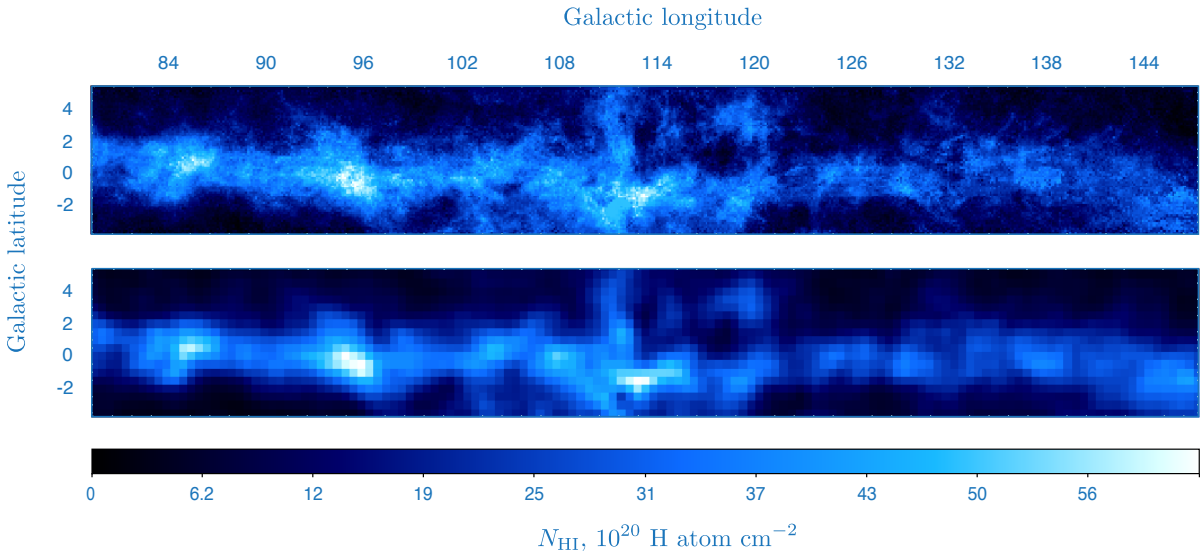

(b) Column density of the atomic hydrogen N_{HI}.

Figure 2.11: (a) W_{CO} derived with the deconvolution technique described in the text from observations of CGPS (top) in comparison to the W_{CO} derived by Dame (bottom). Both maps are shown within a distance bin of 7.5–9.5 kpc, corresponding to the 5^{th} ring. (b) N_{HI} as a combination of unabsorbed HI gas and the colder HI absorber derived with the deconvolution technique from CGPS observations (top). This is compared to the N_{HI} derived with LAB observations (bottom).

3

Observation of SNR RX J1713.7–3946

In this chapter the analysis of the γ-ray emission from the SNR RX J1713.7–3946 is described. The analysis is performed using the 2nd Fermi-LAT catalog and the diffuse Galactic γ-ray emission background derived in the previous chapter. A discussion of the observed spatial and spectral features jointly with X-ray and TeV γ-ray observations and the possible origin of the γ-ray emission is presented.

3.1 Introduction

RX J1713.7–3946, also known as G347.3–0.5, is a young ($t_{\rm SNR} \simeq 1600$ yr) shell-type SNR located in the Galactic plane within the tail of the constellation Scorpius. This SNR was discovered in 1996 during the ROSAT X-rays all-sky survey [66]. Its shape is slightly elliptical with the maximum extent of $70'$ and it exhibits bright X-ray emission predominantly from the western edge of the shell. The assumed distance $d_{\rm SNR} \simeq 1$ kpc implies a shell radius $r_{\rm SNR} \simeq 8.7$ pc. The remnant contains an X-ray point-like source whose properties are similar to central compact objects in other SNRs, thus typing RX J1713.7–3946 as a core-collapse supernova.

Since its discovery RX J1713.7–3946 has been observed in a wide energy range. In 1997, observations with the Japanese ASCA satellite [67] (Figure 3.1a) showed a featureless X-ray spectrum in the northwest shell of the remnant indicating a clear non-thermal emission. Two years later, new ASCA observations [68], confirming the previous results, obtained evidence of the absence of line emission everywhere in the remnant and showed that all parts of the remnant had spectra described by power-law with comparable indices from ~ 2.2 to 2.4. At small spatial scale more recent studies of the remnant conducted with Chandra [69] and XMM-Newton [70] satellites clearly showed a spatial variation of the photon index ranging

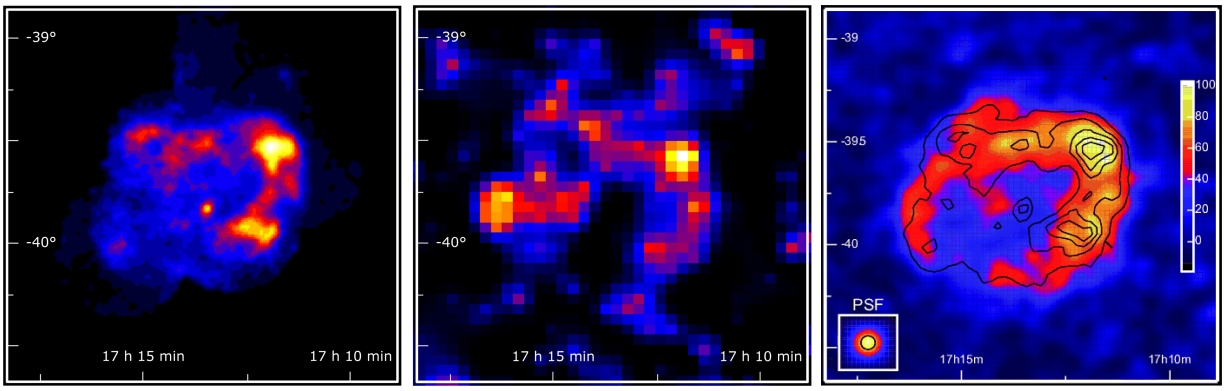

(a) ASCA (keV scale). **(b)** Fermi (MeV–GeV scale). **(c)** H.E.S.S. (GeV–TeV scale).

Figure 3.1: Field of view of the region around RX J1713.7–3946 ($2^\circ \times 2^\circ$). The remnant has been detected in a wide energy band by different observatories. Three of the most significance detections are shown here. (a) ASCA count map in the energy range 1–3 keV. (b) Map of the test statistic obtained by the Fermi collaboration using events above 500 MeV. (c) TeV count map obtained by the H.E.S.S. experiment with an energy threshold of 800 GeV.

from 1.8 to 2.6.

At higher energies the nature of the emission from RX J1713.7–3946 remains still controversial. Two competing radiation processes complicate its interpretation. The leptonic scenario where the γ-rays are produced by electrons via inverse Compton scattering, and the hadronic scenario where the γ-rays are due to π^0-decay from proton-proton interactions. Both scenarios can produce similar fluxes in the GeV-TeV energy range.

In 1998, the CANGAROO atmospheric Cherenkov telescope detected a TeV-scale emission in the northwest of the SNR. Such emission was interpreted as due to inverse Compton from accelerated electrons [71]. The reason being that the low matter densities in the ambient medium made the interpretation in terms of π^0-decay process unlikely.

In 1999, EGRET, one of four instruments outfitted on NASA's Compton Gamma Ray Observatory satellite, detected GeV γ-rays in the northeast of the SNR [72]. The emission was interpreted in terms of hadronic scenario as originating from CR nuclei accelerated at the shock front of RX J1713.7–3946 and interacting with the very massive ($\sim 3 \times 10^5\, M_\odot$) and dense (500 nucleons cm^{-3}) molecular cloud associated to the unidentified EGRET source 3EG J1714-3857 [73].

In 2000, a second CANGAROO observation of RX J1713.7–3946 led to a different conclusion. The measured spectrum, between 400 GeV and 8 TeV, showed an index of 2.8 consistent with the hadronic scenario and no other mechanism [74]. Nevertheless, this interpretation was found to be in conflict with the EGRET observations [75].

In 2004, another atmospheric Cherenkov experiment, the H.E.S.S. telescope array, confirmed the detection of RX J1713.7–3946 at the TeV-scale [76] and showed the similarity

between the X-ray and TeV-band emission (see Figure 3.1c). The collaboration discussed the emission for both leptonic and hadronic scenarios. No decisive conclusion was drawn for the particle population responsible for the emission, although the hadronic scenario was favoured.

In 2011, the Large Area Telescope (LAT) [77], the principal instrument on board NASA's Fermi γ-ray satellite, measured an extended GeV γ-ray emission coincident with the position of RX J1713.7–3946 [78]. Figure 3.1b shows the significance map of the emission region in terms of test statistic[1]. The spectral analysis found a very hard spectral photon index ($\gamma = 1.5$) which was well in agreement with a leptonic scenario. Nonetheless this conclusion did not exclude the possibility that protons are accelerated in this SNR.

The scenario which emerges from all these observations clearly shows that at present it is not possible to distinguish unambiguously the contributions of leptonic and hadronic interactions to different bands of γ-ray spectrum. Thus, the possibility to analyse a larger data set from Fermi-LAT in the region of RX J1713.7–3946 along with a new DGE background model derived with the method described in the previous chapter (hereinafter the corrected DGE background), provides an exciting opportunity to further investigate the properties of the emission associated with this controversial SNR. In this regard, in the next sections a new morphological and spectral study of RX J1713.7–3946 is presented.

3.2 Detector performance and data reduction

The young shell-type supernova remnant RX J1713.7–3946 is analysed using observations from Fermi-LAT. A brief description of the instrument together with the set of data cuts which are processed before the start of the analysis is outlined below.

3.2.1 The LAT instrument

The LAT, shown in Figure 3.2, is a pair-conversion telescope designed to detect photons from $\sim$ 20 MeV to 300 GeV. The core of the LAT is a 4×4 grid which accommodates 16 identical modules. Each module consists of a tracker and a calorimeter. The tracker is made up of 18 layers of silicon microstrip detectors interleaved with tungsten foils to promote the conversion of γ-rays into electron–positron pairs. A segmented CsI calorimeter located at the bottom of the tower is used to determine the γ-ray energy. The whole system is surrounded by a scintillator shield to discriminate the charged CR background.

Photon direction is primarily reconstructed by following the trajectory of electron-positron pairs through the tracker layers back to the photon interaction vertex. Detector geometry

[1]The test statistic (TS) is defined in Equation 3.6.

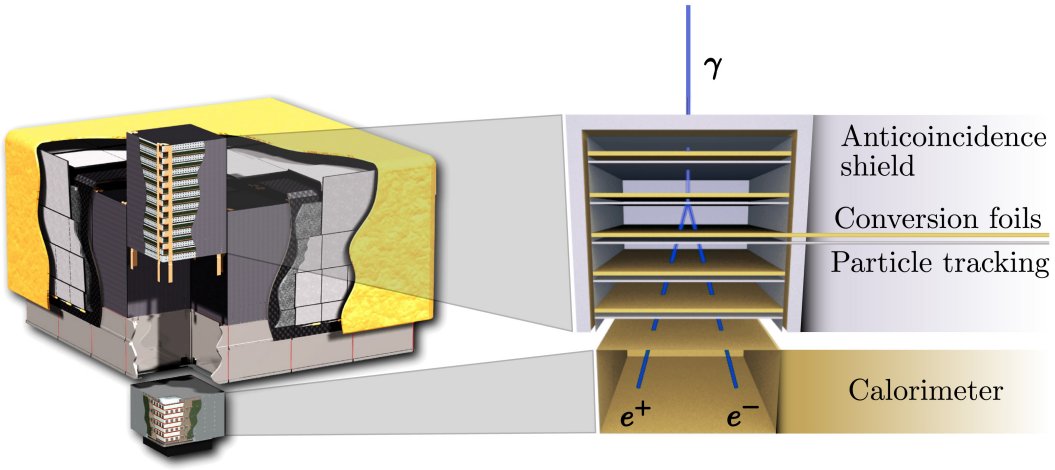

Figure 3.2: LAT instrument on board NASA's Fermi satellite. Figure adapted from Atwood et al. (2009).

and physical processes such as multiple scattering determine the intrinsic point-spread function (PSF) of the instrument.

When the LAT operates in survey mode ($> 80\%$ of the observing time) its pointing system is relative to the zenith, the direction away from the Earth. To cover the whole sky and to achieve a uniform exposure the pointing system oscillates (or "it rocks") perpendicular to the orbital motion 35° north for one orbit then 35° south for another orbit, resulting in a two-orbit periodicity covered in ~ 3 hours. This performance is achieved thanks to its large effective area which on-axis at 1 GeV is ~ 7000 cm^{-2}, as shown in Figure 3.3, and its wide field of view of 2.4 sr. A more detailed description of the LAT instrument is given in Atwood et al. (2009).

3.2.2 Event selection

The data used in this work come from observations over a period of five years, from August 8, 2008 to August 13, 2013. Data analysis is performed with specific analysis tools developed by the LAT team, using the post-launch P7v6 version of the instrument response functions (IRFs). The IRFs are matrices describing the detector performance such as the detection efficiency, the angular resolution, and the energy reconstruction. They depend not only on the instrument itself, but also on the reconstruction and background rejection algorithms, and on any eventual selection of events. Thus, the computation of the IRFs may change during the mission as soon as new improved algorithms are developed or new performing cuts are implemented. Depending on the science being performed, different analysis classes are provided within the analysis tools based on trade-offs amongst the non-photon background, the effective area, and the spatial and energy resolution. In this work, the CR background

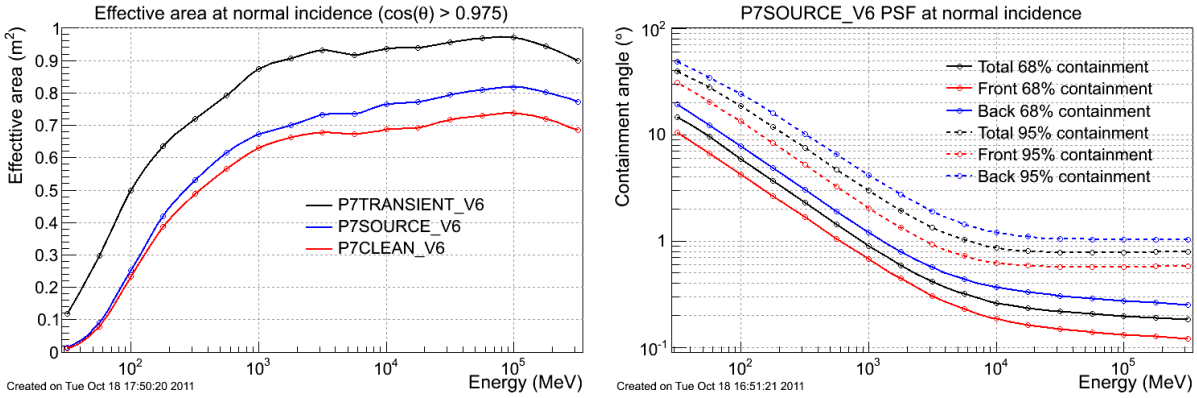

Figure 3.3: *Left*: Fermi-LAT effective area as a function of energy. The effective area is shown for three different analysis classes. The blue curve (P7SOURCE_V6) represents the class chosen in this work. *Right*: point-spread function (PSF) at normal incidence as a function of energy. The solid (dashed) curves show events within 68% (95%) of containment angle from the front of the tracker (red), where the resolution is finer, from the back of the tracker (blue) with a more coarse resolution, and from the entire tracker (black).

is reduced by choosing the P7SOURCE class, recommended by the LAT team for most analyses, which only includes events with high probability of being photons.

Atmospheric γ-rays from the Earth limb, which lies at a zenith angle of 113°, may be a significant source of background. To minimise the spill-over of these photons a zenith angle cut of 100° is applied together with a method of correcting the exposure for the zenith cut itself. The method chosen consists in excluding time intervals where any part of the region of interest (ROI) is beyond the zenith-angle limit. Furthermore, data are not taken in consideration while the observatory is transiting the South Atlantic Anomaly (SAA)[2] and excluded when the rocking angle exceeds 52°.

In the analysis only photons with reconstructed energy greater than 500 MeV, for which the 68%-containment radius of the PSF is narrower than $\sim 1.5°$ (see Figure 3.3), are used. The choice of selecting events above 500 MeV is motivated by the broad PSF at low energy. The broadening may in fact affect the analysis by leading to systematic problems of source confusion in this densely populated region of the Galactic plane.

3.3 Analysis and results

The data analysis is done using the publicly available Fermi-LAT `ScienceTools` version 9.31.1. In particular, spatial and spectral analyses are performed with dedicated scripts based on the python likelihood tools that expand upon the command line tools provided

[2]The SAA is a region over the South Atlantic with a high density of charged particles that are trapped by the configuration of the Earth's magnetic field.

with the Fermi Science Tools package. All the analyses performed with Fermi-LAT are based on the Poisson statistics, the details of which are outlined below.

3.3.1 Statistics of Fermi-LAT analysis

Being the Fermi-LAT a counting experiment, the appropriate way to describe its events is by using the Poisson statistics. Since events are binned according to many observables (i.e., energy, position, time), each bin will contain a small number of counts. Thus, the statistical distribution of these counts, which in fact is the Poisson distribution, cannot be approximated by a normal distribution. The functional form of the Poisson distribution, which gives the probability p_i of observing the detected counts n_i in the i^{th} bin, is

$$p_i = \frac{m_i^{n_i}}{n_i!}\, e^{-m_i}, \tag{3.1}$$

where m_i is the number of counts predicted by the source model in that bin. The source model describes the physical properties of γ-ray sources through their photon flux density, defined as the number of photons per unit energy, area, and time from a solid angle around a certain position. A set of different models depending on a few parameters is provided by the Fermi Science Tools. To connect the models with the data and to estimate the model parameters the method of maximum likelihood is used.

Since the counts in each bin are independent, the likelihood L is defined as the product of the p_i over all bins:

$$L = \prod_i p_i = \prod_i \frac{m_i^{n_i}}{n_i!}\, e^{-m_i}. \tag{3.2}$$

This function can be factored into the product of the terms $m_i^{n_i}/n_i!$, which depend on the data through the values of n_i, and e^{-m_i} which depends purely on the model. When multiplying over all bins the latter writes as

$$\prod_i e^{-m_i} = e^{-\sum_i m_i} = e^{-N_{\text{exp}}}, \tag{3.3}$$

where the sum of m_i is just the total number N_{exp} of counts that the source model predicts.

Equation 3.2 eventually becomes

$$L = e^{-N_{\text{exp}}} \prod_i \frac{m_i^{n_i}}{n_i!}. \tag{3.4}$$

Since the bins have a finite size for which the number of counts n_i may be greater than 1, Equation 3.4 represents a *binned likelihood*. However, the binning destroys information i.e.,

the precise values of the observables describing a count. There is hence a trade-off between the number of bins (and thus the bin size) and the accuracy, and smaller bins result in a more accurate likelihood.

In the limit of infinitesimally small bin size, where n_i can take on only the values 0 or 1, Equation 3.4 becomes an *unbinned likelihood*, defined as

$$L = e^{-N_{\rm exp}} \prod_i m_i, \tag{3.5}$$

where i is now the index over the counts. As opposed to the binned likelihood, Equation 3.5 is calculated using the precise values for each count, and not an average over a finite size bin, and therefore it is the most accurate. The drawback of the unbinned likelihood is however its prohibitive computational load as the number of the observed counts increases.

3.3.2 Data binning

Since the analysis is performed over a large number of observed counts, the binned likelihood analysis is preferred. In binned analyses the data input is a three-dimensional counts map, called *counts cube*, with two spatial axes in equatorial coordinates (right ascension α and declination δ) and a logarithmically spaced axis in energy.

In this work the counts cube, whose spatial dimension defines the ROI, is a square region measuring 28° on a side and centred on $\alpha = 258.39°$ and $\delta = -39.76°$ (J2000), the nominal position of RX J1713.7–3946. The angular binning is chosen to be 0.125° per pixel in stereographic projection to match the resolution of the corrected DGE background.

In order not to lose accuracy in the likelihood analysis 30 energy bins are chosen. This binning allows to accommodate more rapid variations in the effective area with decreasing energy below $\sim$ 1 GeV.

3.3.3 Background modelling

Due to the PSF-broadening at low energy, the γ-ray background is modelled in an acceptance region, called the source region, which is 5° larger than the ROI. This accounts for sources that lie just outside the data region, but whose photons may end up in the data set.

The background model includes 174 point-like sources and 2 extended sources listed in the 2$^{\rm nd}$ Fermi-LAT catalog [79]. The source 2FGL J1712.4–3941 is not considered in the model because spatially coincident with RX J1713.7–3946. Furthermore, the corrected DGE background template together with the corresponding isotropic template[3] that accounts for extragalactic emission and residual cosmic-ray contamination are also included.

[3]The isotropic template is available from the Fermi Science Support Centre.

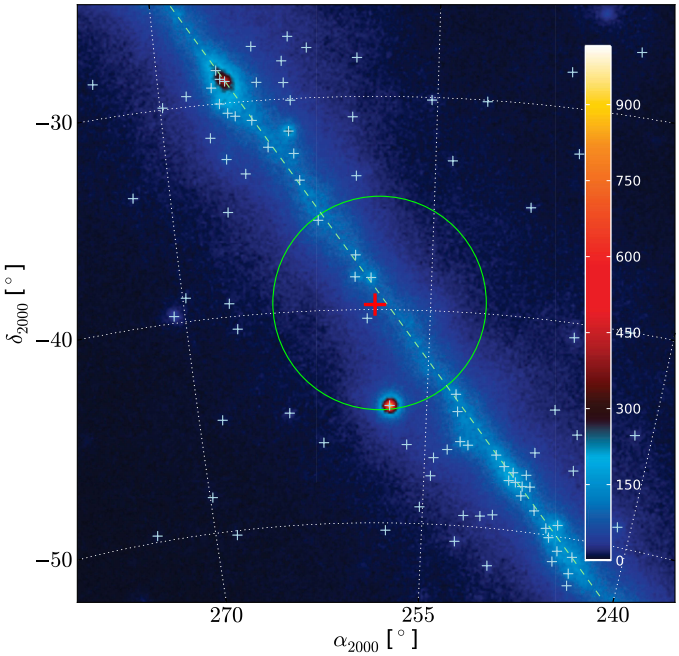

Figure 3.4: Counts map of the region of interest (ROI) used in this work. Sources of the 2nd Fermi-LAT catalog are marked by light blue crosses. The green dashed line denotes the Galactic plane and the red cross represents the nominal position of RX J1713.7–3946. During the fit procedure the parameters of the sources inside the green circular region of 5° radius are free to vary.

Amongst the point-like and extended sources, 105 lie inside the ROI and most of them are modelled with power-law energy spectra. The spatial and spectral parameters of sources outside a circular region of 5° radius centred at the nominal position of RX J1713.7–3946, are kept fixed at the values given in the catalog. Inside this region the spectral parameters of 7 sources along with the normalisation of the diffuse components are permitted to freely vary. Thus, the final set of free parameters is reduced to 20, a number which allows the fit to converge. Figure 3.4 shows the ROI with 105 sources of the 2nd Fermi-LAT catalog and the circular region of 5°.

3.3.4 The HISA contribution to the DGE

To study the impact of the correction for the HISA on the DGE two binned likelihood analyses are performed, one with the standard Fermi-LAT DGE template and one with the corrected DGE template. The detailed setup of the likelihood fit, used for the standard Science Tool *gtlike*, is identical for both analyses. The two likelihood fits are performed by assuming as a spatial template for RX J1713.7–3946 a uniform disk of 0.5° radius.

The best-fit model is determined by comparing the logarithm of the maximum likelihoods of the two models, where higher values are qualitatively better fit. The difference between

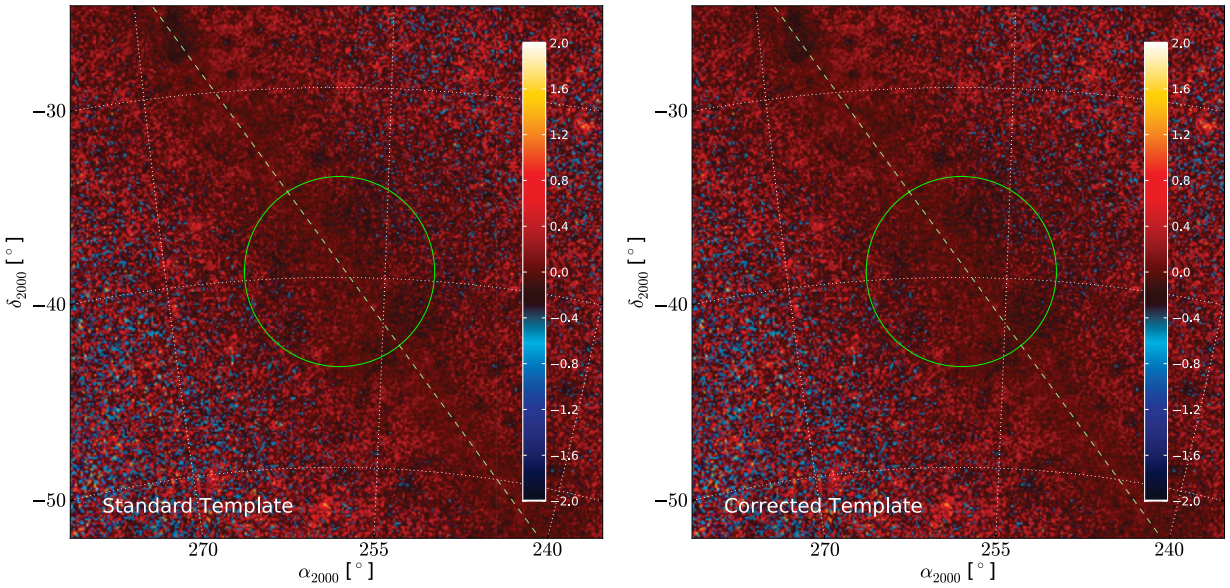

(a) Standard DGE template. **(b)** Corrected DGE template.

Figure 3.5: Residual maps calculated for the whole energy range of 0.5–300 GeV under the null (a) and alternative (b) hypotheses for the DGE background. The maps are shown in units of (model counts)$^{1/2}$.

the two models is measured by the likelihood ratio test and is given in terms of the test statistics (TS) [80] defined as

$$\mathrm{TS} = 2\,(\ln L - \ln L_0) = 2\,\ln\left(\frac{L}{L_0}\right), \tag{3.6}$$

where L_0 is the likelihood of the null hypothesis (i.e., the standard DGE background) and L is the alternative hypothesis (i.e., the corrected DGE background). The fit is performed in the whole energy range spanning from 500 MeV to 300 GeV. The results of the fits indicate that the alternative hypothesis is favoured over the null hypothesis by a significance[4] of $\sim 4\,\sigma$. Figures 3.5a and 3.5b show the residual maps under both the null and alternative hypotheses integrated over the full energy range. The residual is defined as

$$r = \frac{n - m}{\sqrt{m}}, \tag{3.7}$$

where n and m are the detected counts and the counts predicted by the model, respectively. Both maps look almost identical and the residual counts are consistent with the expected

[4]The significance is measured in units of σ (i.e, the standard deviation of a normal distribution), where 1σ to first order corresponds to $\sqrt{\mathrm{TS}}$. A significance value of 3σ is usually taken as a strong hint for the presence of a source or for the goodness of a model, whilst 5σ is considered the threshold for claiming a source discovery or confirming a model validity.

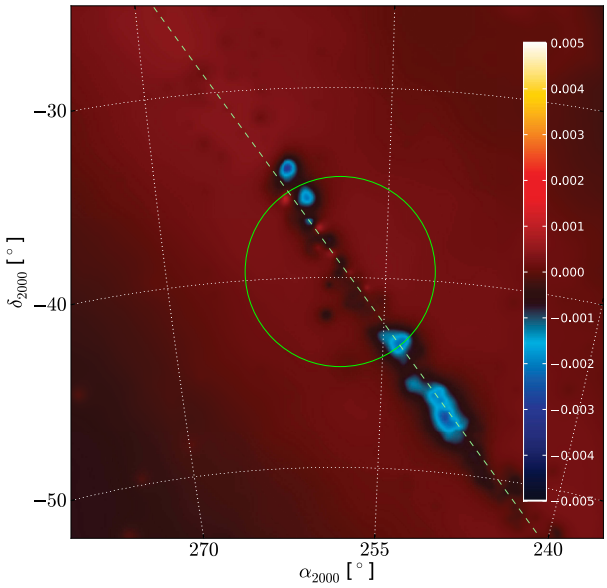

Figure 3.6: Residual map calculated by directly comparing the two hypotheses for the DGE background.

statistical fluctuations, implying that the region around RX J1713.7–3946 is well described by both models. Small differences however can be seen by directly comparing the counts predicted by the two models (i.e., $[m_1 - m_2]/\sqrt{m_2}$, where m_1 and m_2 refer to the null and the alternative hypotheses, respectively), as shown in Figure 3.6. As expected, those differences affect a region along the Galactic plane where most of the corrections for HISA are applied.

Although this result is not particularly strong, the significance of 4σ is high enough to assert that the cold absorbing hydrogen clouds (i.e., HISA gas) represent a non-negligible target for CRs and hence their contribution to the DGE should be taken into account. For this reason, during all the following analyses the corrected DGE template is used.

3.3.5 Detection significance of RX J1713.7–3946

The first 2 years of science operation of Fermi, LAT has established firm detection of γ-ray emission from RX J1713.7–3946 with statistical significance high enough for it ($\sim 9\sigma$ or TS = 79) to be distinguished from the background radiation. After 3 years since the first detection, for a total of 5 years of observation, it is expected that the source significance be higher and the accumulated statistics be enough to clearly show the spatial distribution of the emission coincident with the SNR.

In this regard, a detection significance map (or TS map) is calculated in terms of the test statistic as defined in Equation 3.6. As null and alternative hypotheses a pure background

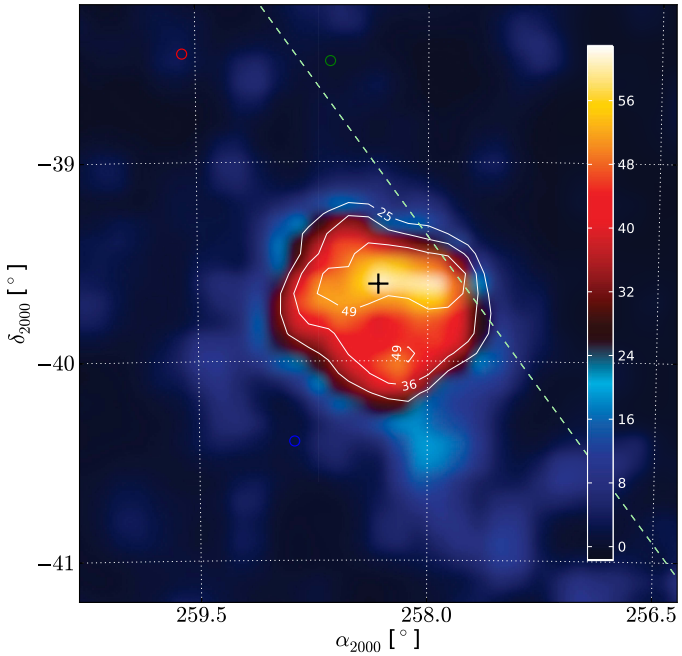

Figure 3.7: Map of the test statistic (TS) for a point-like source in the region around RX J1713.7–3946. The black cross denotes the maximum value of the map. Red circles indicate the position of the second Fermi-LAT catalog sources in the background model. Shown are also the contours for different values of TS.

(i.e., there is no source) and a point-like source are respectively assumed. The method to create the TS map consists of moving a putative point-like source through a grid of locations on a square region. The region measures $\sim 3^\circ$ on a side and is centred at the nominal position of the SNR. At each point of the grid the likelihood ratio of the null hypothesis with respect to the alternative hypothesis, in which the parameters of the point-like source are free to vary and those of all background components are fixed at the values found in the previous likelihood analysis (see Section 3.3.4), is evaluated. The resolution of the grid is 0.1° which implies 961 likelihood analyses. The resulting significance map in units of test statistic (TS) is shown in Figure 3.7. The white significance contours starting from 5σ (TS = 25) suggest a spatially extended emission from the shell of the SNR. Particularly interesting is the local enhancement of the emission in the northwest region of the shell with a significance $> 7\sigma$ (TS > 49). This enhancement coincides with a similar feature detected by X-ray and very high energy (VHE) γ-ray observations (i.e., H.E.S.S.).

3.3.6 Position and spatial extension of RX J1713.7–3946

To find the best position of the source and minimise hence the systematic uncertainties a number of maximum likelihoods is performed. The method is the same used to find

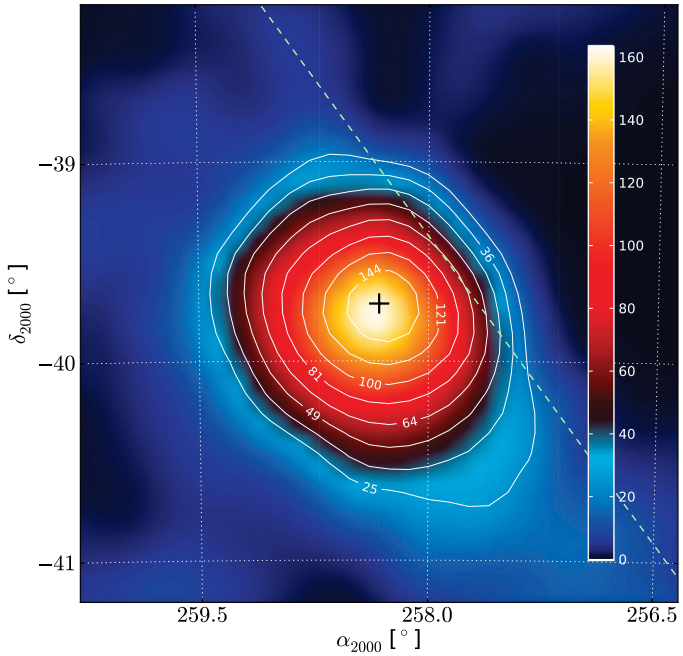

Figure 3.8: Map of the test statistic for the study of the best RX J1713.7–3946 position, which is marked by a black cross. The green dashed line is the location of the Galactic plane. Shown are also the contours for different values of TS. A TS of 25 corresponds to a significance of 5σ.

the detection significance. The only difference is the assumption used for the alternative hypothesis. To model RX J1713.7–3946 an extended template based on a uniform disk with a radius of 0.5° is used instead of a point-like source.

The resulting TS map is shown in Figure 3.8. The best-fit centroid for the disk model, marked by a black cross, is found to be $\alpha = 258.32°$ and $\delta = -39.71°$ in J2000 with an error radius of 0.02° at the 68% confident level. This location corresponds to the highest excess in the TS map, namely TS = 160. The best-fit position is about 0.07° offset of the nominal coordinates in direction of the Galactic plane, marked in the figure by the green dashed line. All the following analyses are performed using a spatial template centred at these best-fit coordinates.

To investigate the spatial morphology of the emission associated with RX J1713.7–3946 a number of spatial templates are tested. In particular, five templates based on a uniform-disk shape with different radii varying from 0.5° to 0.7° in steps of 0.05° are evaluated. Furthermore, a template of the emission as detected by the H.E.S.S. telescope is also taken into account. In Figure 3.9 are shown all these spatial templates after being convolved with the Fermi-LAT PSF. To evaluate which one of them fits the emission better six maximum likelihood analyses are performed. During the analyses the background components are treated as described in Section 3.3.3. The best-fit parameters and the significance of the

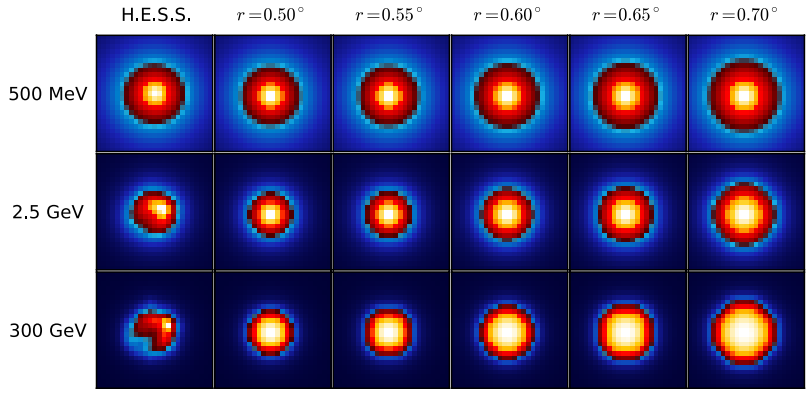

Figure 3.9: Spatial templates used to model the emission associated with RX J1713.7–3946. The templates are convolved with the Fermi-LAT PSF and are shown for three different energies. Due to the broadening of the PSF at low energies the detailed shape and size of the six templates can only be distinguished at high energies.

source for each analysis are summarised in Table 3.1. All models show a high test statistic value ($150 \leqslant \mathrm{TS} \leqslant 163$) implying that the emission is well resolved by the LAT as an extended region. The results for uniform-disk templates show that the TS slightly decreases after a radius of 0.55°, a value which is consistent with the findings reported by the previous LAT analysis [78] and by X-ray measurements [81]. The TS value for the uniform disk of radius 0.55° is also very close to that of the H.E.S.S. template. However, since the difference between these two TS values is considerably small ($\Delta\mathrm{TS} = 2$), this leads to the conclusion that the LAT is not sensitive to the detailed shape of the emission region. Nevertheless, the spatial extension model based on the H.E.S.S. template, which shows the highest TS value, is used in the following as the default model.

Source morphology	Flux[a]	Photon index	Test statistic
Uniform disk ($r = 0.50°$)	4.982 ± 0.916	1.508 ± 0.075	160
Uniform disk ($r = 0.55°$)	5.122 ± 0.941	1.509 ± 0.075	161
Uniform disk ($r = 0.60°$)	5.449 ± 1.069	1.513 ± 0.075	159
Uniform disk ($r = 0.65°$)	5.547 ± 1.052	1.514 ± 0.075	156
Uniform disk ($r = 0.70°$)	5.908 ± 1.216	1.521 ± 0.076	150
H.E.S.S. template	5.522 ± 1.075	1.528 ± 0.074	163

Table 3.1: Morphological analysis of the γ-ray emission associated with RX J1713.7–3946.

[a]The integral flux of RX J1713.7–3946 is calculated over the energy range 500 MeV–300 GeV and it is given in units of 10^{-9} photons cm^{-2} s^{-1}.

3.3.7 Energy spectrum of RX J1713.7–3946

The spectral properties of the emission associated with the SNR are those found in the previous analysis performed using the H.E.S.S template as spatial model for RX J1713.7–3946. Such analysis is performed from 500 MeV to 300 GeV, with the background components treated as described in Section 3.3.3, and the spectral model of RX J1713.7–3946 described by a simple power law of the form

$$\frac{dN}{dE} = N_0 \left(\frac{E}{E_0}\right)^{-\gamma}, \tag{3.8}$$

where N_0 is the prefactor, E_0 the energy scale, and γ the spectral index. The fit yields a $\gamma = 1.53 \pm 0.07$ and a TS value of 163 for RX J1713.7–3946, which corresponds to a detection significance of about 13σ. The measured integral photon flux above 500 MeV is $F_{500} = (5.52 \pm 1.07) \times 10^{-9}$ photons cm^{-2} s^{-1}.

In order to obtain a spectral energy distribution (SED) for the SNR, the entire energy range is divided into 9 logarithmically spaced energy bins. For each individual bin a likelihood fit is performed by using the spectral model and parameters obtained in the overall fit. For those bins where the TS is less than 7 a 95% confidence-level flux upper limit is derived.

Since uncertainties in the spatial distribution of the DGE or in the source shape template can contribute to the systematic errors, the data are re-fitted for several variations of the default model. First, the corrected DGE background model is replaced by the standard DGE background model. Second, the H.E.S.S. template is changed with the uniform-disk templates. Furthermore, uncertainties due to instrumental effects are also taken into account. The flux measurement in fact depends on the knowledge of the effective collecting area of LAT as a function of energy. The systematic error in the effective area for the P7SOURCE_V6 event class may be quoted as 10% at 100 MeV, 5% at 560 MeV, and again 10% at 10 GeV and above [82]. All these contributions are accounted for in the estimation of the overall systematic uncertainties.

The resulting energy spectrum of RX J1713.7–3946 is shown in Figure 3.10 together with H.E.S.S measurements (orange data points). The green solid line denotes the best fit for a power law model, with the two bands indicating the statistical errors (green band), and the systematic uncertainties (light-gray band). The 9 Fermi-LAT data points (black crosses) only include statistical errors. On the background of the figure the gray histogram represents the distribution of TS values obtained for each bin of the Fermi-LAT SED. The dotted line at the bottom of the histogram denotes the threshold (TS = 7) for setting a 95% confident-level upper limit on the Fermi-LAT data points. The physical interpretation of the SED will be discussed in the next section.

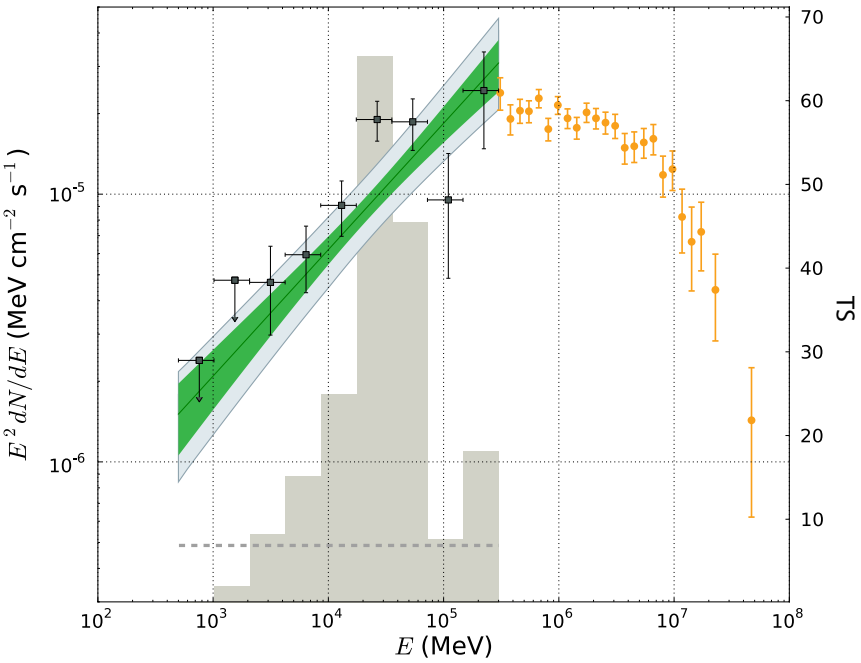

Figure 3.10: Broadband γ-ray spectrum of RX J1713.7–3946 as measured by this work (black points) and by H.E.S.S. (orange points). The green solid line is the overall best-fit model in the energy range from 0.5 GeV to 300 GeV. The two bands denote statistical (green) and systematics (light-gray) uncertainties. The histogram indicates the TS value for each energy bin. The dotted line is the threshold for setting a 95% confident level upper limit.

3.4 Discussion

The nature of the GeV γ-ray emission coincident with RX J1713.7–3946 cannot be understood using only data from the GeV-to-TeV observations. This because, as already mentioned in Chapter 1, the spectrum of such emission can be easily reproduced by different emission mechanisms. To investigate its origin is thus necessary to perform a phenomenological spectral modelling in multi-wavelength. In this regard, two broadband spectral fits using X-ray (Suzaku [83]), GeV γ-rays (Fermi-LAT), and TeV γ-rays (H.E.S.S) data are used to assess the feasibility of two scenarios (leptonic and hadronic) and to calculate the energetics associated to the interacting particle population. During the fit procedure a simplified picture is assumed that the interacting protons and electrons are accelerated at the same site and are distributed uniformly inside a common effective volume $V = (4\pi/3)R^3$, where R is the radius of the SNR in γ-rays. The model accounts for three emission mechanisms: electron synchrotron radiation, constrained by X-ray data, inverse Compton scattering and neutral pion decay γ-rays, constrained by the GeV-to-TeV observations. For IC scattering of electrons, the interstellar radiation fields providing the seed photons include the CMB, infrared, and four optical star light components for which the energy densities and graybody temper-

Model	$K_{\rm ep}$	α	$E_{\rm br}$ (TeV)	B (μG)	$n_{\rm HI}{}^{a}$ (cm^{-3})	$W_{\rm p}$ ($W_{\rm e}$) (10^{49} erg)	ϵ (%)
Leptonic	2×10^{-2}	2.204	37.8	9.3	0.2	21.8 (0.43)	22.3
Hadronic	7×10^{-4}	1.908	26.1	13.6	0.8	23.6 (0.01)	23.6

Table 3.2: Parameters of the leptonic and hadronic models used to fit the broadband spectrum. The electron-to-proton ratio and the density gas are fixed parameters during the fit.

[a]These values refer to the post-shock gas which is ~ 4 times more dense than that of the pre-shock given in the text.

atures are tuned according to Shibata et al. (2011) [84]. Due to the Klein-Nishina cutoff usually only scattering of CMB photons is important. However, over the inner Galaxy where RX J1713.7–3946 is located the contribution to the total IC emission given by the optical and infrared photons is comparable to that of the CMB since their energy densities are higher than those far from the Galactic centre [85].

The γ-ray spectra of IC and synchrotron radiation are calculated using differential cross sections given by Sturner et al. (1997) [86]. The γ-ray spectrum generated by hadronic interactions (i.e., $p_{\rm CR} + p_{\rm ISM} \rightarrow \pi^0 + X$) and the subsequent decay of secondary particles (i.e., $\pi^0 \rightarrow 2\gamma$) is instead obtained using the γ-ray-production matrix produced by Huang et al. (2007) [87]. The shape of the particle spectrum is assumed to be the same for electrons and protons:

$$J(E) = K_{\rm ep}\, N_0\, E^{-\alpha} \exp\left(-\frac{E}{E_{\rm br}}\right), \tag{3.9}$$

where $K_{\rm ep}$ is the electron-to-proton ratio, N_0 is a normalisation factor, α is the particle spectral index, and $E_{\rm br}$ is the spectral break in the particle spectrum.

Figure 3.11 shows the fitted broadband spectrum of RX J1713.7–3946 calculated for the two scenarios. For both models, the spectrum is reproduced for the GeV-to-TeV emission first, adjusting the spectral index and the normalisation to fit the high-energy data. The particle and the photon spectral indices (α and γ, respectively) are linked by the relation $\alpha = 2\gamma - 1$. Accounting for the errors on γ, the allowed values for α are hence 2.056 ± 0.148. With α and N_0 constrained, the magnetic field B and the energy break $E_{\rm br}$ are varied to also reproduce the X-ray data. Stringent constraints on the gas density in the SNR, required for synchrotron and π^0-decay spectra calculations, are given by the absence of a clear detection of thermal X-ray emission [83]. In particular, in this analysis values of the pre-shock gas density of $n_{\rm HI} = 0.05$ cm^{-3} and $n_{\rm HI} = 0.2$ cm^{-3} are used for leptonic and hadronic models, respectively [88].

The spectral fit results are shown in Table 3.2. Within the leptonic scenario, the synchrotron model seems to fit the X-ray data reasonably well with a soft electron spectral index

and a low magnetic field which is comparable to other studies (e.g., [88]). The high-energy region, on the other hand, suffers some mismatches between the model and the GeV Fermi-LAT spectrum. In particular, two spectral points around $\sim$ 50 GeV are above the model predictions. The peak of the inverse Compton emission, however, reproduces the H.E.S.S. data in a correct way.

On the other hand, the hadronic model faces more difficulty in explaining the broadband spectrum. While at low energy the synchrotron model is in agreement with the X-ray data also in this case, at higher energy the flat peak of the π^0-decay emission completely covers the low-energy tail of the Fermi-LAT spectrum up, where a gradual low-energy rollover would be expected. In the face of such a discordance the hadronic scenario appears to be disfavoured.

In both models a large energy content stored in the protons ($W_\mathrm{p} \sim 2 \times 10^{50}$ erg) is required in order to reproduce the observed γ-ray luminosity. This values is somewhat a factor of 2 higher than the assumed standard value of $\leqslant 10^{50}$ erg, corresponding to $\sim 10\%$ of the supernova energy explosion released in particles energy, but it is still a reasonable estimation.

This simple model does not account for the possibility that the energetic proton and electron populations can potentially be accelerated at different sites in the SNR, and interact with media under very different conditions and inside different effective volumes. For example, the shell can be responsible for the acceleration of part of the interacting electron population, while the protons can be interacting predominantly in the molecular cloud region near the northwest part of the SNR. In such cases, the assumptions of a common interaction volume and spectral shape for protons and electrons is not strictly true, so the broadband data may not be easily fitted simultaneously on the same ground but should be considered separately, and the fitted parameters and estimated particle energy contents would require more careful reassessments.

3.5 Conclusions

In this analysis an extended GeV-γ-ray source is found in the direction of the SNR RX J1713.7–3946 using more than five years of observation with Fermi-LAT and a diffuse Galactic γ-ray background corrected for the HI self-absorption. The positional coincidence between the Fermi-LAT γ-ray emission and the SNR RX J1713.7–3946 suggests that the γ-ray emission is produced by shock-accelerated particles within the remnant.

Based on the extension study described in Section 3.3.6 and the spectral analysis described in Section 3.3.6 as well as in the discussions section, the main conclusions are:

- The γ-ray emission from RX J1713.7–3946 is detected at 13σ level: the emission is extended with a radius $r = 0.55^\circ$ in the energy range between 0.5 GeV and 300 GeV.

- The extended source region overlaps almost completely the region observed by H.E.S.S. in the very-high energy regime. Both experiments measure an enhancement feature in the northwest region of the remnant probably due to particles interacting with a local molecular cloud.

- The measured spectrum of RX J1713.7–3946 shows a hard spectral index of $\gamma = 1.528 \pm 0.074$ with an integral flux above 500 MeV of $F_{500} = (5.52 \pm 1.07) \times 10^{-9}$ photons cm^{-2} s^{-1}.

- The H.E.S.S. spectrum appears to be a natural extension, within errors, of the LAT SED. Along with the high spatial correlation between the emission regions observed by LAT and H.E.S.S., it may suggest a common origin for the observed GeV and TeV emission.

- A phenomenological spectral modelling in multi-wavelength is needed to draw some conclusion about the nature of the emission. The chosen parameters sets shown in Table 3.2 are not unique in their ability to fit the broadband SED, but are the most representative sets. Nevertheless, the GeV spectrum measured in this work does not agree with the expected flux predicted by a hadronic model even using different parameters sets. This implies that the hard Fermi-LAT spectrum cannot be ascribed to the π^0-decay emission. The leptonic scenario turns out instead to be the most natural picture for the high-energy γ-ray emission of RX J1713.7–3946. Although disfavoured, however the hadronic scenario cannot be ruled out.

- The fits of the broadband SED show that a common particle power-law spectrum with an exponential cutoff for electrons and protons faces some difficulty in simultaneously accounting for the X-ray, GeV γ-ray, and TeV γ-ray observations. A more complex model with additional parameters and more flexible assumptions could modify the shape of the broadband spectrum and realise a better description of the γ-ray data.

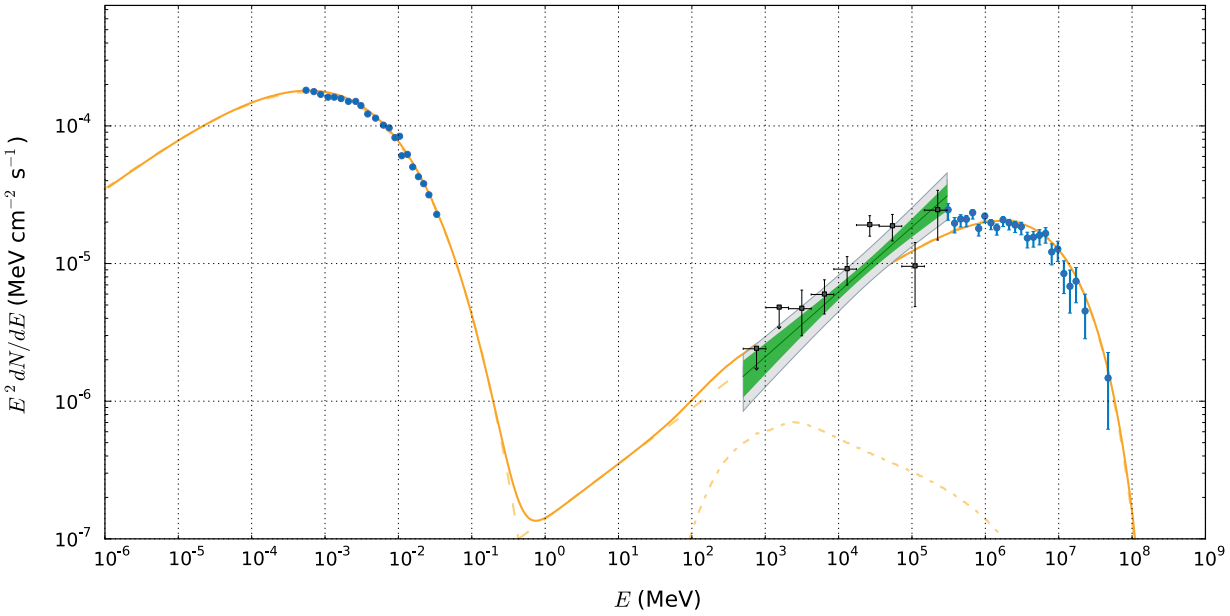

(a) Leptonic model.

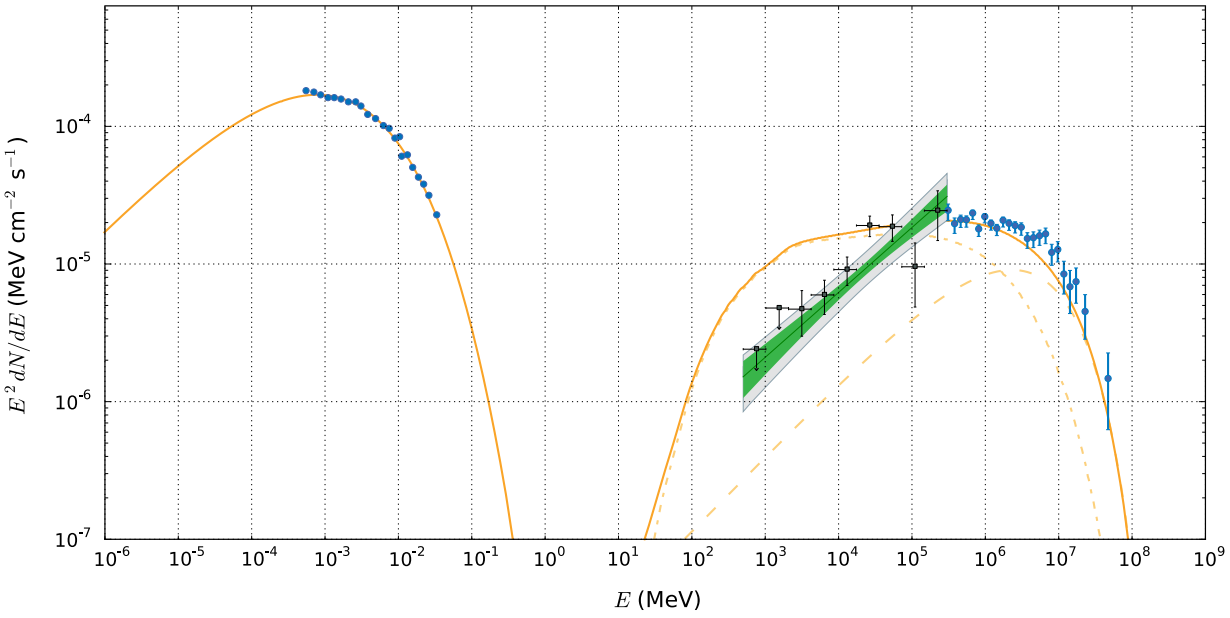

(b) Hadronic model.

Figure 3.11: Phenomenological multi-wavelength models of RX J1713.7–3946. In both panels, at low energy the blue circles denote X-ray data by Suzaku, while at higher energy the data are the same as in Figure 3.10. The dashed line represents synchrotron radiation and inverse Compton, the dash-dotted line the neutral-pion decay, and the solid line is the total model.

4

Dark matter studies of Segue 1

This chapter presents an overview of a previous work on dark matter that was jointly performed with other authors. The analysis presented here is not related to the main subject of the thesis discussed thus far.

This work is based on the analysis of the dwarf spheroidal galaxy Segue 1. Its intent is to investigate, using observations from Fermi-LAT, different scenarios about the dark matter density profile of Segue 1, and to set upper limits on the annihilation cross-section of dark matter particles. Finally, a comparison of these limits with the cross section estimate from dark matter abundance is discussed.

This study has been published in *Physical Review D* [89].

4.1 Introduction

The nature of dark matter (DM) is one of the most fascinating mysteries of the modern physics. A variety of observations provide a tight constraints on the amount of baryonic material[1] in the Universe, which is found to be 5% of the total matter (e.g., [90], [91]). Many DM candidates have been proposed so far by particle physicists. The most likely one is however the class of the weakly interacting massive particles (WIMPs). They are so popular because they arise naturally from theories that seek to extend the standard model of particle physics, the most promising of which seems to be the supersymmetry (SUSY, see Ref. [92] for a comprehensive review). Furthermore, WIMP particles (denoted by χ)

[1]Baryonic matter is the ordinary atomic matter composed by baryons. The most common baryons in nature are protons and neutrons.

naturally achieve the correct relic abundance in the early Universe

$$\Omega_\chi h^2 = \frac{m_\chi n_\chi}{\rho_c} \approx \frac{3 \times 10^{-27}\,\mathrm{cm^3 s^{-1}}}{\langle \sigma v \rangle}, \tag{4.1}$$

where h is the Hubble parameter in units of 100 km s^{-1} Mpc^{-1}, m_χ and n_χ are the mass and the number density of DM particles respectively, $\rho_c \simeq 10^{-5} h^2$ GeV cm^{-3} is the today's critical density, and $\langle \sigma v \rangle$ is the DM self-annihilation cross section times the relative velocity of two WIMPs averaged over their velocity distribution. Given the measured value $\Omega_\chi\, h^2 = 0.1109 \pm 0.0056$ [93], in order to achieve the appropriate relic density a WIMP of any mass must have $\langle \sigma v \rangle \simeq 3 \times 10^{-26}$ cm^3 s^{-1}, corresponding to a cross-section typical of weak interactions in the standard model, hence the name WIMPs.

In the simplest WIMP models, dark matter particles can self-annihilate into particles of the Standard Model such as quarks, leptons, and gauge bosons. Their annihilation gives rise to secondary particles that eventually hadronise or decay. Among the final products γ-rays are particularly advantageous as, unlike charged particles, they freely stream through the Galaxy and so they direct point back to their source. These γ-rays give rise to continuous spectra, unlike γ-rays directly produced by the annihilation of two DM particles that provide a monochromatic line emission. The detection of γ-rays could be hence an attractive possibility to clarify the nature of these particles.

Different astrophysical objects are used as target to search for dark matter signals. Among these the class of dwarf spheroidal (dSph) galaxies surrounding the Milky Way. These particular galaxies, which are a subclass of the dwarf elliptical galaxies, have a peculiarity that makes them very promising objects for detecting dark-matter annihilation. They have low astrophysical γ-ray backgrounds, because they contain almost no gas or dust, no star-forming regions, and probably few millisecond pulsars. Thus, almost any high-energy signal detected from dSph galaxies could be ascribed to the signal of dark-matter annihilation.

Among the known dSph galaxies the best candidate for indirect detection of DM is probably Segue 1. This galaxy is in fact the closest to Earth and being at high latitude it is not obscured by the Galactic disk. Furthermore, it is the most DM-dominated galaxy known [94]. These features have hence contributed to the choice of Segue 1 as target for the analysis presented here, whose details are given in the following sections.

4.2 The γ-ray flux from WIMP annihilation

The analysis of Segue 1 is performed assuming as DM candidate all WIMPs whose final annihilation products are heavy particles. Among these, the most likely candidate is the

neutralino, the lightest SUSY particle. The γ-ray emission from Segue 1 is measured using data from Fermi-LAT, currently the most sensitive instrument to photons originating by the annihilation of neutralinos with mass m_χ ranging from 10 GeV to 1 TeV. To set the upper limits on the cross-section of neutralino annihilation and thus to constraint dark-matter models, the measured γ-ray emission, that is, the differential γ-ray flux due to WIMPs annihilation from a solid angle $d\Omega$ and an energy interval dE which is measured by an observer on Earth, is modelled as

$$\frac{d\phi_\gamma}{d\Omega\, dE} = \frac{\langle \sigma v \rangle_c}{8\,\pi\, m_\chi^2} \frac{dN_\gamma}{dE} F, \tag{4.2}$$

where $\langle \sigma v \rangle_c$ is the velocity averaged annihilation cross section, dN_γ/dE is the γ-ray spectrum generated per WIMP annihilation, m_χ is the neutralino mass, and F is defined as

$$F = \int_{\text{l.o.s.}} C \frac{\langle \sigma v \rangle}{\langle \sigma v \rangle_c} \rho^2\, dl. \tag{4.3}$$

The quantity F is the integral performed along the line of sight of the squared DM density profile ρ of Segue 1 at the projected radius, and it depends on two terms.

- The first term C is the so-called *boost factor*, defined as the ratio $\langle \rho^2 \rangle / \langle \rho \rangle^2$. The boost factor takes into account the enhancement of the annihilation signal due to the possible presence of dark-matter substructures. As this possibility is not sufficiently explored for Segue 1, its contribution is not considered here and a value of $C \equiv 1$ is used throughout this work.

- The second term is the ratio $\langle \sigma v \rangle / \langle \sigma v \rangle_c$ which allows for a possible dependence of $\langle \sigma v \rangle$ on the particle velocity v, i.e. the Sommerfeld effect (a brief description is given in Section 4.3.2). The quantity $\langle \sigma v \rangle_c$ has a characteristic value chosen such that for velocity independent models $\langle \sigma v \rangle = \langle \sigma v \rangle_c = \text{constant}$.

Upper limits on the annihilation cross section are hence derived solving Equation 4.2 for $\langle \sigma v \rangle_c$. To calculate F, four models describing the DM density distribution ρ of Segue 1 are used. They are illustrated in Section 4.3. The γ-ray spectrum dN_γ/dE generated by different annihilation channels is derived using the `DarkSUSY` package [95]. A description of these spectra is presented in Section 4.4. Finally, the differential γ-ray flux $d\phi_\gamma/(d\Omega\, dE)$ is obtained by Fermi-LAT data, whose analysis is described in Section 4.5.

4.3 Description of dark matter models

To investigate the properties of the dark-matter density profile in the region of Segue 1 four models based on different assumptions are used.

4.3.1 Models with velocity independent cross section

The first two models assume that $\langle \sigma v \rangle$ does not depend on the velocity so that $\langle \sigma v \rangle = \langle \sigma v \rangle_c$ and Equation 4.3 simplifies to

$$F = \int_{\text{l.o.s.}} \rho^2 \, dl. \tag{4.4}$$

The first model, called *standard model*, is based on the Einasto density profile

$$\rho = \rho_s \, e^{-2\,n\left[(r/r_s)^{1/n}-1\right]}, \tag{4.5}$$

where the values for the set of parameters are taken from Ref. [96], with the scale density $\rho_s = 1.1 \times 10^8$ $\mathrm{M}_\odot$ kpc^{-3}, the scale radius $r_s = 0.15$ kpc, and the index $n = 3.3$.

To test how sensitive the annihilation signal is to the choice of the profile, a second model called *minimal model* is used. This model is based on two assumptions. First, that the total mass of Segue 1[2] within a radius $r_0 = 67$ pc is the same as that of the standard model. Second, that the DM density profile ρ is homogeneously distributed within r_0 and is the same as that of the standard model beyond.

Among all the profiles this last model gives the minimal predicted signal. Furthermore, in this conservative case the DM density profile changes the angular extent of the annihilation signal in a way that makes it larger compared to a sharper density profile, for which a point-source analysis may be more suitable.

4.3.2 Models with velocity dependent cross section

The last two models account for the Sommerfeld effect with $\langle \sigma v \rangle$ depending on v. In this case Equation 4.3 becomes

$$F = \int_{\text{l.o.s.}} \frac{\langle \sigma v \rangle}{\langle \sigma v \rangle_c} \rho^2 \, dl. \tag{4.6}$$

Both model are based on the same Einasto density profile described by Equation 4.5, but differ for the assumptions on $\langle \sigma v \rangle$. Before describing these models, it is however useful to give a brief overview of the Sommerfeld effect.

[2]The mass of Segue 1 within half-light radius is $\sim 5.8 \times 10^5$ $\mathrm{M}_\odot$ [94], where half-light radius refers to the radius within which half of the galaxy's luminosity is contained.

The Sommerfeld effect, also known as Sommerfeld enhancement, is a non-relativistic quantum effect occurring when annihilating particles, like neutralinos in this case, interact through a potential of some sort. The effect of this potential is to distort the initial wave function $\Psi(\vec{r})$ of the incoming two-particle state. Such effect can be quantified using the ratio between the "undistorted" two-body wave function of the incoming particles ($r \to \infty$) and the "distorted" two-body wave function at the point of the annihilation ($r = 0$). This gives the so-called *Sommerfeld enhancement factor* that is specifically defined as

$$S = \frac{|\Psi(\infty)|^2}{|\Psi(0)|^2}. \tag{4.7}$$

The standard approach to compute the enhancement factor is to solve numerically the Schrödinger equation for the incoming two-particle state to find the wave function distortion. The "enhanced" annihilation cross section is given eventually by $\langle \sigma v \rangle = S \langle \sigma v \rangle_c$.

In simple cases (e.g., where the interaction between the two particles is due to an attractive Yukawa potential), S scales as $\sim 1/v$, where v is the relative velocity between two annihilating neutralinos. This $1/v$ scaling is valid only for $(v/c) \gtrsim (m_\phi/m_\chi)$, where c is the speed of light and m_ϕ is the mass of the force carrier ϕ. At very small velocities S saturates at value proportional to m_χ/m_ϕ [97].

Depending on the model assumptions, if v is low enough a significant enhancement might hence occur. However, if the dark-matter particles interact via standard gauge bosons[3], the enhancement is significant only for WIMPs with heavy masses (i.e., in the TeV range). On the other hand, if the interaction is mediated by lighter particles the enhancement occurs even in the case of low-mass WIMPs.

The $1/v$ enhancement of the annihilation cross section can be parametrized as

$$\langle \sigma v \rangle = \frac{v_c}{v} \langle \sigma v \rangle_c, \tag{4.8}$$

where the characteristic velocity v_c represents the escape velocity from the centre of Segue 1. Such a velocity can be derived by the gravitational potential of Segue 1, $\phi(r)$, which in turn can be calculated from the Einasto density profile ρ, defined in Equation 4.5. Eventually, the value of the escape velocity is found to be $v_c = 2\sqrt{-\phi(0)} \simeq 60$ km s^{-1}.

Despite the velocity distribution of the DM particles within the source is not well known [98], in this work two hypotheses are considered. The first, called *virial model*, is that v is proportional to the escape velocity $v_{\rm esc}$. A similar behaviour occurs also when the radial motion of dark matter particles dominates [99]. In the second hypothesis, called *orbital model*, the velocity v is assumed to be proportional to the orbital velocity $v_{\rm orb}$. This case is also typical

[3]The most heavy gauge boson known thus far is the Higgs boson with a mass of ~ 125 GeV.

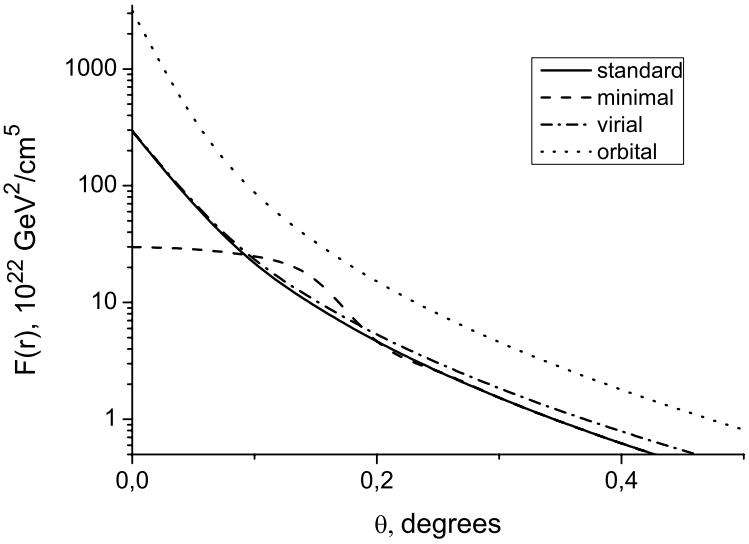

Figure 4.1: Angular distribution of the signal as defined in Equation 4.3 for the four models described in the text. The quantity θ is the angular distance from the centre of the source.

for the isothermal dark-matter halo [100]. The small velocity dispersion of stars at the centre of Segue 1, that was observed to be ~ 3.7 km s^{-1} [94], seems to favour this last scenario. The two hypotheses for the distribution of v can be summarised as follows,

$$v = \begin{cases} 2\,v_{\rm esc}/\sqrt{2} = 2\sqrt{-\phi(r)} & (\textit{virial model}) \\ \sqrt{2}\,v_{\rm orb}(r) & (\textit{orbital model}) \end{cases}$$

For both models the limits on the cross section are meant to apply to the quantity $\langle\sigma v\rangle_c$, the $\langle\sigma v\rangle$ at the average collision velocity v_c.

The four profiles described above are shown in Figure 4.1.

4.3.3 Smoothing kernel

The angular size of the source is comparable to the angular resolution of Fermi-LAT above 10 GeV. Since the analysis is performed with a binned likelihood method (see Section 4.5), to avoid a dependence of the model on the position in the analysis grid, the profiles are smoothed in such a way

$$\hat{F} = \frac{1}{\Delta\Omega}\int_{\Delta\Omega} F\,d\Omega, \tag{4.9}$$

where $\Delta\Omega \sim 0.037^\circ \times 0.037^\circ$, corresponding to an area 15 pc $\times$ 15 pc, which is slightly smaller than the pixel size (0.05°). The smoothing kernel is about a factor 2.5 narrower than the angular resolution of Fermi-LAT above 10 GeV and its particular choice has no impact on the results of the likelihood fit.

4.4 The γ-ray spectrum from WIMP annihilation

As described in the introduction to this chapter, in the simplest WIMP models the DM particles can annihilate into a pair of particles of the Standard Model (quarks, leptons, gauge bosons). The channels with light final states (quarks: u, d, s; leptons: e, μ, ν; bosons: g) are suppressed by the helicity[4] [101], and the main products of the annihilation are heavy particles (quarks: b, t, c; leptons: τ; bosons: W, Z, H). The different annihilation final states i are characterised by the branching ratio k_i. Thus, for instance, $k_{\tau\tau}$ denotes the average fraction of annihilations resulting in a $\tau\bar{\tau}$ pair. These heavy particles are unstable and eventually decay into stable products including γ-rays (mainly from π^0-decays).

The overall γ-ray spectrum resulting from the WIMP annihilation is a linear combination of spectra of different channels with coefficients k_i,

$$\frac{dN_\gamma}{dE} = \sum_i k_i \frac{dN_\gamma^i}{dE}. \tag{4.10}$$

The contribution of each channel k_i depends on the choice of the SUSY model. To avoid a complete scan of the SUSY parameter space, spectra of single channels are used such that the upper limits are obtained on the products $k_i\sigma$. For each neutralino mass two types of spectral models are used. They correspond to pure annihilation into $b\bar{b}$ and $\tau\bar{\tau}$, respectively. Figure 4.2 shows the differential γ-ray spectra from the annihilation of two neutralinos with mass $m_\chi = 200$ GeV, into different final states. The spectra shown in the figure are normalised as if each channel were the only channel of the annihilation. As can be seen, all spectra, except those corresponding to the $\tau\bar{\tau}$ and $t\bar{t}$ channels, resemble the spectrum of the $b\bar{b}$ channel. Therefore, placing a limit on $k_{bb}\sigma$ provides a very good approximation of the upper bound on $(k_{bb} + k_{cc} + k_{WW} + k_{ZZ})\,\sigma$.

Note that, for a significant part of SUSY parameter space, $(k_{bb} + k_{cc} + k_{WW} + k_{ZZ})$ is close to 1. The branching ratio of the $\tau\bar{\tau}$ channel is usually significantly smaller than 1, but the spectrum is very hard hence easily noticeable since the background rapidly decreases with the energy. The $t\bar{t}$ spectrum is somewhat softer than that of $b\bar{b}$ but not very different hence this channel is not considered in this work.

In the analysis the upper limits are evaluated using an array of neutralino masses. The expected mass range [102] covers an approximately uniform interval in $\log E$ whose values are: 40, 50, 63, 80, 100, 126, 159, 199, 251, 316, 398, 501, 631, 794, 1000, 1259, 1585, 1995, 2512, 3162, 3981, and 5011 GeV. The number of spectral models tested is then 44. Half of which are from the $b\bar{b}$ channel and the other half from the $\tau\bar{\tau}$.

[4]The projection of the particle spin onto the direction of momentum.

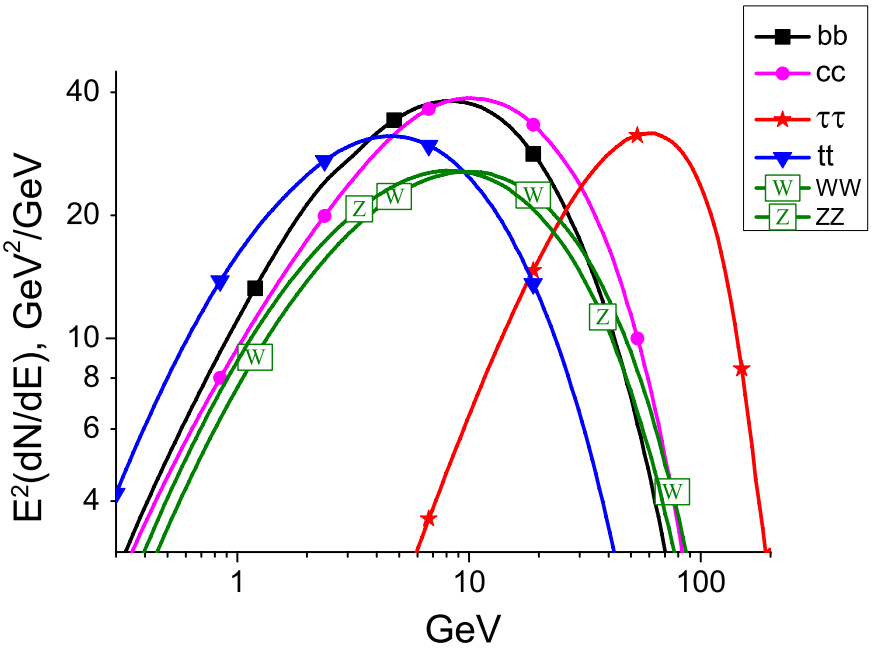

Figure 4.2: Differential γ-ray spectra generated by the annihilation of two neutralinos with a mass $m_\chi = 200$ GeV. Several different channels are shown. Each spectrum is normalised as if the corresponding channel were the only channel of the annihilation.

4.5 Observations of Segue 1 with Fermi-LAT

As already mentioned in Section 4.2, to search for evidence of γ-ray emission from Segue 1, the analysis is performed with data from Fermi-LAT. The data come from observations over a period of ~ 3.5 years, from August 8, 2008 to February 4, 2012.

The data analysis is performed with the Fermi-LAT `ScienceTools` version 9.23.1, using the post-launch P7SOURCE_V6 instrument response functions. The cosmic-ray background is reduced by choosing the P7SOURCE class which only includes events with high probability of being photons. A zenith-angle cut of 100° is also required in order to minimise the spill-over of photons from the Earth limb. Time intervals where any part of the region of interest (ROI) is beyond the zenith-angle limit are excluded. In addition, data are not taken while the observatory is transiting the South Atlantic Anomaly and excluded when the rocking angle exceeds 52°.

A binned likelihood analysis is performed on a map with 0.05° pixel size in gnomonic (TAN) projection, measuring 10° on a side and centred on $\alpha_{J2000} = 151.767°$ and $\delta_{J2000} = 16.0819°$, the nominal position of Segue 1. Only photons with reconstructed energy greater than 2.4 GeV, for which the 68%-containment radius of the point-spread function is narrower than $\sim 0.45°$, are used. The annihilation spectra are always substantially harder than those of the background, and therefore a high energy threshold can help to minimise background

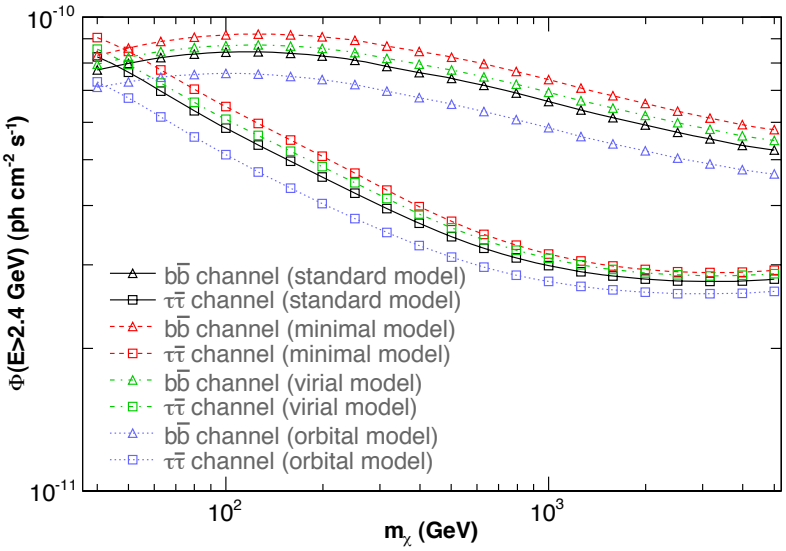

Figure 4.3: 95%-C.L. integral flux upper limits for Segue 1. The curves with the same color represent the two channels 100% $b\bar{b}$ (triangular markers) and 100% $\tau\bar{\tau}$ (square markers) for a specific model. All of the four models described in the text are showed.

contamination.

The resulting background model includes seven sources listed in the 2$^{\text{nd}}$ Fermi-LAT catalog, and the LAT standard Galactic diffuse emission component `gal_2yearp7v6_v0.fits` along with the corresponding isotropic template `iso_p7v6source.txt` that accounts for extragalactic emission and residual cosmic-ray contamination [5]. All the seven sources lie outside the ROI and are modelled as point sources with power-law energy spectra. Their spatial and spectral parameters are kept fixed at the values given in the catalog, while the normalisations of the diffuse components are permitted to freely vary.

Segue 1 is characterised by a spatial template of 2° diameter with a resolution of 0.05°, following Equations 4.3 and 4.5. Despite the spatial binning is slightly larger than the smoothing kernel applied to the Segue 1 profile, the results of the likelihood analysis are not affected. Analyses with different binning scale show, in fact, changes in the integral flux upper limits less than 1%.

As described above, two different model spectra for the self-annihilation of neutralinos into quarks ($b\bar{b}$) and leptons ($\tau\bar{\tau}$) for each of the four model profiles (standard, minimal, virial, and orbital) are used. 22 values of dark-matter particle mass from 40 GeV to 5011 GeV are tested.

[5] Both are available from the *Fermi* Science Support Centre.

m_χ, GeV	Flux U.L., $b\bar{b}$	Flux U.L., $\tau\bar{\tau}$
50	7.98	7.65
100	8.43	5.83
501	7.42	3.44
1000	6.64	2.99
5011	5.24	2.80

Table 4.1: Integral-flux upper limits above an energy threshold of 2.4 GeV for different WIMP masses (standard model). The confidence level is 95% and the units 10^{-11} ph cm^{-2} s^{-1}.

4.6 Analysis and results

The data analysis is performed over an energy range from 2.4 GeV to 300 GeV. The low-energy limit is *a priori* chosen to optimise the constraints on the neutralino masses above 100 GeV. The normalisation of the Segue 1 spatial template is the relevant free parameter of the analysis since the position is kept fixed. No significant γ-ray signal is detected from Segue 1. Thus, integral flux upper limits are derived over the whole energy range using the maximum likelihood technique. These limits are shown in Figure 4.3 as a function of the neutralino mass for both annihilation channels and for all models. Numerical values of the 95% confidence-level (CL) upper limits for the standard model are provided in Table 4.1.

It is apparent form Figure 4.2 that on average the $b\bar{b}$ final state predicts a lower photon energy than the $\tau\bar{\tau}$ channel. Therefore, the background contamination is more serious for the $b\bar{b}$ channels and, consequently, the flux upper limits are better (i.e., lower) for the $\tau\bar{\tau}$ final state.

The impact of using P7SOURCE class events, instead of the older P6_V3_DIFFUSE, is also investigated. Differences of the two data sets slightly affect the results of the upper limits on $\langle\sigma v\rangle_c$. The analysis performed with the Pass-6 data provides more constraining upper limits compared with the Pass-7 data, of around 10% for the low-mass neutralino (i.e., $m_\chi < 100$ GeV for $b\bar{b}$ and $m_\chi < 501$ GeV for $\tau\bar{\tau}$ model) and around 20% for those with higher mass. Note that this change is likely due to a statistical fluctuations. The templates for diffuse and isotropic emission are different for Pass 6 and Pass 7, and they dominate the likelihood fit. In the Pass-7 list of events between 2.4 GeV and 300 GeV reconstructed energy, 7 events are found within 0.5° of the nominal position of Segue 1 (5 events in the Pass-6 event list). The entire region of interest comprises 920 events, or 9.2 per square-degree on average.

Accounting for the source extent in the likelihood analysis increases the upper limits by typically 20%–25%, but only 10%–15% for $\tau\bar{\tau}$ models with large particle mass, for which most of the gamma rays have energies $\gtrsim 100$ GeV.

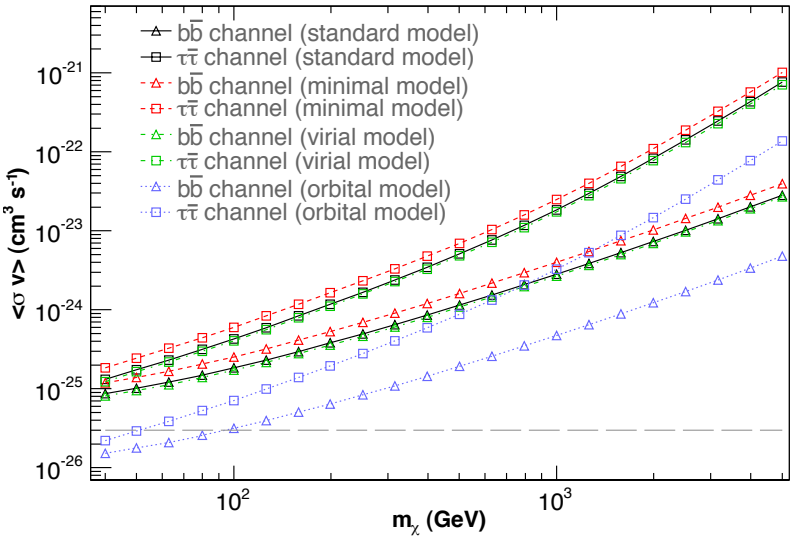

Figure 4.4: 95%-CL upper limits on $\langle\sigma v\rangle$ as a function of the neutralino mass for $k_{bb} = 1$ (curves with triangular markers) and $k_{\tau\tau} = 1$ (curves with square markers) for each of the four models. The horizontal dashed line shows the canonical value of the self-annihilation cross section for a thermal WIMP ($\langle\sigma v\rangle_a \simeq 3 \times 10^{-26}$ cm^3 s^{-1}).

4.7 Discussion and conclusions

Figure 4.4 shows the 95% CL upper limits on $\langle\sigma v\rangle_c$ as a function of the neutralino mass assuming $k_{bb} = 1$ or $k_{\tau\tau} = 1$. These limits are derived for each of the four models described in this work, and for both $b\bar{b}$ and $\tau\bar{\tau}$ channels.

What is interesting in these results is that the standard and minimal models do not differ significantly. This suggests that the limits obtained using the Einasto profile are quite conservative and not very sensitive to the shape of the density profile. Furthermore, the standard and virial models show an almost identical behaviour. This is due to the fact that the central region of the source has a radius smaller than r_s. As a consequence $\phi(r)$, the gravitational potential of Segue 1, and so the average particle velocity v, varies only slightly inside the source region.

From the results it is apparent that the only model that excludes the relic abundance cross-section $\langle\sigma v\rangle_a \simeq 3 \times 10^{-26}$ cm^3 s^{-1}, for small neutralino masses, is the orbital model. This reflects the fact that $v_{\rm orb} \to 0$ if the central density of the halo is finite. As a result, the signal at the centre is significantly boosted. However, the exclusion region only contains low-mass neutralinos ($m_\chi \lesssim 100$ GeV) whose annihilation cross section is enhanced by the Sommerfeld effect. As already discussed in Section 4.3.2, the Sommerfeld enhancement for low-mass particles can occur only if the WIMPs interact through low-mass force carriers,

that do not belong to the class of the standard gauge bosons. Thus, only a few exotic dark matter models can be excluded.

As mentioned in Section 4.4, channels ($b\bar{b} + c\bar{c} + W\bar{W} + Z\bar{Z}$) dominate for the majority of SUSY models and the total γ-ray spectrum differs little from that of the $b\bar{b}$ annihilation alone. Therefore, the limit given by the $b\bar{b}$ model can be considered with reasonable accuracy as the limit on the total cross section.

Overall, the results obtained in this work do not significantly constrain dark-matter models. In fact, those models for which the dark matter has never been in thermodynamic equilibrium should predict an annihilation cross section much lower than the limits shown in Figure 4.4. On the other hand, if the dark matter was once in thermodynamic equilibrium its cross section at that epoch can be estimated from the dark-matter abundance $\langle\sigma v\rangle_a$ for Majorana particles [103]. But, as already seen, the upper limits found in this work never reach $\langle\sigma v\rangle_a$, except for the orbital model. All other profiles are at least a factor 4 higher.

One of the more significant findings to emerge from this study is that the limits on $\langle\sigma v\rangle_c$ must be improved between two and five orders of magnitude for particles with mass > 1 TeV. This prediction is most likely out of reach for space based instruments operating in the GeV γ-ray band like Fermi-LAT, but may be within reach of future ground based observatories like CTA [104]. The main advantage of these instruments is in fact their large γ-ray collecting area ($\sim 10^6$ m^2) that could improve their flux sensitivity enough to reach $\langle\sigma v\rangle_a$ even for very heavy WIMPs. The only significant weakness of the imaging atmospheric Cherenkov telescopes is their relatively high energy threshold (~ 50 GeV) that limits their capability for probing WIMPs with lighter masses. On the other hand, for a large part of reasonable dark-matter models (e.g., mSUGRA, CMSSM) a low-mass WIMP will very soon be excluded (or detected) by the Large Hadron Collider (LHC).

5

Conclusions

This analysis has investigated the detailed properties of GeV γ-ray emission of a supernova remnant using data from the LAT instrument onboard the Fermi Gamma-Ray Space Telescope. For these kind of analyses the diffuse emission represents the dominant component of the background. The ability to accurately model it is a crucial aspect to obtain reliable spectra and morphology of extended sources such as supernova remnants.

In this work a novel approach, which is based on a deconvolution technique of high-resolution radio data, is used to model the diffuse Galactic γ-ray emission and to account for the small-scale structures therein. Its innovative aspect allows to correct the HI data for HI self-absorption, that prevents the detection of the colder atomic hydrogen gas, and therefore to include the contribution of the resulting absorber component into the total gas density. One of the more significant findings to emerge from this study is that this contribution can reach more than 30% of the total hydrogen gas density for several lines of sight. Neglecting the HI self-absorption may thus lead to underestimate the interstellar gas density, especially in the Galactic plane where most of the cold gas lies.

The high-resolution HI map, corrected for self-absorption, together with the map of molecular gas derived from CO-line measurements, are deconvolved to provide the spatial distribution of matter in the Galaxy. The resulting distribution is then used to calculate the γ-ray emissivities from which the intensity of the γ-ray background template is derived. The inverse-Compton templates, that account for the emission due to interactions of cosmic rays with the radiation fields, are used directly because they lack small-scale structure.

The corrected-background map is then used for the analysis of the extended supernova remnant RX J1713.7–3946. The first important result of this analysis comes from the likelihood ratio test between the model with the standard Fermi-LAT diffuse background and the one calculated in this work. The test statistic favours in fact the model with the corrected-

background with a significance of 4σ supporting the idea that the emission due to the interaction of cosmic rays with the cold absorbing hydrogen clouds gives a non-negligible contribution to the overall diffuse emission.

The properties of the extended emission associated with the supernova remnant are investigated with spatial and spectral likelihood analyses. The analysis of the spatial morphology shows the similarity with the emission observed at higher energies, particularly in the northwest region of the remnant where an enhancement of the emission appears. A feature probably due to the interaction of cosmic rays accelerated at the shock front of the supernova remnant with a local molecular cloud. This hypothesis needs however detailed investigations to be firmly established.

The spectral analysis over the whole energy range of the Fermi-LAT data gives a spectral index of 1.5 for RX J1713.7–3946, a hard index value which is in good agreement with a previous study carried out by the Fermi-LAT collaboration. Since the measured spectrum of the supernova remnant cannot be easily interpreted using only data from GeV-to-TeV observations, to draw conclusions about the nature of the emission of RX J1713.7–3946 a phenomenological spectral modelling in multi-wavelength is performed. The evidence from this study suggests that the GeV γ-ray spectrum does not agree with the expected flux predicted by a hadronic model. This implies that the hard Fermi-LAT spectrum cannot be ascribed to the π^0-decay emission, leading thus to the conclusion that the leptonic scenario is instead the most natural picture for the high-energy γ-ray emission of RX J1713.7–3946. The leptonic scenario however does not rule out the possibility that cosmic-ray nuclei are accelerated in this supernova remnant, but it suggests that the ambient density may not be high enough to produce a significant hadronic γ-ray emission.

Further investigations involving other supernova remnants using the improved background developed in this work could allow compelling population studies, and hence prove or disprove the origin of Galactic cosmic-ray nuclei in these astrophysical objects. A breakthrough regarding the identification of the radiation mechanisms could be moreover achieved with a new generation of instruments such as CTA.

Bibliography

[1] O. Adriani et al. PAMELA Measurements of Cosmic-ray Proton and Helium Spectra. *Science*, 332:69–72, 2011.

[2] O. Adriani et al. The cosmic-ray electron flux measured by the PAMELA experiment between 1 and 625 GeV. *Phys.Rev.Lett.*, 106:201101, 2011.

[3] A.W. Strong and I.V. Moskalenko. A Galactic Cosmic-Ray Database. 2009.

[4] Johannes Blumer, Ralph Engel, and Jorg R. Horandel. Cosmic Rays from the Knee to the Highest Energies. *Prog.Part.Nucl.Phys.*, 63:293–338, 2009.

[5] K. A. Lave et al. Elemental GCR Observations During the 2009–2010 Solar Minimum Period. In *33rd International Cosmic Ray Conference*, 2013.

[6] K. Lodders, H. Palme, and H.-P. Gail. Abundances of the elements in the solar system. 2009.

[7] Peter M.W. Kalberla, W.B. Burton, Dap Hartmann, E.M. Arnal, E. Bajaja, et al. The Leiden/Argentine/Bonn (LAB) survey of Galactic HI: Final data release of the combined LDS and IAR surveys with improved stray-radiation corrections. *Astron.Astrophys.*, 440:775–782, 2005.

[8] T.M. Dame, Dap Hartmann, and P. Thaddeus. The Milky Way in molecular clouds: A new complete CO survey. *Astrophys.J.*, 547:792–813, 2001.

[9] Troy A. Porter, Igor V. Moskalenko, Andrew W. Strong, Elena Orlando, and Laurent Bouchet. Inverse Compton Origin of the Hard X-Ray and Soft Gamma-Ray Emission from the Galactic Ridge. *Astrophys.J.*, 682:400–407, 2008.

[10] Andrew W. Strong, Igor V. Moskalenko, and Olaf Reimer. Diffuse continuum gamma-rays from the galaxy. *Astrophys.J.*, 537:763–784, 2000.

[11] Donald C. Ellison, Daniel J. Patnaude, Patrick Slane, Pasquale Blasi, and Stefano Gabici. Particle Acceleration in Supernova Remnants and the Production of Thermal and Nonthermal Radiation. *Astrophys.J.*, 661:879–891, 2007.

[12] P. Morrison. On gamma-ray astronomy. *Il Nuovo Cimento*, 7:858–865, 1958.

[13] A.M. Hillas. In *19th International Cosmic Ray Conference, La Jolla, USA*, volume 3, page 445, 1985.

[14] T.C. Weekes, M.F. Cawley, D.J. Fegan, K.G. Gibbs, A.M. Hillas, et al. Observation of TeV gamma rays from the Crab nebula using the atmospheric Cerenkov imaging technique. *Astrophys.J.*, 342:379–395, 1989.

[15] S.M. Derdeyn, C.H. Ehrmann, C.E. Fichtel, D.A. Kniffen, and R.W. Ross. Sas-b digitized spark chamber gamma ray telescope. *Nucl.Instrum.Meth.*, 98:557–566, 1972.

[16] G.F. Bignami, G. Boella, J.J. Burger, B.G. Taylor, P. Keirle, J.A. Paul, H.A. Mayer-Hasselwander, E. Pfeffermann, L. Scarsi, and B.N. Swanenburg. The Cos-B Experiment for Gamma-Ray Astronomy. *Space Sci.Instrum.*, 1:245–268, 1975.

[17] C. Pittori and M. Tavani. Scientific goals and instrument performance of the gamma-ray imaging detector AGILE. *Nucl.Phys.Proc.Suppl.*, 134:72–74, 2004.

[18] J.A. Hinton. The Status of the H.E.S.S. project. *New Astron.Rev.*, 48:331–337, 2004.

[19] D. Ferenc. The MAGIC gamma-ray observatory. *Nucl.Instrum.Meth.*, A553:274–281, 2005.

[20] T.C. Weekes, H. Badran, S.D. Biller, I. Bond, S. Bradbury, et al. VERITAS: The Very energetic radiation imaging telescope array system. *Astropart.Phys.*, 17:221–243, 2002.

[21] W.D. Apel, J.C. Arteaga, A.F. Badea, K. Bekk, M. Bertaina, et al. The KASCADE-Grande experiment. *Nucl.Instrum.Meth.*, A620:202–216, 2010.

[22] W.D. Apel et al. Kneelike structure in the spectrum of the heavy component of cosmic rays observed with KASCADE-Grande. *Phys.Rev.Lett.*, 107:171104, 2011.

[23] D.J. Bird et al. The Cosmic ray energy spectrum observed by the Fly's Eye. *Astrophys.J.*, 424:491–502, 1994.

[24] Kenneth Greisen. End to the cosmic ray spectrum? *Phys.Rev.Lett.*, 16:748–750, 1966.

[25] G.T. Zatsepin and V.A. Kuzmin. Upper limit of the spectrum of cosmic rays. *JETP Lett.*, 4:78–80, 1966.

[26] James J. Beatty and Stefan Westerhoff. The Highest-Energy Cosmic Rays. *Ann.Rev.Nucl.Part.Sci.*, 59:319–345, 2009.

[27] Reinhard Schlickeiser. *Cosmic Ray Astrophysics*. Springer, 2002.

[28] Steven J. Gibson, A. Russell Taylor, Lloyd A. Higgs, and Peter E. Dewdney. A New View of Cold H I Clouds in the Milky Way. *Astrophys.J.*, 540(2):851, 2000.

[29] Rahul Shetty, Simon C. Glover, Cornelis P. Dullemond, and Ralf S. Klessen. Modeling CO Emission: I. CO as a Column Density Tracer and the X-Factor in Molecular Clouds. 2010.

[30] A.W. Strong, I.V. Moskalenko, O. Reimer, S. Digel, and R. Diehl. The distribution of cosmic-ray sources in the Galaxy, gamma-rays, and the gradient in the CO-to-H2 relation. *Astron.Astrophys.*, 422:L47–L50, 2004.

[31] David B. Henley, Robin L. Shelton, Kyujin Kwak, M. Ryan Joung, and Mordecai-Mark Mac Low. The Origin of the Hot Gas in the Galactic Halo: Confronting Models with XMM-Newton Observations. *Astrophys.J.*, 723:935–953, 2010.

[32] J.S. Mathis, P.G. Mezger, and N. Panagia. Interstellar radiation field and dust temperatures in the diffuse interstellar matter and in giant molecular clouds. *Astron.Astrophys.*, 128:212–229, 1983.

[33] B.T. Draine and Aigen Li. Infrared emission from interstellar dust. I. stochastic heating of small grains. *Astrophys.J.*, 551:807–824, 2001.

[34] K. Mattila, D. Lemke, L. K. Haikala, R. J. Laureijs, A. Leger, K. Lehtinen, C. Leinert, and P. G. Mezger. Spectrophotometry of UIR bands in the diffuse emission of the galactic disk. *Astron.Astrophys.*, 315:L353–L356, November 1996.

[35] K. Koyama, R. Petre, E.V. Gotthelf, U. Hwang, M. Matsuura, et al. Evidence for shock acceleration of high-energy electrons in the supernova remnant SN1006. *Nature*, 378:255–258, 1995.

[36] S. van den Bergh and R. D. McClure. Rediscussion of extragalactic supernova rates derived from Evans's 1980-1988 observations. *Astrophys.J.*, 425:205–209, April 1994.

[37] S.E. Woosley and T.A. Weaver. The Evolution and explosion of massive stars. 2. Explosive hydrodynamics and nucleosynthesis. *Astrophys.J.Suppl.*, 101:181–235, 1995.

[38] G. Taylor. The Formation of a Blast Wave by a Very Intense Explosion. I. Theoretical Discussion. *Royal Society of London Proceedings Series A*, 201:159–174, March 1950.

[39] L. I. Sedov. *Similarity and Dimensional Methods in Mechanics*. New York, 1959.

[40] M.A. Malkov and L O'C Drury. Nonlinear theory of diffusive acceleration of particles by shock waves. *Rep.Prog.Phys.*, 64(4):429, 2001.

[41] P.O. Lagage and C.J. Cesarsky. The maximum energy of cosmic rays accelerated by supernova shocks. *Astron.Astrophys.*, 125:249–257, 1983.

[42] A. R. Bell. Turbulent amplification of magnetic field and diffusive shock acceleration of cosmic rays. *MNRAS*, 353:550–558, September 2004.

[43] Aya Bamba, Ryo Yamazaki, Masaru Ueno, and Katsuji Koyama. Fine structures of shock of SN 1006 with the Chandra observation. *Astrophys.J.*, 589:827, 2003.

[44] V.V. Dwarkadas, I. Telezhinsky, and M. Pohl. On the Evolution of the Maximum Energy of Accelerated Particles in Young Supernova Remnants. 2012.

[45] F. Lebrun, K. Bennett, G. F. Bignami, P. A. Caraveo, J. B. G. M. Bloemen, R. Hermsen, W.and Buccheri, M. Gottwald, G. Kanbach, and H. A. Mayer-Hasselwander. Gamma-rays from atomic and molecular gas in the first galactic quadrant. *Astrophys.J.*, 274:231–236, 11 1983.

[46] S. D. Hunter, D. L. Bertsch, J. R. Catelli, T. M. Dame, S. W. Digel, B. L. Dingus, J. A. Esposito, C. E. Fichtel, R. C. Hartman, G. Kanbach, D. A. Kniffen, Y. C. Lin, H. A. Mayer-Hasselwander, P. F. Michelson, C. von Montigny, R. Mukherjee, P. L. Nolan, E. Schneid, P. Sreekumar, P. Thaddeus, and D. J. Thompson. EGRET Observations of the Diffuse Gamma-Ray Emission from the Galactic Plane. *Astrophys.J.*, 481:205, may 1997.

[47] A.A. Abdo et al. Fermi LAT Observation of Diffuse Gamma-Rays Produced Through Interactions between Local Interstellar Matter and High Energy Cosmic Rays. *Astrophys.J.*, 703:1249–1256, 2009.

[48] Fermi observations of Cassiopeia and Cepheus: diffuse gamma-ray emission in the outer Galaxy. *Astrophys.J.*, 710:133–149, 2010.

[49] M. Ackermann et al. Constraints on the Cosmic-ray Density Gradient Beyond the Solar Circle from Fermi Îş-ray Observations of the Third Galactic Quadrant. *Astrophys.J.*, 726:81, 2011.

[50] A.W. Strong, I.V. Moskalenko, S. Digel, T.A. Porter, G. Johannesson, E. Orlando, and A. Vladimirov. GALPROP. http://galprop.stanford.edu/.

[51] A.W. Strong and I.V. Moskalenko. Propagation of cosmic-ray nucleons in the galaxy. *Astrophys.J.*, 509:212–228, 1998.

[52] A.W. Strong, T.A. Porter, S.W. Digel, G. Johannesson, P. Martin, et al. Global cosmic-ray related luminosity and energy budget of the Milky Way. *Astrophys.J.*, 722:L58–L63, 2010.

[53] Andrew W. Strong, Igor V. Moskalenko, and Vladimir S. Ptuskin. Cosmic-ray propagation and interactions in the Galaxy. *Ann.Rev.Nucl.Part.Sci.*, 57:285–327, 2007.

[54] I.V. Moskalenko, S.G. Mashnik, and A.W. Strong. New calculation of radioactive secondaries in cosmic rays. 2001.

[55] E. C. Stone, A. M. Frandsen, R. A. Mewaldt, E. R. Christian, D. Margolies, J. F. Ormes, and F. Snow. The Advanced Composition Explorer. *Space Science Reviews*, 86:1–22, July 1998.

[56] Steven J. Gibson, A. Russell Taylor, Lloyd A. Higgs, Christopher M. Brunt, and Peter E. Dewdney. An Automated method for the detection and extraction of HI self-absorption in high-resolution 21cm line surveys. *Astrophys.J.*, 626:214–232, 2005.

[57] A. R. Taylor, S. J. Gibson, M. Peracaula, P. G. Martin, T. L. Landecker, C. M. Brunt, P. E. Dewdney, S. M. Dougherty, A. D. Gray, L. A. Higgs, C. R. Kerton, L. B. G. Knee, R. Kothes, C. R. Purton, B. Uyaniker, B. J. Wallace, A. G. Willis, and D. Durand. The canadian galactic plane survey. *The Astronomical Journal*, 125(6):3145, 2003.

[58] Naomi M. McClure-Griffiths, J.M. Dickey, B.M. Gaensler, A.J. Green, M. Haverkorn, et al. The Southern Galactic Plane Survey: HI observations and analysis. *Astrophys.J.Suppl.*, 158:178–187, 2005.

[59] Jeroen M. Stil, A.R. Taylor, J.M. Dickey, D.W. Kavars, P.G. Martin, et al. The VLA Galactic Plane Survey. *Astron.J.*, 132:1158–1176, 2006.

[60] T. J. Sodroski, N. Odegard, R. G. Arendt, E. Dwek, J. L. Weiland, M. G. Hauser, and T. Kelsall. A Three-dimensional Decomposition of the Infrared Emission from Dust in the Milky Way. *The Astrophysical Journal*, 480(1):173, 1997.

[61] Martin Pohl, Peter Englmaier, and Nicolai Bissantz. 3D Distribution of Molecular Gas in the Barred Milky Way. *Astrophys.J.*, 677:283–291, 2008.

[62] D.P.Clemens. Massachusetts-stony brook galactic plane co survey: The galactic disk rotation curve. *Astrophys.J.*, 295(2):422–436, August 1985.

[63] Igor V. Moskalenko and Andrew W. Strong. Anisotropic inverse Compton scattering in the galaxy. *Astrophys.J.*, 528:357–367, 2000.

[64] C. D. Dermer. Secondary production of neutral pi-mesons and the diffuse galactic gamma radiation. *Astron.Astrophys.*, 157:223–229, March 1986.

[65] H.W. Koch and J.W. Motz. Bremsstrahlung cross-section formulas and related data. *Reviews of Modern Physics*, 31(4):920–955, 1959.

[66] E. Pfeffermann and B. Aschenbach. ROSAT observation of a new supernova remnant in the constellation Scorpius. In *International Conference on X-ray Astronomy and Astrophysics: Röntgenstrahlung from the Universe*, pages 267–268, 1996.

[67] K. Koyama, K. Kinugasa, K. Matsuzaki, M. Nishiuchi, M. Sugizaki, K. Torii, S. Yamauchi, and B. Aschenbach. Discovery of Non-Thermal X-Rays from the Northwest Shell of the New SNR RX J1713.7-3946: The Second SN 1006? *Publications of the Astronomical Society of Japan*, 49:L7–L11, Jun 1997.

[68] Patrick Slane, Bryan M. Gaensler, T.M. Dame, John P. Hughes, Paul P. Plucinsky, et al. Nonthermal X-Ray Emission from the Shell-Type Supernova Remnant G347.3-0.5. *Astrophys.J.*, 525:357–367, 1999.

[69] Yasunobu Uchiyama, F.A. Aharonian, and T. Takahashi. Fine - structure of non-thermal x-rays in the Chandra image of SNR RX J1713.7-3946. *Astron.Astrophys.*, 400:567–574, 2003.

[70] G. Cassam-Chenaï, A. Decourchelle, J. Ballet, J.-L. Sauvageot, G. Dubner, and E. Giacani. XMM-Newton observations of the supernova remnant RX J1713.7-3946 and its central source. *Astron.Astrophys.*, 427:199–216, 2004.

[71] H. Muraishi, T. Tanimori, S. Yanagita, T. Yoshida, M. Moriya, et al. Evidence for TeV gamma-ray emission from the shell type SNR RXJ1713.7-3946. *Astron.Astrophys.*, 354:L57–L61, 2000.

[72] R.C. Hartman et al. The Third EGRET catalog of high-energy gamma-ray sources. *Astrophys.J.Suppl.*, 123:79, 1999.

[73] Yousaf M. Butt, Diego F. Torres, Jorge A. Combi, Thomas Dame, and Gustavo E. Romero. Is the supernova remnant rx j1713.7-3946 a hadronic cosmic ray accelerator ? *Astrophys.J.*, 562:L167–L172, 2001.

[74] R. Enomoto and R. Enomoto. The acceleration of cosmic-ray protons in the supernova remnant rx j1713.7-3946. *Nature*, 416:823–826, 2002.

[75] O. Reimer and M. Pohl. No evidence yet for hadronic TeV gamma-ray emission from SNR RX J1713.7-3946. *Astron.Astrophys.*, 390:L43–L46, July 2002.

[76] F.A. Aharonian et al. High-energy particle acceleration in the shell of a supernova remnant. *Nature*, 432:75–77, 2004.

[77] W.B. Atwood et al. The Large Area Telescope on the Fermi Gamma-ray Space Telescope Mission. *Astrophys.J.*, 697:1071–1102, 2009.

[78] A.A. Abdo. Observations of the young supernova remnant RX J1713.7-3946 with the Fermi Large Area Telescope. *Astrophys.J.*, 734:28, 2011.

[79] Fermi Large Area Telescope Second Source Catalog. *Astrophys.J.Suppl.*, 199:31, 2012.

[80] J.R. Mattox, D.L. Bertsch, J. Chiang, B.L. Dingus, S.W. Digel, et al. The Likelihood Analysis of EGRET Data. *Astrophys.J.*, 461:396, 1996.

[81] David A. Green. Galactic supernova remnants: An Updated catalogue and some statistics. *Bull.Astron.Soc.India*, 32:335–370, 2004.

[82] M. Ackermann et al. The Fermi Large Area Telescope On Orbit: Event Classification, Instrument Response Functions, and Calibration. *Astrophys.J.Suppl.*, 203:4, 2012.

[83] Takaaki Tanaka, Yasunobu Uchiyama, Felix A. Aharonian, Tadayuki Takahashi, Aya Bamba, et al. Study of Nonthermal Emission from SNR RX J1713.7-3946 with Suzaku. *Astrophys.J.*, 685:988, 2008.

[84] T. Shibata, T. Ishikawa, and S. Sekiguchi. A possible approach to three-dimensional cosmic-ray propagation in the Galaxy IV. Electrons and electron-induced gamma-rays. *Astrophys.J.*, 727:38, 2011.

[85] Troy A. Porter, Igor V. Moskalenko, and Andrew W. Strong. Inverse Compton Emission from Galactic Supernova Remnants: Effect of the Interstellar Radiation Field. *Astrophys.J.*, 648:L29–L32, 2006.

[86] Steven J. Sturner, Jeffrey G. Skibo, Charles D. Dermer, and John R. Mattox. Temporal evolution of nonthermal spectra from supernova remnants. *Astrophys.J.*, 490(2):619, 1997.

[87] Ching-Yuan Huang, S.-E. Park, M. Pohl, and C.D. Daniels. Gamma-Rays Produced in Cosmic-Ray Interactions and the TeV-band Spectrum of RX J1713-3946. *Astropart.Phys.*, 27:429–439, 2007.

[88] Donald C. Ellison, Daniel J. Patnaude, Patrick Slane, and John Raymond. Efficient cosmic ray acceleration, hydrodynamics, and Self-consistent Thermal X-ray Emission applied to SNR RX J1713.7-3946. *Astrophys.J.*, 712:287–293, 2010.

[89] A.N. Baushev, S. Federici, and M. Pohl. Spectral analysis of the gamma-ray background near the dwarf Milky Way satellite Segue 1: Improved limits on the cross section of neutralino dark matter annihilation. *Phys.Rev.*, D86:063521, 2012.

[90] C.B. Netterfield et al. A measurement by Boomerang of multiple peaks in the angular power spectrum of the cosmic microwave background. *Astrophys.J.*, 571:604–614, 2002.

[91] C. Pryke, N.W. Halverson, E.M. Leitch, J. Kovac, J.E. Carlstrom, et al. Cosmological parameter extraction from the first season of observations with DASI. *Astrophys.J.*, 568:46–51, 2002.

[92] Stephen P. Martin. A Supersymmetry primer. 1997.

[93] E. Komatsu et al. Seven-Year Wilkinson Microwave Anisotropy Probe (WMAP) Observations: Cosmological Interpretation. *Astrophys.J.Suppl.*, 192:18, 2011.

[94] Joshua D. Simon, Marla Geha, Quinn E. Minor, Gregory D. Martinez, Evan N. Kirby, et al. A Complete Spectroscopic Survey of the Milky Way Satellite Segue 1: The Darkest Galaxy. *Astrophys.J.*, 733:46, 2011.

[95] P. Gondolo, J. Edsjo, P. Ullio, L. Bergstrom, Mia Schelke, et al. DarkSUSY: Computing supersymmetric dark matter properties numerically. *JCAP*, 0407:008, 2004.

[96] J. Aleksic et al. Searches for Dark Matter annihilation signatures in the Segue 1 satellite galaxy with the MAGIC-I telescope. *JCAP*, 1106:035, 2011.

[97] Massimiliano Lattanzi and Joseph I. Silk. Can the WIMP annihilation boost factor be boosted by the Sommerfeld enhancement? *Phys.Rev.*, D79:083523, 2009.

[98] A. N. Baushev. Interaction of clumpy dark matter with interstellar medium in astrophysical systems. *MNRAS*, 420:590–595, February 2012.

[99] Anton N. Baushev. Principal properties of the velocity distribution of dark matter particles on the outskirts of the Solar System. *J.Phys.Conf.Ser.*, 375:012048, 2012.

[100] A. N. Baushev. The universal density profile of the central region of dark matter haloes. *ArXiv e-prints*, May 2012.

[101] H. Goldberg. Constraint on the Photino Mass from Cosmology. *Phys.Rev.Lett.*, 50:1419, 1983.

[102] D. S. Gorbunov and V. A. Rubakov. *Introduction to the theory of the early universe.* 2011.

[103] Gianfranco Bertone, Dan Hooper, and Joseph Silk. Particle dark matter: Evidence, candidates and constraints. *Phys.Rept.*, 405:279–390, 2005.

[104] B.S. Acharya, M. Actis, T. Aghajani, G. Agnetta, J. Aguilar, et al. Introducing the CTA concept. *Astropart.Phys.*, 43:3–18, 2013.